

ACTA GEO TECHNICA SLOVENICA

2009/2

A. petkovšek et al.

A LABORATORY CHARACTERIZATION OF SOILS AND CLAY-BEARING ROCKS USING THE ENSLIN-NEFF WATER-ADSORPTION TEST

Z. tomanovič

INFLUENCE OF K_0 ON THE CREEP PROPERTIES OF MARL

A. gosar

A MICROTREMOR HVSR STUDY OF THE SEISMIC SITE EFFECTS IN THE AREA OF THE TOWN BREŽICE [SE SLOVENIA]

I. tasič & F. runovc

AUTOMATIC S-PHASE ARRIVAL IDENTIFICATION FOR LOCAL EARTHQUAKES

g. vilhar & v. jovičič

MEASUREMENT AND INTERPRETATION OF THE SMALL STRAIN STIFFNESS OF BOŠTANJ SILTY SAND

L. chien et al.

THE GEO-MECHANICS BEHAVIOR OF SOFT MARINE SILTS UNDER A NEARSHORE RUBBLE-MOUND BREAKWATER



**ACTA
GEOTECHNICA
SLOVENICA**

ISSN: 1854-0171

ustanovitelji

founders

Univerza v Mariboru, Fakulteta za gradbeništvo
University of Maribor, Faculty of Civil Engineering



Univerza v Ljubljani, Fakulteta za gradbeništvo in geodezijo
University of Ljubljana, Faculty of Civil
and Geodetic Engineering



Univerza v Ljubljani, Naravoslovnotehniška fakulteta
University of Ljubljana, Faculty of Natural
Sciences and Engineering



Slovensko geotehniško društvo
Slovenian Geotechnical Society



Društvo za podzemne in geotehniške konstrukcije
Society for Underground and Geotechnical
Constructions



izdajatelj

publisher

Univerza v Mariboru, Fakulteta za gradbeništvo
University of Maribor, Faculty of Civil Engineering

odgovorni urednik

editor-in-chief

Ludvik Trauner
Univerza v Mariboru

uredniki

co-editors

Bojana Dolinar
Univerza v Mariboru
Borut Macuh
Univerza v Mariboru
Stanislav Škrabl
Univerza v Mariboru
Helena Vrecl Kojc
Univerza v Mariboru
Bojan Žlender
Univerza v Mariboru

lektor

proof-reader

Paul McGuiness

naklada

circulation

500 izvodov - issues

tisk

print

Tercia tisk d.o.o. Ptuj

Revija redno izhaja dvakrat letno. Članki v reviji so recenzirani s strani priznanih mednarodnih strokovnjakov. Baze podatkov v katerih je revija indeksirana: SCIE - Science Citation Index Expanded, JCR - Journal Citation Reports / Science Edition, ICONDA - The international Construction database, GeoRef
Pri financiranju revije sodeluje Javna agencija za knjigo Republike Slovenije.

uredniški odbor

editorial board

Darinka Battelino
Università degli Studi di Trieste
József Farkas
Budapesti Műszaki és Gazdaságtudományi Egyetem
Theodoros Hatzigogos
Aristotle University of Thessaloniki
Rolf Katzenbach
Technische Universität Darmstadt
Zlatko Langof
Univerzitet u Sarajevu
Jakob Likar
Univerza v Ljubljani
Janko Logar
Univerza v Ljubljani
Bojan Majes
Univerza v Ljubljani
Milan Maksimović
Univerzitet u Beogradu
Borut Petkovšek
Zavod za gradbeništvo Slovenije
Mihael Ribičič
Univerza v Ljubljani
César Sagaseta
Universidad de Cantabria
Stephan Semprich
Technische Universität Graz
Abdul-Hamid Soubra
Université de Nantes
Ivan Vaniček
České vysoké učení technické v Praze
Franjo Verič
Sveučilište u Zagrebu

naslov uredništva

address

ACTA GEOTECHNICA SLOVENICA
Univerza v Mariboru, Fakulteta za gradbeništvo
Smetanova ulica 17
2000 Maribor
Slovenija
Telefon / Telephone: +386 (0)2 22 94 300
Faks / Fax: +386 (0)2 25 24 179
E-pošta / E-mail: ags@uni-mb.si

spletni naslov

web address

<http://www.fg.uni-mb.si/journal-ags>

The journal is published twice a year. Papers are peer reviewed by renowned international experts. Indexation data bases of the journal: SCIE - Science Citation Index Expanded, JCR - Journal Citation Reports / Science Edition, ICONDA - The international Construction database, GeoRef
Financially supported also by Slovenian Book Agency.

VSEBINA

2	Ludvik Trauner UVODNIK
4	ana petkovšek in drugi LABORATORIJSKA KARAKTERIZACIJA ZEMLJIN IN KAMNIN, KI VSEBUJEJO GLINO, S PREI- SKAVO ADSORPCIJE VODE PO ENSLIN - NEFFU
14	zvonko tomanovič VPLIV K_0 KARAKTERISTIKE LEZENJA LAPORJA SLOJU ZARADI DVOJNE DIFUZIJE
30	andrej gosar RAZISKAVE SEIZMIČNEGA VPLIVA LOKALNIH TAL NA OBMOČJU Z METODO MIKROTRERORJEV
46	izidor tasič in franc runovc SAMODEJNA RAZPOZNAVA PRIHODA VALOV "S" PRI LOKALNIH POTRESIH
56	gregor vilhar in vojkan jovičič MERJENJE IN INTERPRETACIJA TOGOSTI MELJASTEGA PESKA IZ BOŠTANJA PRI ZELO MAJHNIH DEFORMACIJAH
76	Lien-kwei chien in drugi GEOMEHANSKO OBNAŠANJE STISLJIVIH MORSKIH MELJEV POD OBRÉŽNIM VALOLOMOM IZ GRUŠČNATEGA NASIPA
94	NAVODILA AVTORJEM

CONTENTS

Ludvik Trauner EDITORIAL	3
ana petkovšek et al. A LABORATORY CHARACTERIZATION OF SOILS AND CLAY-BEARING ROCKS USING THE ENSLIN- NEFF WATER-ADSORPTION TEST	5
zvonko tomanovič INFLUENCE OF K_0 ON THE CREEP PROPERTIES OF MARL	15
andrej gosar A MICROTREMOR HVSR STUDY OF THE SEISMIC SITE EFFECTS IN THE AREA OF THE TOWN OF BREŽICE (SE SLOVENIA)	31
izidor tasič and franc runovc AUTOMATIC S-PHASE ARRIVAL IDENTIFICATION FOR LOCAL EARTHQUAKES	47
gregor vilhar and vojkan jovičič MEASUREMENT AND INTERPRETATION OF THE SMALL STRAIN STIFFNESS OF BOŠTANJ SILTY SAND	57
Lien-kwei chien et al. THE GEO-MECHANICS BEHAVIOR OF SOFT MARINE SILTS UNDER A NEARSHORE RUBBLE-MOUND BREAKWATER	77
INSTRUCTIONS FOR AUTHORS	95

UVODNIK

Cilj uredniškega odbora revije Acta Geotechnica Slovenica je objavljati visoko kvalitetne znanstvene in strokovne članke, kajti le ti vodijo k njeni uveljavitvi in mednarodnemu priznanju. Pri tem se zavedamo, da lahko tem ciljem sledimo le s pomočjo tistih, ki nam zaupajo. Zato bi se rad ob tej priliki zahvalil vsem avtorjem prispevkov, ki so za objavo svojih ugotovitev in spoznanj izbrali prav to revijo.

V pričujoči številki je objavljenih kar šest prispevkov. Za povečan obseg te številke revije smo se odločili zaradi izjemno zanimivih tem, ki jih članki obravnavajo.

Ana Petkovšek, Matej Maček in Bojan Majes v prispevku opisujejo raziskave adsorpcije vode po Enslin-Neffu na značilnih slovenskih zemljinah in kamninah ter na referenčnih čistih, monomimeralnih vzorcih. Raziskave kažejo, da je Enslin – Neffov postopek odlično dopolnilo obstoječim postopkom za karakterizacijo zemljin in kamnin.

V članku Zvonka Tomanovića je analiziran vpliv napetostnega stanja na deformacijski odziv kamninske mase na enoosnih, dvoosnih in triosnih preizkušanjih laporja, pri kratkotrajnem obremenjevanju in preizkusih lezenja v trajanju 3 do 180 dni.

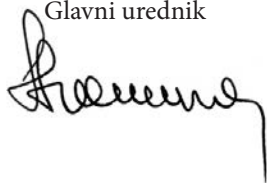
Prispevek avtorja Andreja Gosarja prikazuje oceno seizmičnega vpliva lokalnih tal s pomočjo študije z metodo spektralnega razmerja vodoravnih in navpične komponente (HVSr) mikrotremorjev v 113 merskih točkah na prostem površju.

V članku Izidorja Tasića in Franca Runovca je prikazan razvoj postopka za samodejno zaznavo začetka prihoda valov S iz tri-komponentnega seizmičnega zapisa. Tak, tako imenovani izbiralnik začetka valov S, uporablja Državna mreža potresnih opazovalnic Republike Slovenije za samodejno analizo podatkov o lokalnih potresih.

Gregor Vilhar in Vojkan Jovičić predstavljata merjenje in interpretacijo meritev z bender elementi na meljastem pesku iz Boštanja. Tehnika merjenja z bender elementi je bila uporabljena za določitev dinamičnega strižnega modula materiala pri zelo majhnih deformacijah.

Avtorji Lien-kwei Chien, Tsung-shen Feng in Tsung-ching Chen v članku obravnavajo stisljivi morski melji pod obrežnim valolomom iz gruščnatega nasipa v Ma-Zu-ju na zahodu Tajvana. Rezultati študije so uporabni pri mehaniki morskih meljev in stabilnostnih analizah za planiranje, projektiranje in podobne raziskave v inženirstvu obrežij.

Ludvik Trauner
Glavni urednik



EDITORIAL

The aim of the Editorial Board of Acta Geotechnica Slovenica is to publish high-quality scientific and professional articles, since this is the only route to the journal gaining an international reputation. However, we are aware that we can only achieve this goal with the help of authors who trust us. Therefore, we would like to express our thanks to all those contributors who have chosen our journal to publish their ideas and findings.

Six contributions are published in the current issue, which we decided to extend due to the very interesting themes treated in these articles.

In their article, Ana Petkovšek, Matej Maček and Bojan Majes describe their research on water adsorption according to the Enslin-Neff procedure on typical Slovenian soils and aggregates as well as on reference clean mono-mineral samples. The research shows that the Enslin-Neff method is an excellent addition to the existing procedures for the characterization of soils and aggregates.

In his contribution, Zvonko Tomanović analyses the influence of the stress state on the deformation response of a rock mass on uniaxial, bi-axial and three-axial specimens of marl during short loading and in creep tests for periods of 3 to 180 days.

The article of Andrej Gosar describes an assessment of the seismic influence of local soil with the help of the horizontal-to-vertical spectral ratio (HVSR) method of microtremors at 113 free-field measuring points on a free surface.

Izidor Tasič and Franc Runovc present, in their contribution, the development of the procedure for the automatic picking of the S wave's arrival from three-component seismic data. Such a so-called S-phase picker is used to automatically analyze the data from local earthquakes in Slovenia's seismic network.

Gregor Vihar and Vojkan Jovičić introduce measurements as well as an interpretation of these measurements, based on the use of bender-element probes for Boštanj silty sand. The bender-element technique was used to determine the dynamic shear modulus of the soils at very small strains.

The authors Lien-kwei Chien, Tsung-shen Feng and Tsung-ching Chen describe, in their article, the soft marine silts under a rubble-mound breakwater in Ma-Zu of west Taiwan. The results are useful for marine silts mechanics and a stability analysis for the planning, design, and related research on near-shore engineering.

Ludvik Trauner
Editor-in-chief



LABORATORIJSKA KARAKTERIZACIJA ZEMLJIN IN KAMNIN, KI VSEBUJEJO GLINO, S PREISKAVO ADSORPCIJE VODE PO ENSLIN – NEFFU

ANA PETKOVŠEK, MATEJ MAČEK IN BOJAN MAJES

o avtorjih

Ana Petkovšek
Univerza v Ljubljani,
Fakulteta za gradbeništvo in geodezijo
Jamova 2, 1000 Ljubljana, Slovenija
E-pošta: apetkovs@fgg.uni-lj.si

Matej Maček
Univerza v Ljubljani,
Fakulteta za gradbeništvo in geodezijo
Jamova 2, 1000 Ljubljana, Slovenija
E-pošta: mmacek@fgg.uni-lj.si

Bojan Majes
Univerza v Ljubljani,
Fakulteta za gradbeništvo in geodezijo
Jamova 2, 1000 Ljubljana, Slovenija
E-pošta: bmajes@fgg.uni-lj.si

izvleček

Postopek za merjenje adsorpcije vode na fina zrna zemljin in drugih praškastih materialov je razvil Enslin leta 1933. Postopek so kasneje dopolnjevali različni nemški raziskovalci. Danes je postopek znan kot Enslin – Neff postopek in je vključen v nemške standarde. Kljub temu, da je postopek enostaven, hiter in daje pomembne informacije o obnašanju drobno zrnatih materialov v stiku z vodo, je v ne nemško govorečih deželah praktično nepoznan.

V prispevku so opisani rezultati raziskav adsorpcije vode po Enslin-Neffu na značilnih slovenskih zemljinah in kamninah ter na referenčnih čistih, monomimralnih vzorcih. Izmerjene vrednosti adsorpcije vode so primerjane z Atterbergovimi mejami plastičnosti, Metilen modro vrednostjo in vsebnostjo vode na značilnih točkah retencijske krivulje in pri značilnih sukcijah. Rezultati kažejo na direktno zvezo med mejo židkosti in adsorpcijo vode po Enslin – Neffu, ki jo je možno zapisati z enostavno enačbo. Ugotovljeno je tudi, da vrednost adsorpcije vode ustreza prvi točki na deviški retencijski krivulji pri nični sukciji. Zveze med adsorpcijo vode in metilen modrim ni možno zapisati z enotno, splošno veljavno enačbo, ker je v meritvi po Enslin – Neff vključena kapilarna in adsorpcijska voda, metilen modro pa zaznava le adsorpcijski potencial zrn za organsko barvilo metilen modro. Pridobljeni rezultati kažejo, da obstaja zveza med vrednostjo Metilen modro in adsorpcijo vode, vendar bo potrebno za matematični opis te zveze opraviti še dodatne raziskave.

Raziskave kažejo, da je Enslin – Neff postopek odlično dopolnilo obstoječim postopkom za karakterizacijo zemljin, kamnin in finih zrn v kamenem agregatu. Prednost postopka pred Atterbergovimi mejami plastičnostmi je zlasti v hitrejši in enostavnejši izvedbi ter predvsem v majhni količini vzorca, potrebni za raziskavo.

ključne besede

adsorpcija vode, Atterbergove meje plastičnosti, metilen modro vrednost, retencijska krivulja, zemljinska sukcija

A LABORATORY CHARACTERIZATION OF SOILS AND CLAY-BEARING ROCKS USING THE ENSLIN-NEFF WATER-ADSORPTION TEST

ANA PETKOVŠEK, MATEJ MAČEK and BOJAN MAJES

About the authors

Ana Petkovšek
University of Ljubljana,
Faculty of Civil and Geodetic Engineering
Jamova 2, 1000 Ljubljana, Slovenia
E-mail: apetkovs@fgg.uni-lj.si

Matej Maček
University of Ljubljana,
Faculty of Civil and Geodetic Engineering
Jamova 2, 1000 Ljubljana, Slovenia
E-mail: mmacek@fgg.uni-lj.si

Bojan Majes
University of Ljubljana,
Faculty of Civil and Geodetic Engineering
Jamova 2, 1000 Ljubljana, Slovenia
E-mail: bmajes@fgg.uni-lj.si

Abstract

The application of the Enslin-Neff water-adsorption test for the determination of soil-index properties has been investigated on commercially available reference minerals and on real soils. The Enslin-Neff test is a simple and reliable laboratory method, which can provide important information about the behavior of soils, clay-bearing rocks and aggregate fines that are in contact with water. Although the test has been frequently used for bentonite testing, practically no results have been published about the physical meaning of the Enslin-Neff water-adsorption values for real soils. The results of this study indicate that the Enslin-Neff water-adsorption test can be used to obtain accurate values of some soil-index properties, such as the liquid limit, the plasticity index, the methylene-blue value, and the soil-water characteristic curve.

Keywords

water adsorption, methylene blue value, soil water characteristic curve, soil suction

1 INTRODUCTION

A test method for determining the water-adsorption capacity of powders was proposed by Enslin in 1933. It was found to be applicable to viscous silk, cellulose, paint, glue, gelatine, adhesives based on starch, soils and some other substances. The method has, however, been improved several times since then [1]. Today, the method is included in the German industrial norm DIN 18 132 [2], and is known as the Enslin-Neff water-adsorption test (w_A). The test is widely used in clay mineralogy and in the production of bentonite for quality control [3]. Although the Enslin-Neff method is simple, quick to perform, inexpensive and can give important information about the nature and the behaviour of geological materials, practically no results have been published about the physical meaning of Enslin-Neff water-adsorption values for real soils and clay-bearing rocks. Available publications, mostly published by German researchers, deal with improvements to the method [4], [5], the reproducibility of the results [1], and the comparability of the results with the Atterberg-limits values [6]. Dieng [6] investigated natural soils, bentonites and kaolinitic clays, and laboratory-prepared mixtures of kaolin and bentonite with limestone, as well as laboratory-prepared mixtures with lime and organic material in order to define the relationship between the water-adsorption value and the Atterberg-limits values (w_L and I_P). Based on the results of his experiments, he defined the relationships between the w_A and w_L and I_P values as follows:

For soils with:

$$w_A + 0.3 w_{Ai} \leq 210\% \quad (1)$$

$$w_L = 0.61(w_A + 0.3 w_{Ai}) \quad (2)$$

when: $w_A > 40\%$

$$I_P = 0.28(w_A + 0.3 w_{Ai}) - 5 \quad \text{kaolin} \quad (3)$$

$$I_P = 0.51(w_A + 0.3 w_{Ai}) - 13 \quad \text{other soils} \quad (4)$$

For soils with:

$$w_A + 0.3 w_{Ai} > 210\% \quad (5)$$

$$w_L = 1.13(w_A + 0.3w_{Ai}) - 126 \quad (6)$$

$$I_P = 1.1(w_A + 0.3 w_{Ai}) - 140 \quad (7)$$

Dieng [6] defined the value of w_{Ai} as a function of water adsorption after 100 minutes (w_{A100}) and water adsorption after 5 minutes (w_{A5}):

$$w_{Ai} = w_{A100} - w_{A5} \quad (8)$$

Compared with the Atterberg-limit values for soil classification, the advantage of the Enslin-Neff method is that only a very small sample, about 3 grams, is needed for the test. This means that the test could be used to identify the nature of soils, rocks and aggregate fines even in cases when other test methods cannot be used due to the lack of samples of an adequate size, for instance when studying fine-layered or fractured expansive clay-bearing rocks and the slip surfaces of rocks, when testing the nature of fines in the aggregate production industry, for forensic and other purposes.

This paper presents the results of a study in which the results obtained for the Enslin-Neff water adsorption (w_A) were compared with those obtained by a test of the Atterberg limits (w_L , I_P), the methylene-blue test (MB_f), and the soil-suction measurements for determining the soil-water characteristic curve (SWCC) [7].

2 METHODS

Water-adsorption values were determined according to the German norm DIN 18 132 [2] using a conventional Enslin-Neff device (Figure 1). Oven-dried samples with weights of 0.3 grams, in the case of bentonites, and 1 gram in the case of other powders, were placed on the frit using the recommended funnel method. For each material in the experiment, three parallel tests were performed in order to check the reproducibility. The readings of the burette were recorded continuously, with the first reading after 15 seconds, and then following the power law. The final reading was taken after 24 hours. The effect of evaporation from the burette was determined prior to the experiment. With the increasing duration of the test the effect of evaporation on the readings increases. For most of the soil samples in the experiment, the water uptake in the sample was finished after 15 minutes. For the reference bentonites the readings lasted for more than 24 hours, so that the error due to evaporation could be relatively large.

For the purpose of this study, the readings after 24 hours were used as a reference for all three bentonites.

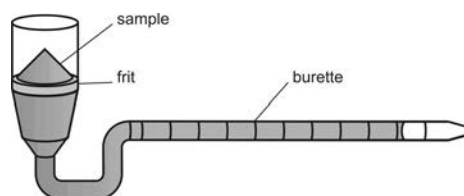


Figure 1. The Enslin-Neff device used in the experiment.

The Atterberg-limits test was determined according to the standard SIST TS CEN ISO/TS 17892-12:2004 [8]. For the determination of the liquid limit a 60g/60° cone was used. The reference samples were used in the natural state, without sieving, whereas in the case of the real soil and clay-bearing rocks, only fines passing through a 0.063-mm sieve were used.

The methylene-blue value, expressed as MB_f , was determined using the standard method defined in SIST EN 933-9:1999 [9]. The qualitative mineralogical composition was determined by X-ray diffraction analysis using a Phillips device with Cu K α radiation.

The soil suction at low suction rates was determined by the axial-translation technique, using a soil-moisture pressure-plate device. Saturated samples that had been prepared at a water content equivalent to the liquid limit or slightly higher were placed on a porous plate with a high air-entry value, and then maintained at the chosen cell air pressure of 10 kPa, 33 kPa and 100 kPa. At suction rates higher than 100 kPa, a Decagon chilled-mirror dew-point potentiometer was used for the tests.

3 MATERIALS

For the purpose of this study, 134 samples were prepared and tested. The five reference samples consisted of commercially available materials: non-active limestone flour, brick clay and Na⁺ and Ca²⁺ bentonites. All the other samples were taken from typical Slovenian soils and clay-bearing rocks, and consisted of mixtures over a wide spectrum of different minerals: Eocene flysch marl and claystone, Oligocene highly overconsolidated grey marine clay and marl, Miocene marl, Pliocene overconsolidated clays from the Sub Pannonian basin, and Pliocene karstic clays (terra rosa). Quaternary alluvial and deluvial soils, taken from weathered zones in alluvial gravels, carbonatic, ultramafic and metamorphic phyllonites were also included in the test program.

Table 1. Characteristics of the soils used in the research.

Sample	w_L %	I_P %	w_A %	MB_f g/kg	$w_{s1500kPa}$ %	Dominant mineral*
Bentonite Wyoming	535	490	778	336		M_{Na}
Bentonite Macedonia	207	172	297	176	46	M_{Ca}
Bentonite Slovenia	83	56	113	172		M_{Ca}
Brick clay Slovenia	53	36	73	57	14	I/C
Stone flour Slovenia	23	-	32	2	1	Ca, $CaCO_3$: 99 %
Oligocene marine clay	41-48	26-29	62-70	48-25	11-12	MM:I/K/Ca/Q/
Eocene flysch	42-50	25-32	56-64	56-60	11-13	MM: I/K/Calc/Q/
Miocene marl	39-53	15-34	56-74	20-31	7-11	MM: I/K/M/Calc/Q/
Pliocene clay	52-85	25-57	67-88	61-62	11-23	MM: I/K/M/Q/mica
Pliocene karstic clay	63-122	41-89	83-121	8-13	20-35	L/Mn/Ca/Q
Alluvial clay	67-68	49-51	78-82	38-40	14-15	MM: I/K/M/Q
W – gravel river alluvium	37-42	8-16	47-55	3-12	3-7	MM
W - dolomite	21-38	6-20	29- 51	2-34	2-11	MM: D/I/C
W – phyllonite	27-40	8-19	41-57	7-11	3-9	MM:Sc/C/B/Q
W – serp. harzburgite	40-78	19-42	68-116	28	13-16	S/C/L/O

* M_{Na} – Na montmorillonite > 70 %; M_{Ca} – Ca montmorillonite > 70 %, I- illite/muscovite, B – biotite, C – chlorite, Ca – calcite, D – dolomite, L – limonite, MM – wide mineral mixture, Mn – manganese oxide, O – olivine, Q – quartz, S – serpentinite, Sc – sericite, W – weathered products inside the bedrock

4 RESULTS AND DISCUSSION

The results for the Atterberg-limit values, the Enslin-Neff water absorption, the methylene blue, the water content at a soil suction equal to 1500 kPa and the prevailing mineral composition are given in the ranges for the representative samples of the typical groups of soils (Table 1).

The liquid limits and the plasticity indexes of the tested soils are presented for all the samples in Figures 2 and 3. The reference samples (commercially available materials) are indicated in the key in each diagram. The reference clayey samples were found to be located close to the same straight line, which corresponds to the U-line in the AC diagram, whereas most of the tested real soils

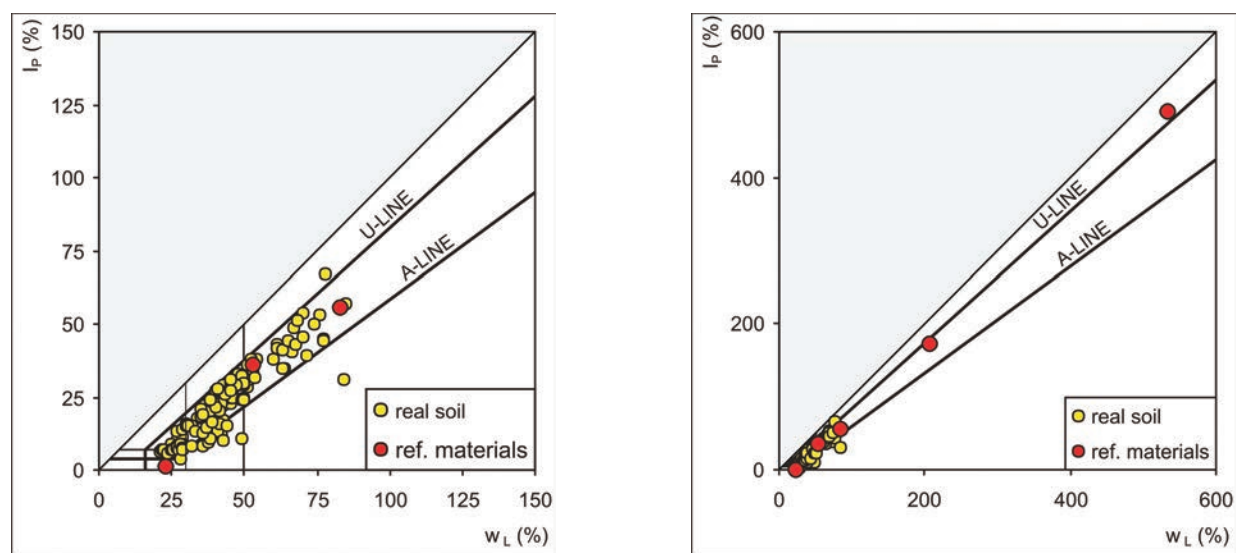


Figure 2. Position of the tested soils in the AC diagram, limited scale (left) and complete scale (right).

lie above the A-line (Figure 2). The U- and A-line are defined as in the ASTM standard D 2487-00 [10], where the U-line is defined as the empirically determined approximate “upper limit” for the natural soil and the A-line as the border line between silts and clays.

4.1 RELATIONSHIP BETWEEN THE ENSLIN-NEFF WATER-ADSORPTION TEST AND THE ATTERBERG-LIMITS TEST

The Atterberg-limits test is one of the most widely used tests in soil mechanics for classification purposes, although it is partially subjective and requires experienced laboratory staff. At least 200 g of soil is needed for the test, which is quite inconvenient, especially when thin layers of highly expansive clay are encountered inside the bedrock mass or when coarse material with a low fines content has to be tested. However, the Enslin-Neff test is a promising test that could overcome the shortcomings of Atterberg’s soil-classification test.

The experimentally determined relationship between the Atterberg liquid-limit test and the Enslin-Neff water-adsorption test is given in Figure 3.

For the reference materials an excellent correlation was found between w_A and w_L and the corresponding simple equations can be written as:

$$w_L = 0.69 w_A \quad (9)$$

$$w_A = 1.45 w_L \quad (10)$$

For the real soils, the values of the coefficient in equation (10) can vary between 1.13 and 1.77. The experimentally defined relationship is close to that proposed by Dieng [6], but it is expressed in a much simpler form.

For the real soils the scattering of the results seems to increase with the increasing liquid limit (Figure 3). Therefore, the coefficient w_A/w_L was calculated for all the samples and the standard deviation was determined to be 0.2. Figure 4 presents the distribution of the coefficient w_A/w_L and the normal distribution for the determined standard deviation and coefficient w_A/w_L . The liquid limit, w_L , could be calculated with a 10% accuracy from the real measurement by using equation (10) for more than 50% of the samples (for example, $w_L=40\%$ in the range 36–44%).

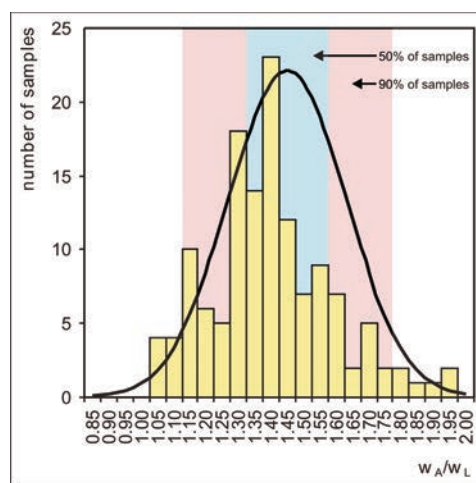


Figure 4. Grouping of the soils following the position in the AC diagram.

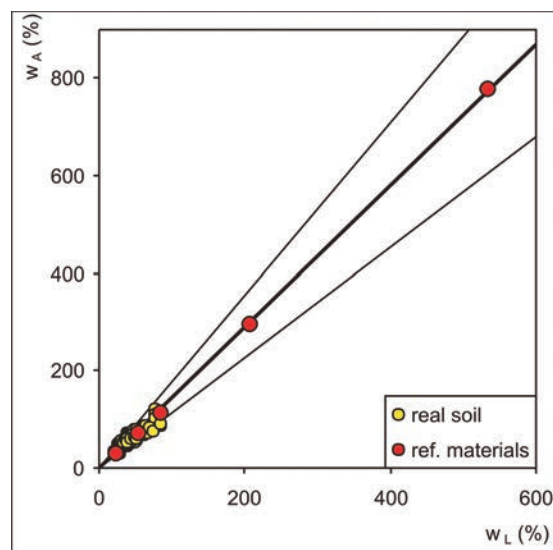
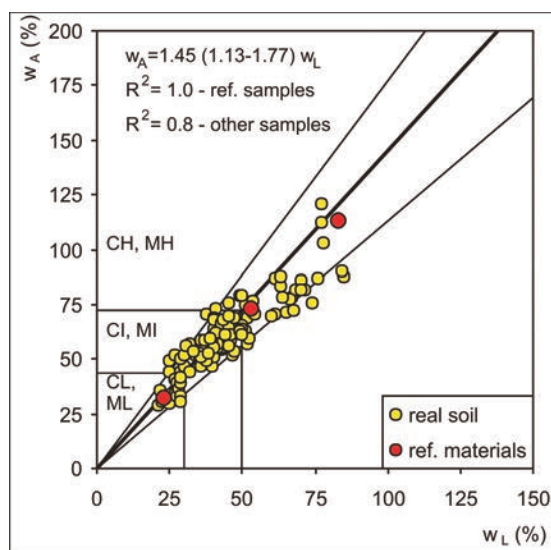


Figure 3. Enslin-Neff water adsorption as a function of the liquid limit, limited scale (left) and complete scale (right).

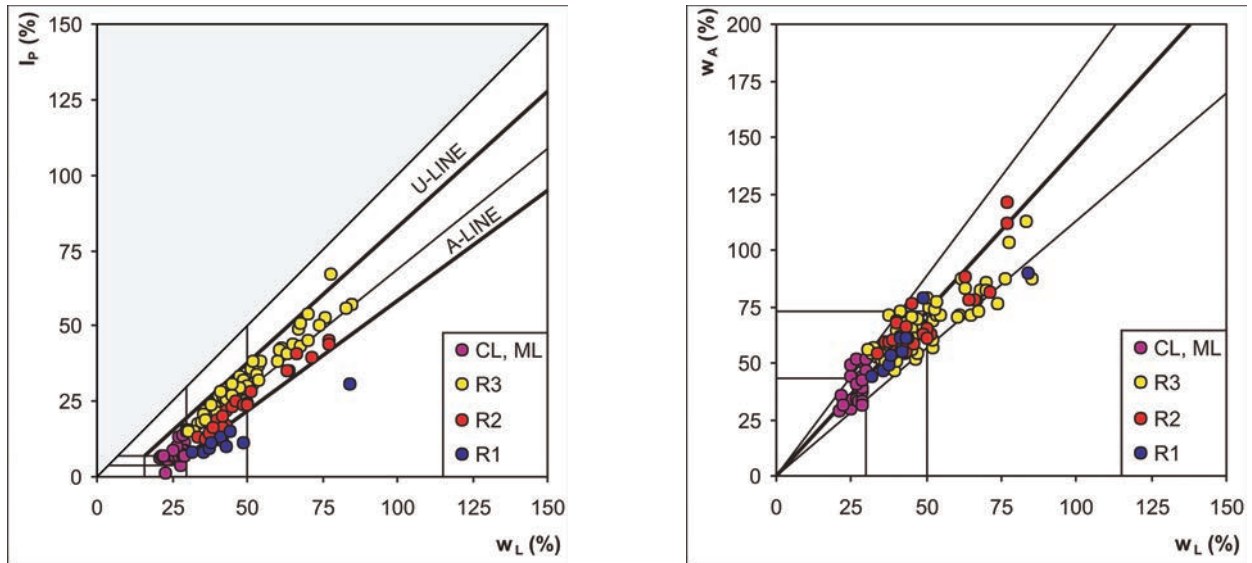


Figure 5. Grouping of soils following the position in the AC diagram (left) and the relationship w_L-w_A (right).

To explain the influence of the different types of soils on the ratio w_A/w_L , the samples were divided into four groups: lean clays and silts represent a special group with a liquid limit $w_L < 30\%$, whereas the groups R1, R2 and R3 were defined according to the soil position in the AC classification diagram (Figure 5).

From Figure 5 it can be concluded that the type of soil does not influence the relationship w_A/w_L and that equation (10) is valid for all types of soils. However, for the relationship between w_A and I_p (Figure 6) these findings are not valid.

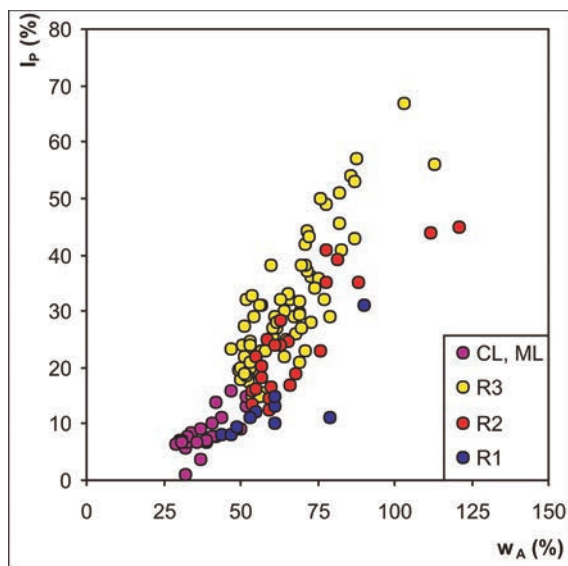


Figure 6. The index of plasticity as a function of water adsorption and soil group.

The results of the experiments show that both values, i.e., w_A and w_L , have similar physical meanings when describing the clean mono-mineral soils as well as the real heterogeneous soils. In the case of both tests, the measured water content belongs to the water adsorbed to the external and internal surfaces of the grains. However, the water content at the liquid limit corresponds to an undrained shear strength of $c_u = 1.6$ kPa [11], but does not correspond to the maximum void ratio (e_{max}). The sample on the frit in the Enslin-Neff device is in the loosest state, and is completely saturated when the test is finished. The water content obtained from the Enslin-Neff test is therefore higher than the water content at the liquid limit for the specific soil.

The results of the experiments also confirmed that the Enslin-Neff method could replace or provide an excellent complement to the liquid-limit test, especially in cases when limited quantities of samples are available for the test, or when it is difficult to perform the liquid-limit test, as in the case of Na^+ bentonites or low plastic soils and micas.

4.2 RELATIONSHIP BETWEEN THE ENSLIN-NEFF WATER-ADSORPTION TEST AND THE METHYLENE-BLUE VALUE

It is well known that the specific surface area (SSA) and the cation-exchange capacity (CEC) influence the behaviour of clay in contact with water and water solutions. For more than 40 years the methylene-blue (MB) test has been recognized as a rapid and easily applicable test for

SSA and CEC determination [12], [13], [14], [15], and different classification charts for predicting the swelling potential of soils are based on MB values [13], [15], [16]. In its aqueous state methylene blue is a cationic dye, $C_{16}H_{18}N_3S^+$, which can adsorb onto negatively charged surfaces. The MB molecule has a rectangular shape with the dimensions $17 \text{ \AA} \times 7.6 \text{ \AA} \times 3.25 \text{ \AA}$, and it is assumed that the MB molecule lies on its largest surface [15]. No special equipment is needed for the test. The MB value is determined by measuring the quantity of methylene-blue dye necessary to cover the total (external and internal) surface area of the particles contained in the soil.

From this point of understanding, the Enslin-Neff and the MB tests exploit similar phenomena – the adsorption of water molecules or positively charged dye cations onto negatively charged external and internal particle surfaces. It can therefore be assumed that the correlation between the MB and Enslin-Neff must exist in soils that contain negatively charged surfaces, and where the amount of adsorbing water prevails over the amount of capillary water.

The experimentally determined relationship between the MB_f and w_A values is given in Figure 7. It can be seen that there is no unique and linear relationship between the two measured parameters, which is probably due to the influence of the capillary water and of the different sizes of the adsorbing molecules. The concentration of the results at lower values of MB_f ($MB_f < 15 \text{ g/kg}$) belongs to the silty soils (group R1), where most of the water in the soil belongs to the capillary water and the particles can be estimated as inert. At values of $MB_f > 15 \text{ g/kg}$ the correlation between MB_f and w_A can be expressed as a potential

function with a correlation coefficient of $R^2 = 0.54$. The correlation coefficient was only calculated for the real soils. The reference bentonites were not included, since the small number of these samples with positions far away from the centre of the group would have drastically improved the correlation coefficient R^2 .

However, in the literature it has been reported that the MB shows a high dependency of the adsorption on the type of cations in/on the clay. Researchers have reported that the adsorption of the MB dye is only complete when the sample is in the lithium and sodium exchanged form [15]. From this point of view it is too early to recognize the Enslin-Neff test as a method that could successfully replace the MB test, but it can certainly complement it. The results of the research are promising and show that these investigations should be continued, taking into account the influence of the specific cation-exchange capacity and the specific surface area of the tested soils on both of the measured parameters.

4.3 ENSLIN-NEFF WATER ADSORPTION – SWCC

The soil-water characteristic curve (SWCC) is a continuous sigmoidal function, representing the relationship between the water content (gravimetric or volumetric) or the saturation degree and the stress state of the pore water. Many soil properties can be related to SWCC, such as the volume change, the hydraulic conductivity and the shear strength. The SWCC has three stages that describe the process of desaturation of a soil: the capil-

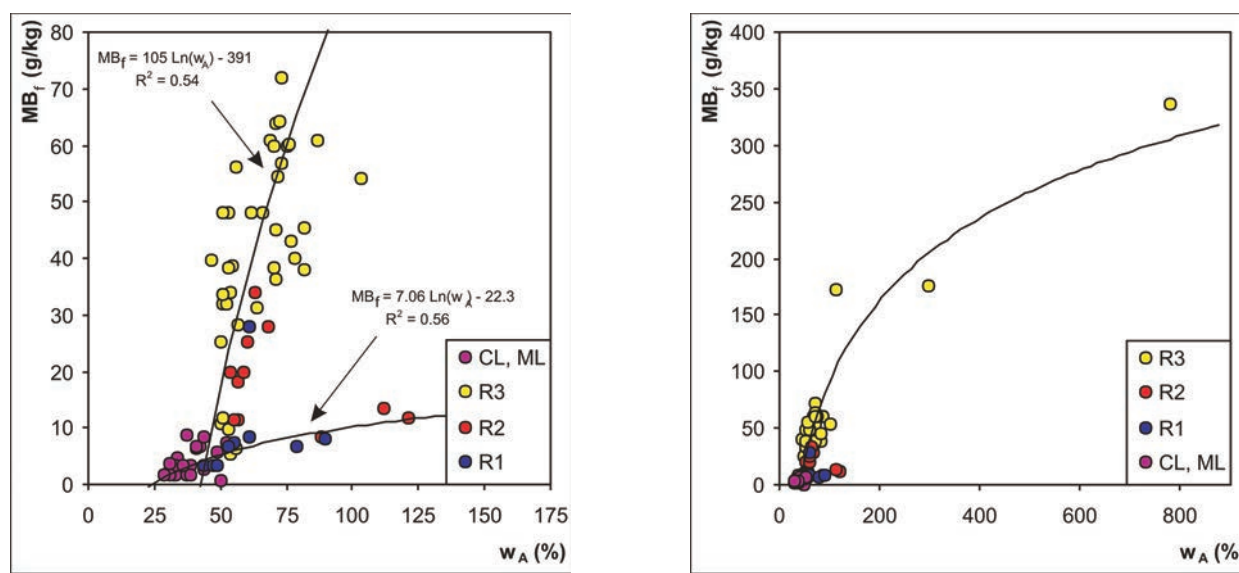


Figure 7. The $MB_f - w_A$ relationship, limited scale (left), complete scale (right).

lary saturation zone, where the pore water is in tension but the soil remains saturated due to capillary forces; the desaturation zone, where the water is displaced by air within the pores; and the residual saturation zone, where the water is tightly adsorbed onto the soil particles and flow only occurs in the form of vapour [7].

The capillary saturation zone ends at the air-entry value, where the applied suction overcomes the capillary water forces in the soil and air enters the pores. The amount of water in the soil or the water content at a certain suction stress depends on the soil's density and the soil's stress history. However, each type of soil has a characteristic maximum void ratio in its loosest state (e_{max}), at which it can hold the highest amount of water in the saturated state (at zero suction). This point corresponds to the first point on the SWCC, which can be called, following the

similarity with the saturated soil oedometric compression curve, the "virgin" SWCC.

The laboratory tests for SWCC determination at low suction usually start on samples that have been prepared at the liquid limit, which means that the soil is no longer in the loosest state. Following the description of Dieng [6], the Enslin-Neff water adsorption can correspond to the first point on the "virgin" SWCC at which the soil pores and the diffusive double layers are filled with water. A relationship between the water content at zero suction and the water content at the residual water content must therefore be expected.

Figure 8 shows the SWCC curves of four representative soils used in the investigation. For each soil sample the experimentally determined soil suctions are given for

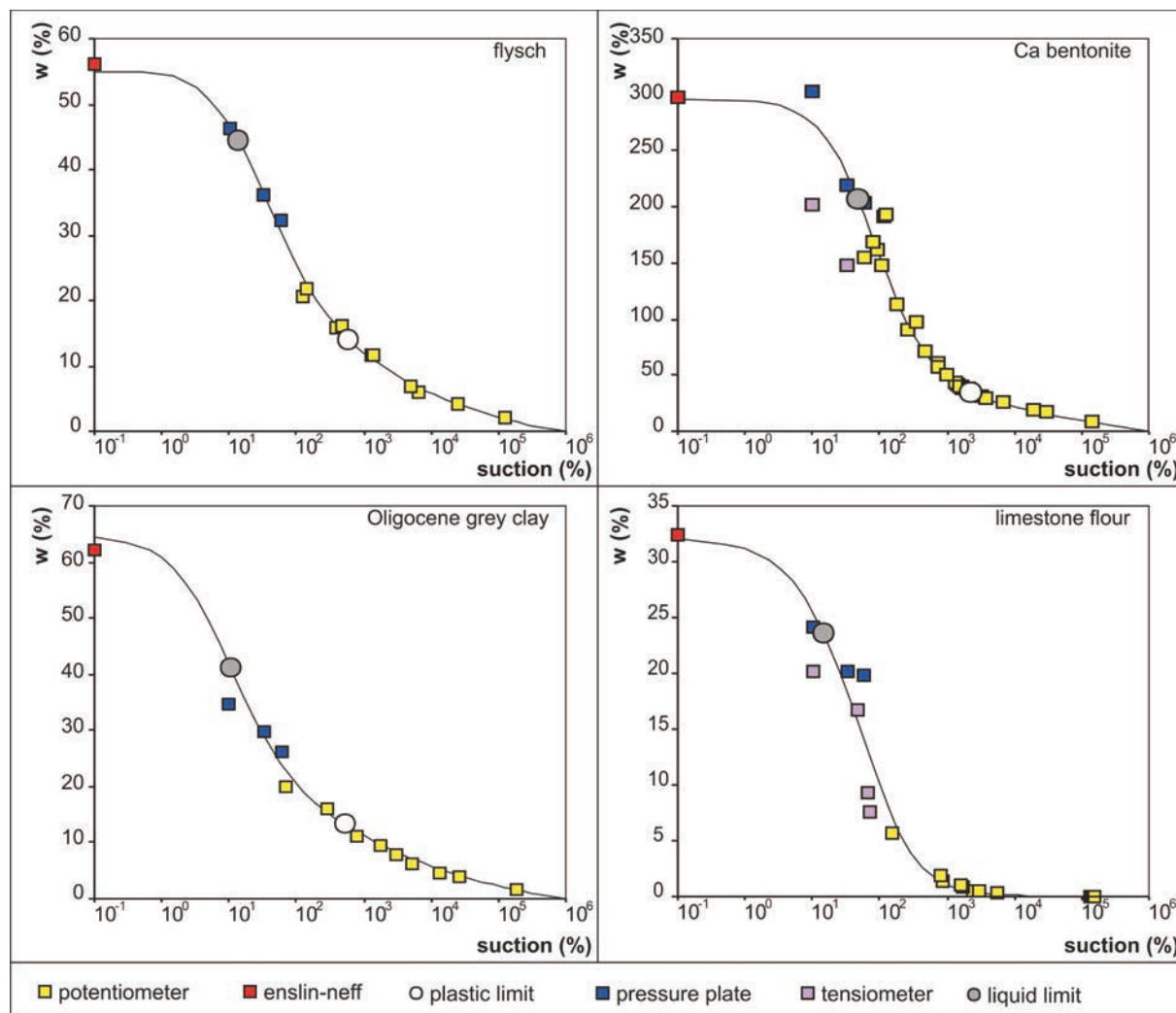


Figure 8. SWCC curves for four representative soils with the positions of the liquid limit and the plastic limit.

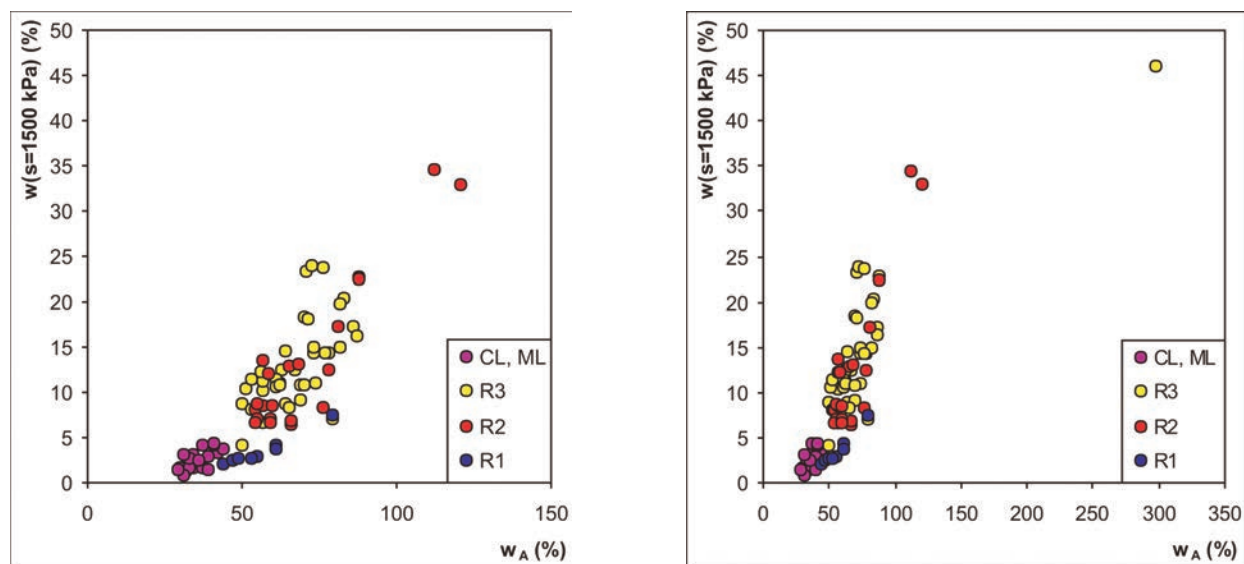


Figure 9. Water content at a suction of 1500 kPa, as a function of w_A .

certain water contents, and the values of w_A , w_L and w_p are indicated in the graph. The SWCC is described using the Fredlund–Xing equation [17]. Different researchers have investigated suction at the liquid and plastic limits of different soils and have found different corresponding values between 0.5 and 30 kPa [18], [19], [20].

The typical results presented in Figure 8 show that the magnitude of the suction at the liquid limit of each specific soil depends on its Enslin-Neff water adsorption. This means that the value w_A , which corresponds to the maximum water content at zero suction, also controls the suction at the liquid limit.

The relationship between w_A and the water content at a suction of 1500 kPa is given in Figure 9. At least two different types of behaviour can be observed. The first type belongs to the soil group R1, for which the w_A values are lower than 80%, and it corresponds to a water content at a suction of 1500 kPa of less than 7.5%. The second type belongs to the soils with w_A values higher than 50% and a water content at a suction of 1500 kPa of more than 7.5%. The amount of experimental data is too small to describe the relationship between the two parameters, but the Enslin-Neff water adsorption could be estimated as the first point on the virgin SWCC.

5 SUMMARY AND CONCLUSION

An experimental program was conducted in the laboratory with the aim of examining the physical meaning of Enslin-Neff water adsorption (w_A) in terms of some of the

more widely known index properties of soils: the Atterberg limits, the MB_f value and the SWCC. Real soil samples with different origins and mineralogy were used, together with clean, commercially available limestone flour, brick clay and bentonites, to determine whether the results are comparable for different adsorption ranges. The following conclusions may be drawn from the investigation:

- Linear trends are evident in the relationship between the Atterberg limits and the Enslin-Neff water adsorption. This observation confirmed the results published by Dieng [6]. By introducing a simplified equation (9), the classification of cohesive soil or fines can be reasonably predicted from the Enslin-Neff test. The Enslin-Neff test is faster, requires a very small sample, and is less subjective than the Atterberg-limits test.
- Trends are indicated in the relationship between the MB_f and the Enslin-Neff above values of $w_A > 60\%$. The strong influence of the nature of the exchangeable cations on the MB_f needs further investigation in the direction of the MB_f and the w_A relationship. However, the obtained results are promising, and could be complemented by further investigations.
- The w_A was recognized as being probably the first point on the “virgin” SWCC. Special connections were recognized between the w_A and the water content at the permanent wilting point. From this point of view, the Enslin-Neff test provides new possibilities for its use in the field of swelling-soil classification methodology after additional testing and certain modifications.

The experimental results have confirmed the wide possibilities for the extended use of the Enslin-Neff method in the laboratory for soil and rock mechanics and for the testing of aggregates. It is especially suitable for soil classification and the preliminary estimation of the possible volume changes of soils and clay-bearing rocks. As it is less subjective than the Atterberg-limits test and the MB titration method, it is a pity that the method has remained almost forgotten and was not introduced to soil mechanics laboratories earlier.

REFERENCES

- [1] Kaufhold, S., Dohrman, R. (2008). Comparison of the traditional Enslin-Neff method and the modified Dieng method for measuring water-uptake capacity. *Clays and Clay minerals*, 56, 6, 686 -692.
- [2] DIN 18 132:1995. Messung der Wasseraufnahme von Boden.
- [3] Böhler, U. (1993). Der Wasseraunahmeversuch nach Enslin-Neff zur Qualitätskontrolle im Deponiebau. *Müll and Abfall*, 11/93, 813 -820.
- [4] Demberg, W. (1991). Über die Ermittlung des Wasseraufnahmevermögens feinkörniger Böden mit dem Gerät nach Enslin-Neff. *Geotechnik*, 14, 125 -131.
- [5] Dieng, M. A. (2005). Der Wasseraunahmeversuch nach DIN 18132 in einem neu entwickelten Gerät, *Bautechnik* 82, Heft 1, Ernst&Sohn, Berlin, 28-32.
- [6] Dieng, M. A. (2006). Bestimmungsmethode der Konsistenzgrenzen mittels Wasseraufnahmeversuchen, *Bautechnik* 83, Heft 7, Ernst&Sohn, Berlin, 492 - 496.
- [7] Fredlund, D.G., Rahardjo, H. (1993). *Soil Mechanics for unsaturated Soils*. John Wiley & Sons. New York.
- [8] SIST-TS CEN ISO/TS 17892-4:2004 Geotechnical investigation and testing – laboratory testing of soil – Part 4: Determination of Atterberg limits (ISO/TS 17892-12:2004).
- [9] SIST EN 933-9:1999 Test of geometrical properties of aggregates – Part 9: Assessment of fines – Methylene blue test.
- [10] ASTM D 2487 – 00 Standard Practice for Classification of Soils for Engineering Purposes (Unified Soil Classification System).
- [11] Dolinar, B. (2004). Undrained shear strength of saturated cohesive soils depending on consolidation pressure and mineralogical properties. *Acta Geotechnica Slovenica*, 1, 5-11.
- [12] Hang P T, Brindley G W (1970) Methylene blue adsorption by clay minerals. Determination of surface areas and cation exchange capacities (Clay – organic studies XVIII). *Clay and clay minerals*, 18, 203-212.
- [13] Çokça, E. (2002). Relationship between Methylene blue value, initial soil suction and swell percent of Expansive Soils. *Turkish Journal of Engineering and Environmental Sciences*, 26, 521 – 529.
- [14] Chiappone, A., Marelllo, S., Scavia, C. and Setti, M. (2004). Clay mineral characterization through the methylene blue test: comparison with other experimental techniques and application of the method. *Canadian Geotechnical Journal*, 41, 1168-1178.
- [15] Yukselen, Y., Kaya, A. (2008). Suitability of the methylene blue test for surface area, cation exchange capacity and swell potential determination of clayey soils. *Engineering Geology* 102, 38-45.
- [16] Petkovšek, A. (2006). *The influence of matrix suction on the strength and stiffness of soils*. Ph.D. thesis. University of Ljubljana, UL – FG, 168, 273.
- [17] Fredlund, D.G., Xing, A. (1994). Equations for the soil water characteristic curve. *Canadian Geotechnical Journal*, No. 31 (3), 521- 532.
- [18] Fleureau, J. M., Verbrugge, J. C., Huergo, P. J., Correia, A. G., Kheirbeck – Saoud, S. (2002). Aspects of the behaviour of compacted clayey soils on drying and wetting paths. *Canadian Geotechnical Journal*, 39: 1341–1357.
- [19] McKeen, R. G. (1992). A model for predicting expansive soil behavior. *7th International Conference on Expansive Soils*, Dallas, 1, 1-6.
- [20] Nelson, J. D., Miller, D. J. (1992). *Expansive soils: problems and practice in foundation and pavement engineering*. John Wiley & Sons. New York.

VPLIV K_0 NA KARAKTERISTIKE LEZENJA LAPORJA

ZVONKO TOMANOVIĆ

O avtorju

Zvonko Tomanović
Univerza v Podgorici,
Fakulteta za gradbeništvo
Cetinjski put bb, 8100 Podgorica, Črna gora
E-pošta: zvonko@t-com.me

Izvleček

Analiziran je bil vpliv napetostnega stanja na deformacijski odziv kamninske mase na enoosnih, dvoosnih in triosnih preizkušancih laporja, pri kratkotrajnem obremenjevanju in preizkusih lezenja v trajanju 3 do 180 dni. Bočni (horizontalni) pritisk bistveno spremeni deformacijski odziv, tako začetnih deformacij povzročenih zaradi spremembe napetosti, kot tudi deformacij lezenja. Vpliv bočnega pritiska na vertikalno deformacijo je možno dobro aproksimirati z linearno funkcijo.

Ključne besede

lezenje, mehke kamnine, lapor, reološki model, bočna napetost, laboratorijske preiskave

INFLUENCE OF K_0 ON THE CREEP PROPERTIES OF MARL

ZVONKO TOMANOVIĆ

About the author

Zvonko Tomanović
University of Montenegro,
Faculty of Civil Engineering,
Cetinjski put bb, 8100 Podgorica, Montenegro
E-mail: zvonko@t-com.me

Abstract

The influence of the stress state on the deformation response of a rock mass has been experimentally examined on uniaxial, bi-axial and three-axial specimens of marl at short loading and in creep tests for periods of 3 to 180 days. The lateral (horizontal) pressure significantly changes the deformation behaviour of both the initial deformations induced by the stress change and creep deformations. The influence of lateral pressure on the vertical deformation can be well approximated by a linear function.

Keywords

creep, soft rock, marl, rheological model, lateral stress, laboratory testing

1 INTRODUCTION

In order to formulate the rheological model for soft rocks with time-dependent deformations presented in this paper, laboratory creep tests were carried out on marl. While formulating the rheological model, specific rheological material coefficients and parameters need to be defined. The task therefore becomes more complex, because, on the one hand, a mathematical model is required to encompass as many characteristics of the materials as possible; while, on the other hand, the number of parameters and the constants of the materials quantifying those characteristics is limited by the real

possibility to define parameters, i.e., material constants by measurements "in situ" or on specimens in the laboratory.

The rheological modelling of rock mass represents an extremely complex problem and thus while formulating the mathematical model, no matter how complex it is, it is necessary to make certain approximations. The level of the approximations, on one hand, in the model should provide the necessary accuracy of the results of the considered stress-deformation phenomenon of the rock mass, and on the other hand, it should enable a simple determination of the material constants and parameters used in the mathematical model.

Most of the research referring to rock behaviour in the conditions of long-term loading at room temperature published so far has been carried out on samples of rock salt [3-11]. There are also fewer published experimental research articles on the room-temperatures behaviour of marl or similar rocks, characterized by significant creep deformations [2-8], representing a real work environment under which many underground structures are constructed.

Various authors published a number of mathematical models that define rock creeping, which are mainly based on the results of tests on rock salt with significant deformation over time. A far smaller number of developed constitutive relations, which include rock creeping, can apply a correct description of different phenomena in rock mechanics due to their general character, in terms of the type of rock material and the direction of the stress and stress states. Due to the previously mentioned, it is necessary to examine the behaviour of different types of rocks, and thus in the first place to develop the most common constitutive models that can adequately describe their time-dependent stress-strain behaviour.

Experimental research on marl specimens, part of which is presented in this paper, under conditions of short-term loading, long-term load and unloading was

conducted for the purpose of the formulation of a rheological model of the behaviour of soft rock under different stress conditions. It is also important and necessary to provide the appropriate material parameters of the rock matrix, which was the objective of this experimental research, through the testing of marl as a selected representative rock from the group of soft rocks.

Uniaxial tests are relatively easy to perform, which makes it possible to obtain the material parameters that correspond with the uniaxial stress state. Having in mind the previously mentioned, creep tests were carried out on uniaxial marl specimens and based on the obtained data, the rheological model was formulated and the material constants and parameters were obtained. The stress state during the analysis of the stress-deformation phenomenon in rock mechanics, for example, the stress state of tunnel tubes, significantly departs from the uniaxial state. Due to that, along with uniaxial tests, tests on bi-axially loaded plate specimens were performed under conditions of the plane stress state and the application of different forces in the vertical and horizontal directions as a simulation of the different primary stress states. A number of short creep tests in a conventional three-axial cell with a rotation symmetrical stress state were conducted.

Based on the creep tests on uniaxial specimens, material constants and the substantial parameters of the materials were obtained, and the rheological model was formulated for uniaxial stress, which describes the stress-deformation behaviour of the materials under the conditions of short- and long-term load [10]. Furthermore, a comparative analysis resulted in the establishment of a correlation between all the deformations at the uniaxial, bi-axial and three-axial rotation symmetrical stress states. This enables a good evaluation of the complete time deformation with complex stress states based on simple tests on uniaxially loaded specimens. This paper presents the results of a three-year laboratory testing on marl under short- and long-term loading and unloading, which refers to the impact of K_0 on the creep properties.

2 SAMPLING AND MATERIAL PROPERTIES OF THE TESTED MARL

The block was taken out from a section above coal deposits from the "Potrlica" coal mine in the town of Pljevlja (northern Montenegro), from a bench that

mainly consists of a thick layered marl. The thickness of the marl layer varies from several to over 100 meters (marl layers mostly lie directly on the coal deposits). A complex layer of marl, 80-100 cm thick, estimated as suitable, was chosen to be taken out as a block (suitable in terms of the dimensions of a specimen for the following laboratory testing), which is shown with arrows in Fig. 1. The layer is at a 15-20 m depth from the actual natural surface of the terrain, but it took more time to do the excavations at 1-3 metres from the surface of the bench.

The marl block that was taken out was a relatively regular form, 380x90x80 cm. A boring mining hole was made in the block and it clearly indicated the natural position of the block, that is, it defined the vertical direction in its natural position. The prismatic and plate specimens for testing were obtained by cutting, and the cylindrical samples were obtained by taking out the core using the rotation drill.

The tested marl, according in its chemical contents, contains about 48% CaCO_3 , while the content of the insoluble remainder (clayey+quartzite) is nearly 52%. Regarding the mineralogical contents, calcite (46-48 %) and quartz (12-13 %) represent the dominant mineral phases, while in the clayey phase there are illite and smectite, montmorillonite, kaolinite, glauconite, transformed feldspar and mica. The sample moisture was 8-11%, which is why all the stress-deformation analyses were given for the total stresses. The uniaxial strength of the material was about $\sigma_c = 8.8 \text{ MPa}$ and the average volume weight was 18.8 kN/m^3 .

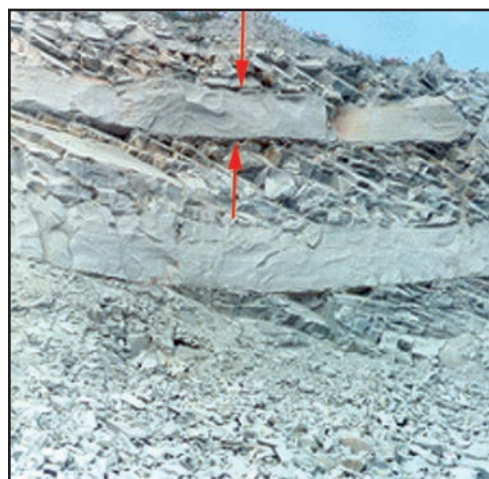


Figure 1. Layer of grey marl where specimens was taken.

With rocks, some material parameters, which describe the mechanical behaviour in general, and thus the creep itself, besides stress and temperature, depend on the moisture of the rock material, the moisture change and the humidity of the air in the surroundings, as well. In the experimental research carried out on the marl samples, the influence of these effects was minimized (by coating the sample with paraffin, the change of the humidity was slowed and limited, and direct contact with the air was prevented as well) in order to perform an unbiased research on the stress effects and the phenomena on deformations in the case of long-term load. During the creep test, relevant measurements on the specimens' moisture, their shrinkage, the temperature and the air humidity were conducted.

3 CREEP-TESTS APPARATUS

3.1 UNIAXIAL CREEP TESTS ON MARL

The uniaxial marl creep test in the experimental research presented here was performed on two groups with three prismatic specimens, 15x15x40 cm each. (This major group of specimen tests was preceded by the "zero" test serial of six specimens on which the creep test was carried out within a period of three months, which was used to verify the measurement techniques and to obtain preliminary values of the measured ones. Apart from this, 12 uniaxial tests were conducted under short loading on the specimens for the purpose of defining the

material parameters). A device with "dead" weight and a system of levers was used for loading and the "preservation" of the force over time, as presented in Fig. 2. Each of the six used devices was equipped with ring load cells (constructed by the author of this paper), which enabled variations of the force on the specimen during the test to be less than 0.3%.

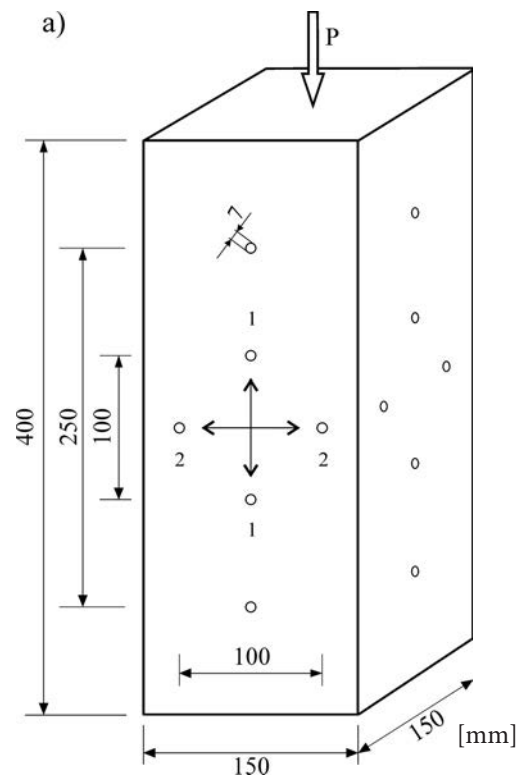


Figure 2. Device for uniaxial loading at creep test.



Figure 3. Prismatic sample: a) scheme of measurement points; b) samples during the creep test (coated with paraffin).

The test was performed in three phases, loading, unloading and reloading to a higher level of stress, while maintaining its constant value after the stress change. The total duration of the test was 360 days (I phase: 180 days, II phase: 30 days and III phase: 150 days). After loading, the creep deformations were measured in the direction of the vertical (longitudinal) and horizontal specimen axes (on four unloaded sides of the specimen), as shown in Fig. 3. a. The measurements were conducted with a mechanical deformation meter (type "Pfender", accuracy 1/1000 mm), 1, 3, 6, 12 and 24 hours after loading, then after 3, 7 and 15 days, and in the remaining period every 30 days. The measurement intervals were determined so as to have the differences between the previous and the current deformation nearly the same.

3.2 TEST ON PLATE SPECIMENS

The testing of the plate specimens was conducted with the devices shown in Fig. 4. The vertical loading in the device was imposed through the system of a lever and a dead load, while the horizontal force was applied through two inter-connected presses. The vertical force was applied through the press, which was set between the load cell and trapeze conveying element, while the horizontal force transfers to the horizontal press, set between the secondary frame and the trapeze element, following the law of connecting tanks. Different ratios of the vertical and horizontal pressures can be obtained by the application of presses whose pistons have differ-



Figure 4. Device for bi-axial loading – characteristic view.

ent cross-sections. By the application of this device the specimen can be "preserved" for months under the same vertical and horizontal pressures.

The plate specimens (Fig. 5 and 6) were loaded uniaxially and bi-axially, in their plane, in increments of 0.5 MPa in the period of an hour to a vertical stress of 2.0 MPa, which makes about 25% of the peak uniaxial strength of the examined marl. Three specimens were loaded uniaxially, and in the following three groups the ratio of the horizontal and vertical pressures was varied $P_h/P_v = 0.3, 0.5$ and 1.0. The initiated stress state (with the ratio $P_h/P_v = \text{const.}$) was preserved in the following 45 days with a measurement of the deformation fields on both sides of the plate. This phase of the test was projected in such a way as to establish the influence of the lateral pressure on the creeping in the vertical direction, and to establish the variation of the measured deformations (short and long), depending on the form of the specimens, i.e., prismatic or plate.

The measurement of creep deformations was performed on the network of measuring spots (shown in Fig. 6) 1, 6 and 24 hours after loading, then after 3 and 7 days and in the following period every 15 days. The measurement intervals were determined so as to have the differences between the previous and current measurement deformations nearly equal.

The network of measuring spots consists of inter-connected triangles with 92 sides in total. Since the measurements contain certain errors, it was necessary to make a correction of the measurements so that the

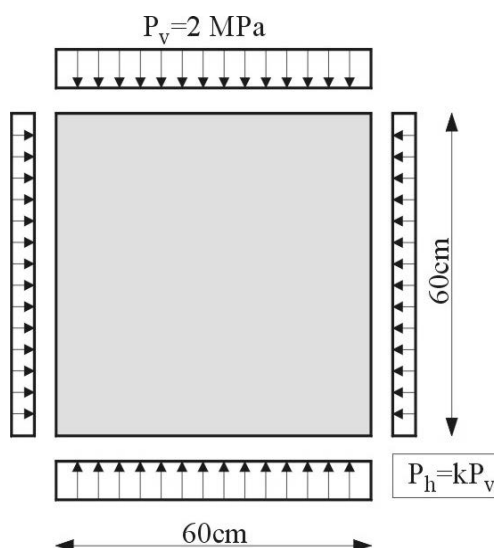


Figure 5. Plate specimen loading scheme.

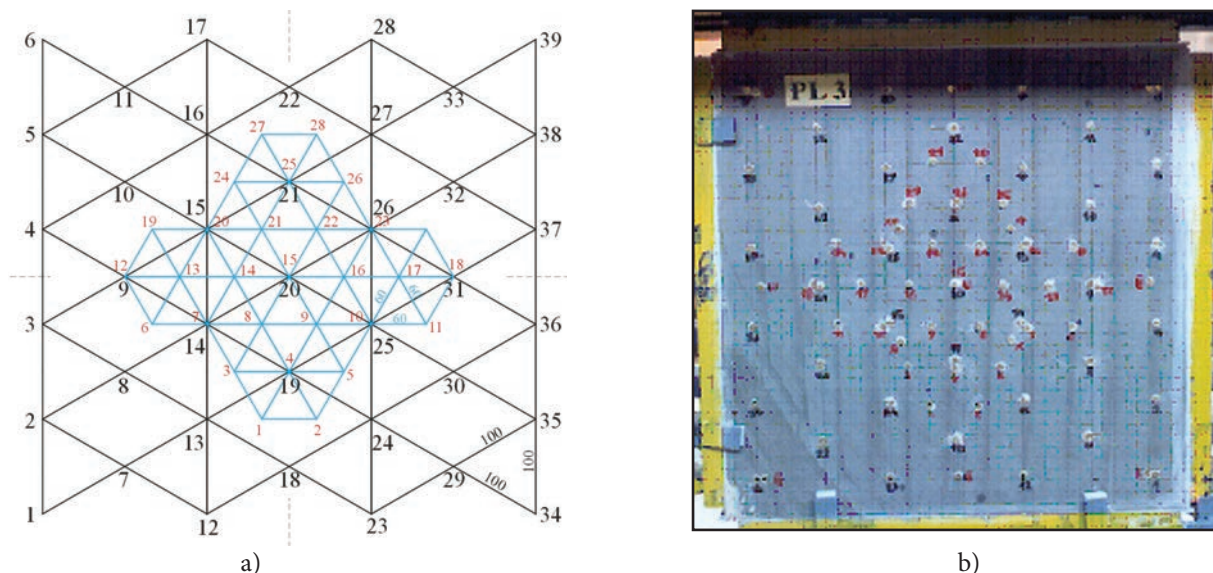


Figure 6. Plate specimen: a) scheme of measuring spots; b) specimen equipped with measuring bases.

lengths of the sides of all the measuring bases—sides of the triangles in the network give the same coordinates of the nodes. For the purpose of finding coordinates of the nodes of the network, the software “SIGMA” was used, which is intended for the “settlement” of the geodetic network based on the over-squares method. For the purpose of calculating the coordinates of the triangles’ apices of the referential network, 62 lengths of the sides correctly positioned on the network were sufficient, while the software used supernumerary measurements to improve the accuracy.

3.3 CONVENTIONAL TESTS OF TRIAXIAL COMPRESSION

The measurement of the specimens’ deformations by conventional three-axial tests in the standard Hook’s cell included the use of a strain gauge and rosettes for the measurement of deformation in the two normal directions (accuracy 10^{-5} mm, producer: TML-Japan). Glue P2 (TML-Japan), with a high deformation power, was used for the gluing of the rosettes, which enabled the measurement of the high strain expected in the examined material.

Each specimen was equipped with three rosettes or a strain gauge set in the middle of the specimen height under the central angle of 120° , seen through the cross-section of the specimen, as shown in Fig. 7. A stripe cable, about 0.3mm thick, was used to connect the strain gauge with the “data logger”. After the cable was set and

the rosettes were connected, a protective membrane was put over the specimens. A total of 24 specimens were prepared and examined in the three-axial device along with measurements of the deformations and about ten more specimens were led to failure without any measurement of the deformations (with a measurement of the axial stress of the failure and the lateral pressure).

Conventional tests of the triaxial compression give the possibility of analysing the influence of the lateral stress on the deformations. The lateral pressure $\sigma_2 = \sigma_3$ (which varies in the set of tests) does not usually exceed a value of 50% of the peak strength obtained in a uniaxial test with free lateral deformations. Generally speaking, this type of test can be conducted with controlled forces, with a load against the specimen or with a control of the velocity of the axial deformation. A creep test carried out on marl in a shorter period of time (seven days), represents a specific type of three-axial test with controlled force that is stress state, after which the application remains constant during the test.

A creep test on marl in a conventional triaxial device was carried out on 10 specimens with a constant vertical load of 2.0 MPa in the period of 3 days and with 4.0 MPa of load within the following 3 days. Three specimens were tested without lateral pressure, the fourth one had a lateral pressure of 1.0 MPa, and three specimens had a 2.0 MPa lateral pressure. This short creep test offered some qualitative indicators of behaviour of the examined rock over time with the influence of the rotation symmetrical lateral pressure.

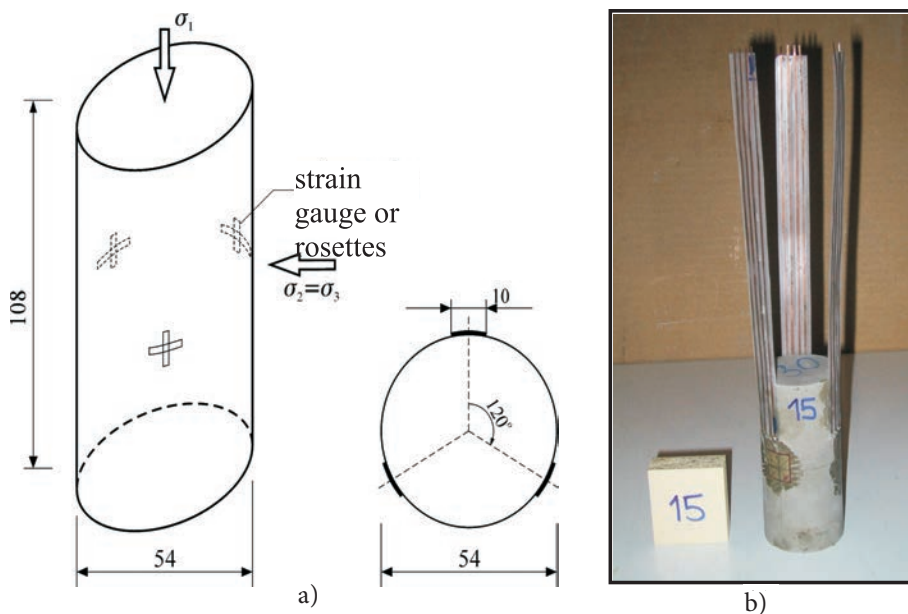


Figure 7. Cylindrical specimen for a conventional three-axial test; a) disposition of measurement rosettes; b) rosettes attached to the specimen.

4 RESULTS OF THE CREEP TESTS ON MARL

4.1 RESULTS OF THE UNIAXIAL CREEP TESTS ON MARL

The results of the measurement of creep deformations on prismatic specimens, at an axial stress from 2.0 MPa

to 4.0 MPa, are shown in Fig. 8. The diagram clearly shows the zone of intensive creep of materials in the axial direction in the first 20 days after the loading. The deformation increase in this period of time is non-linear in relation to the time. However, after this period the creep deformations increase linearly. It can also be noticed that the gradient of deformation increase during a period of time is bigger with specimens under higher pressure stress.

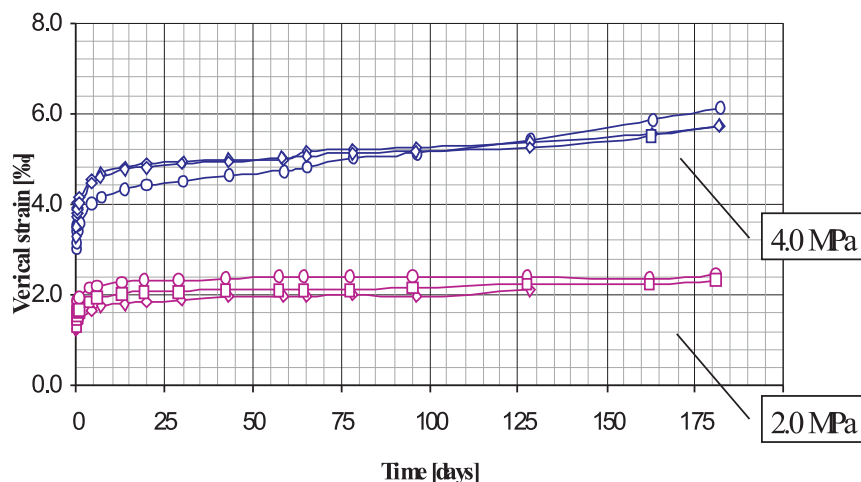


Figure 8. Comparative diagram of the creep in the axial direction under different stresses.

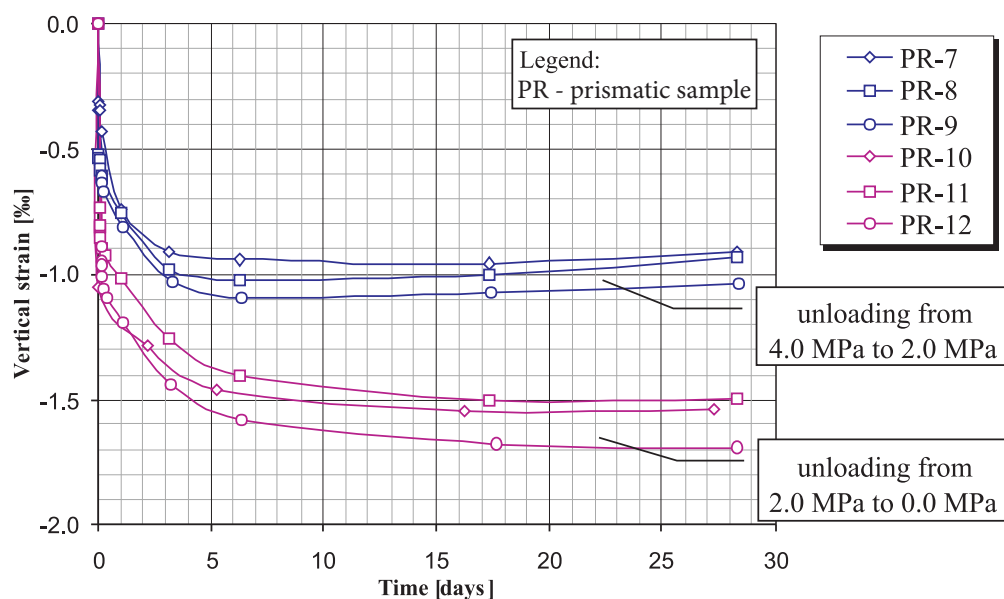


Figure 9. Comparative creep diagram after the total or partial unloading of prismatic samples in the axial direction.

Fig. 9 presents a comparative creep diagram after unloading in the axial direction in these two groups of prismatic samples. This diagram clearly shows that during the process of unloading, besides the instantaneous elastic deformation, there is also a significant time-dependent deformation - reverse creep (for details see [10]).

4.2 RESULTS OF THE CREEP TEST ON THE PLATE SPECIMENS

4.2.1 results of the creep test on the uniaxially loaded plate specimens

The material's low level of tensile strength made conducting the uniaxial test on the plate specimens difficult. Namely, small bumps on the specimens on the contact points with the steel trapeze elements that transfer the load resulted in a local concentration of the tension stress (like the "Brazilian" test by cleavage). Under a vertical load from 1.0 to 2.0 MPa, the tension stresses, induced in the horizontal direction, acquire the strength in materials, referring to tightening, the consequence of which is the appearance of vertical cracks.

At the contact point between the steel construction, i.e., conveying the trapeze elements for the steady loading of the plate specimens, a double Teflon foil was placed in order to eliminate any contact friction. This measure reduced the friction to minimum, which was verified by a measurement of the deformations on the plate specimens. Measuring the moisture of the plate specimens was

conducted directly after breaking the specimens by taking three pieces of marl. The average value of the moisture of the plate specimens was established to be 13.21%.

Due to the above-mentioned difficulties in performing the creep tests on uniaxially loaded plates, the test was performed on two plates with some cracks. The plate marked PL-1 is divided into two plates by a 60x30 cm crack, while the plate marked PL-4 was reduced by a vertical crack to a size of 60x50 cm.

After several unsuccessful attempts to load plate specimens uniaxially to a 2.0 MPa stress without cracks, the problem was, in the subsequent work, resolved by the replacement of two layers of Teflon foil by 5mm rubber beds placed on the contact points with steel trapeze conveying elements. The plate marked PL-7 (which was used in the first phase as a compensation for the shrinkage and temperature) was loaded through the rubber layers up to a stress of 2.0 MPa without the appearance of cracks. This plate was used for the analysis of short deformations of the plate specimens.

The results of the first phase of the creep test on the plate specimens are presented in the diagram in Fig. 10. Some bigger deformations, measured on plate marked PL-1, were probably the consequence of the smaller dimensions of the horizontal plate (60x30 cm), i.e., a smaller number of prevented side deformations. The approximate creep deformations of the prismatic specimens are shown as comparative values.

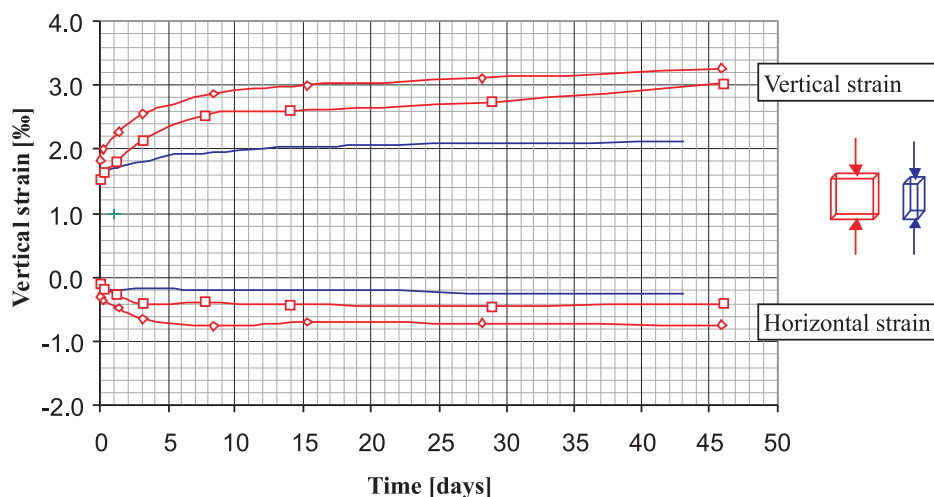


Figure 10. Diagram of the creep of uniaxially loaded plate specimens with 2.0 MPa stress.

The measured deformations on the plate specimens, with the same vertical stress, are bigger than the measured deformations on prismatic specimens. The ratio of the initial vertical deformations of the plate and prismatic specimens is 1.19. The same ratio was established between the deformations on the cylindrical and prismatic specimens. The ratio of the creep deformation of the plate and the prismatic specimens is bigger and amounts 1.85 (30 days after loading).

The diagram in Fig. 10 shows that an increase of the deformation of the creep significantly reduces in the horizontal direction after 10-15 days. This phenomenon can be explained by the behaviour of the materials in the vertical and horizontal directions, i.e., the exceptional anisotropy of the material ($E_h/E_v=2$, E-elasticity module), which is the consequence of the establishment of the microstructure of the marl during sedimentation. The creep of the vertically loaded samples in the horizontal direction is evidently predominantly occurring immediately after loading, i.e., in the zone of the primary creep component – delayed elasticity. When full, elastic deformations are developed, including the delayed deformations, the increase of the creep deformations is drastically reduced. A similar effect is noticed for the bi-axial load specimens – Fig.11.

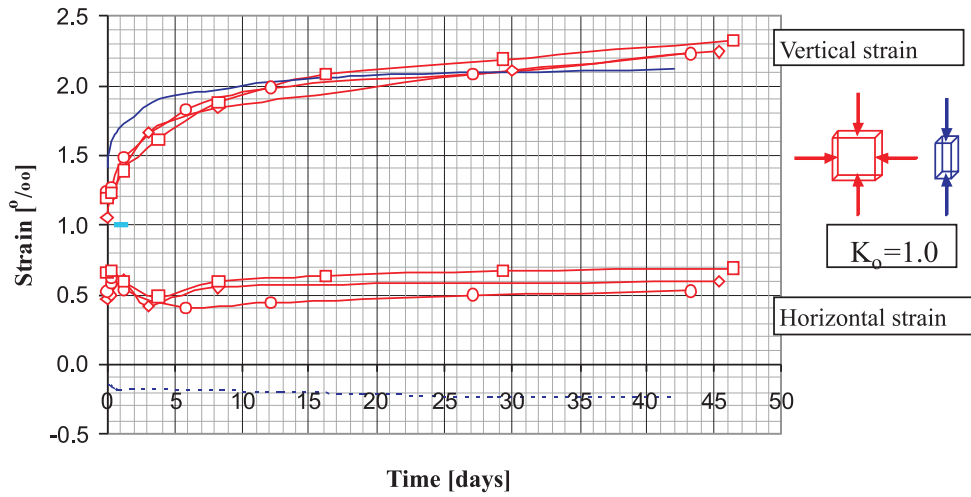
4.2.2 results of the creep test on the bi-axially loaded plate specimens

The lateral load of the bi-axially loaded plate specimens significantly changes the deformation picture, both the initial deformation induced by the stress change and the creep deformation. Fig. 11 shows the results of the

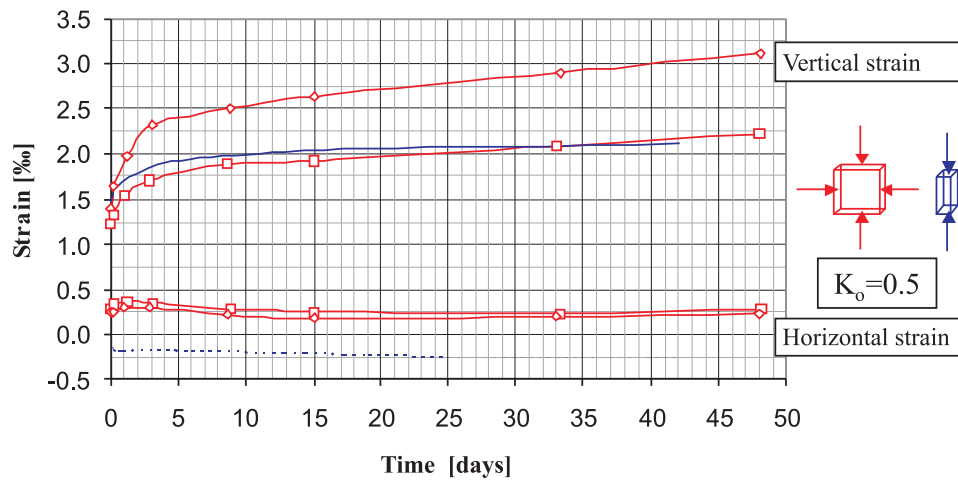
measurement of the deformation on the three groups of specimens loaded under different relations of horizontal and vertical stresses. All the diagrams show the average total deformation of the uniaxially loaded prismatic specimens with 2.0MPa vertical stress as a comparative value.

In the relation $K_o = \sigma_h/\sigma_v = 1.0$ with plate specimens, the initial and time vertical deformation differs very slightly from the deformation of the uniaxially loaded prismatic specimens, as shown in the diagram in Fig. 11.a. The increase in the time deformations was slightly bigger with the plate specimens compared to the prismatic specimens 10-15 days after loading. A larger increase of time deformations was accordingly the consequence of larger secondary creep with the plate specimens (secondary creep becomes more important as the time passes, while primary creep after a period of 10 days had practically no further influence on the deformation increase).

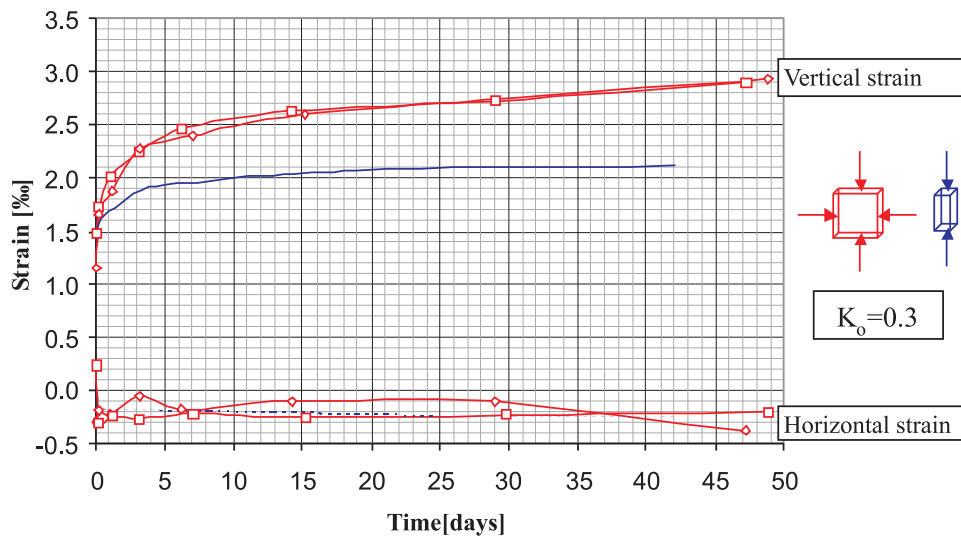
With a reduction of the relation $K_o = \sigma_h/\sigma_v$ from the value 1.0 towards the uniaxial stress state, an increase of the initial and time-dependent vertical deformations increases as shown in the diagrams in Fig. 11 a, b and c, which is the consequence of the release of the specimen's longitudinal extension. The horizontal deformation, with bi-axially loaded plate specimens, showed fluctuations in the first 5-7 days after loading. In the further period, creep in the horizontal direction could be registered only for specimens loaded with the same vertical and horizontal pressure. With all the other specimens with ratios $K_o = \sigma_h/\sigma_v = 0.5$ the horizontal deformations in time retained the value of the initial deformation and in ratio $K_o = \sigma_h/\sigma_v = 0.3$ the horizontal deformations were



a) with vertical stress 2.0MPa, where $K_0 = \sigma_h / \sigma_v = 1.0$;



b) with vertical stress 2.0MPa, where $K_0 = \sigma_h / \sigma_v = 0.5$;



c) with vertical stress 2.0MPa, where $K_0 = \sigma_h / \sigma_v = 0.3$;

Figure 11. Diagram of the creep of the bi-axially loaded plate specimens.

almost the same as the horizontal deformations of the prismatic specimens. In the ratios $K_o = \sigma_h/\sigma_v = 1.0$ and 0.5 the horizontal deformation is the shrinkage deformation and in the ratios $K_o = \sigma_h/\sigma_v = 0.3$ the horizontal deformation is the extension deformation.

4.3 RESULTS OF THE CREEP TESTS IN THE CONVENTIONAL TRIAXIAL DEVICE

The diagram in Fig. 12 shows simultaneously the results of the creep tests (strain-time) of the uniaxially loaded cylindrical specimens ($d/h=5.4 \times 10.8$ cm) and the average creep values on the prismatic specimens ($15 \times 15 \times 40$ cm)

under uniaxial stresses of 2.0 and 4.0 MPa. The test results indicate that there is no significant difference in the measured values of the time-dependent deformations on the prismatic and cylindrical specimens.

The diagram in Fig. 13 shows the creep-test results of the triaxially loaded cylindrical specimens with different lateral pressures. The full lines indicate the axial (vertical) strain and the dash lines indicate the tangential (horizontal) strain.

The radial deformation with all the specimens after one day of loading preserves the obtained level, regardless of the intensity of the radial stress in the considered domain, while the axial deformation indicates the pres-

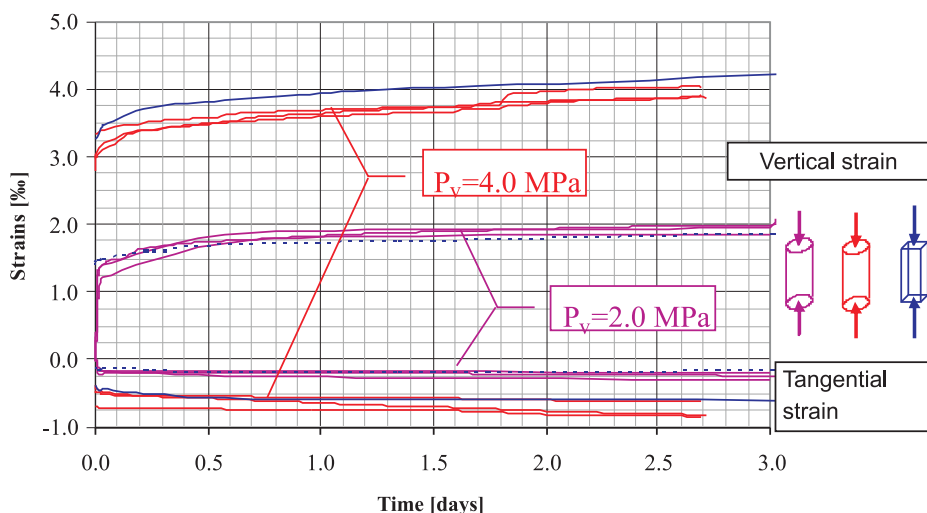


Figure 12. Comparative results of the uniaxial creep tests on the prismatic and cylindrical specimens with uniaxial stresses of 2.0 and 4.0. MPa.

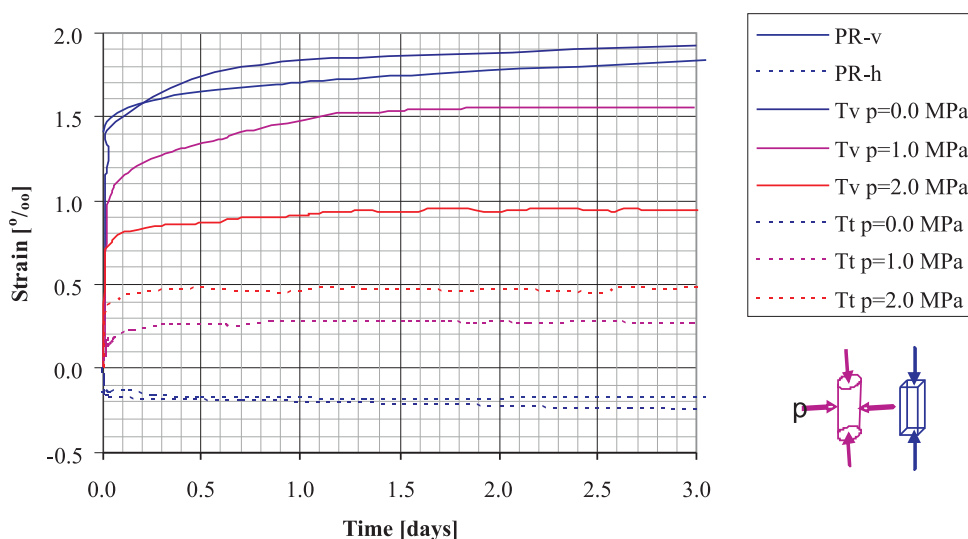


Figure 13. Results of the triaxial creep tests on the cylindrical specimens and of the uniaxial test on the prismatic specimens with an axial stress of 2.0 Mpa. (Legend: PR - prismatic sample; T_v/T_t - vertical/horizontal strain on the cylindrical sample; p - the lateral pressure).

ence of the influence of the lateral stress on the flow of the time deformations.

4.4 RHEOLOGICAL MODEL

Due to the common characteristics of rock features, which can be encompassed, and the formulation for the three-axial stress state, as a suitable basis for a description of the stress-deformation behaviour of different types of rock material, the constitutive Wallner Law was used /1983/ (developed on the basis of tests on rock salt). In a comparative analysis of the time-dependent deformation component of the marl after loading, it was determined that Wallner's rheological model, based on the results of the rock-salt testing, approximates well the creep of the marl after loading. In a comparative analysis of time deformations after total or partial unloading, it was found that the model does not include a reverse creep deformation, which is the consequence of the assumption that the primary creep depends on the current stress state.

As proposed by the author of this paper, and based on the results of uniaxial creep tests on marl specimens, a modified rheological model that describes the behaviour

of soft rock after loading and after total or partial unloading was formulated. In this model, the creep was primarily formulated as a function that is dependent on the stress difference that preceded the creep compared to the original model, where this component of creep depends on the current stress state. The above-mentioned correction enabled a correct description of the behaviour after total or partial unloading, which has significant implications in the event of modelling the state of stress around the tunnel opening. The mechanical model of the constitutive equations of the stress-deformation behaviour of the rock according to Wallner and the author of this paper is presented in Fig. 14.

For a practical application of the presented constitutive model a mathematical description of the rheological model of the rock mass is needed. The mathematical formulation of the rheological model of marl, when stresses are under the plasticity limit, is summarized in the following text (for details, readers can refer to the bibliography [3], [4] and [10]). The equations define the components of deformations and generally refer to three-dimensional cases. Having in mind the fact that deformations are time-dependent equations and are given as derivatives of time.

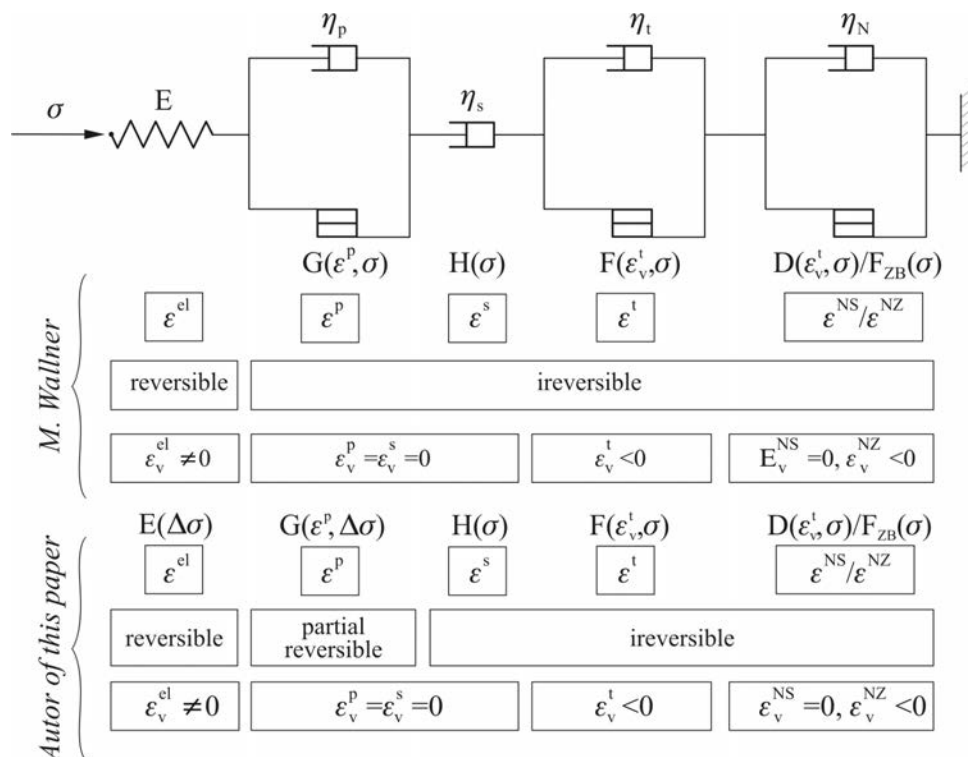


Figure 14. Mechanical model of the constitutive equations of the stress-deformational behaviour of the rock according to M. Wallner and the author of this paper.

According to Wallner's model, all the components of deformations are irreversible, except for the elastic component, while according to the corrected model, the component of secondary creep is reversible as well. Volumetric deformation appears in the elastic domain during tertiary creep and in failure due to the strengthening. The above-mentioned rule applies when there is no volumetric change in the primary and secondary creep.

The total deformation with stresses under the conditions of plasticity is obtained as a sum of three components:

$$\varepsilon = \varepsilon_e + \varepsilon_p + \varepsilon_s ; \quad (1)$$

where:

- ε_e - the elastic strain (induced by stress change),
- ε_p - the strain of primary creep (delayed elasticity),
- ε_s - the strain of secondary creep.

4.4.1 elastic component of deformations

The relation between the stress and the strain in the domain of elasticity in a common form is formulated as a differential equation:

$$\left\{ \frac{\partial \varepsilon^e}{\partial t} \right\} = [C] \left\{ \frac{\partial \sigma}{\partial t} \right\} ; \quad (2)$$

where:

- ε - the vector of the strain components,
- σ - the vector of component stresses,
- $[C]$ - the matrix of the coefficients of flexibility.

When the stress-strain relation is independent of the time, equation (2) is reduced to the following equation

$$\{\varepsilon\} = [D]^{-1} \{\sigma\} = [C] \{\sigma\} . \quad (3)$$

In the case of an arbitrary spatial stress state and strain, the equations of the generalized Hook's Law apply.

4.4.2 primary creeping

The common form of the relation between the stress and the strain in primary creep in a three-dimensional case according to the corrected model is described in the differential equation:

$$\frac{\partial \varepsilon^p}{\partial t} = \frac{1}{\eta_p} G \left\{ \frac{\partial (\Delta \sigma_{eff})}{\partial \{\sigma\}} \right\} ; \quad (4)$$

where:

$$G = E_p \left[\left(\frac{\Delta \sigma_{eff}}{E_p} \right)^m - \Delta \varepsilon_{eff}^p \right] ; \quad (4.1)$$

$$\Delta \sigma_{eff} = \sqrt{\frac{3}{2} (\Delta S_x^2 + \Delta S_y^2 + \Delta S_z^2 + 2\Delta \tau_{xy}^2 + 2\Delta \tau_{yx}^2 + 2\Delta \tau_{zx}^2)} ; \quad (4.2)$$

$$\Delta \varepsilon_{eff}^p = \sqrt{\frac{2}{3} (\Delta \varepsilon_x^2 + \Delta \varepsilon_y^2 + \Delta \varepsilon_z^2 + \frac{1}{2} \Delta \gamma_{xy}^2 + \frac{1}{2} \Delta \gamma_{yx}^2 + \frac{1}{2} \Delta \gamma_{zx}^2)} ; \quad (4.3)$$

- E_p - is the strain-hardening modulus
- η_p - is the viscosity (for primary creep)
- m - is the stress exponent (for primary creep)

The primary creep is described by three specific material parameters. E_p , η_p and m .

For the plastic potential σ_{eff} one invariant of the deviator part of the stress tensor was adopted ($\sigma_{eff} = \frac{3}{\sqrt{2}} \tau_{okt}$, where τ_{okt} is the octahedron of the shearing stress) and describes the departure from the hydrostatic stress state ($\sigma_1 = \sigma_2 = \sigma_3$), while ε_{eff}^p is an adequate invariant of the deviator part of the deformations tensor. The plastic potential σ_{eff} and ε_{eff}^p are defined by the components of the deviator part of the stress tensor $S_x, S_y, S_z, \sigma_{xy}, \sigma_{yz}, \sigma_{zx}$, i.e., the components of the deviator part of the deformations tensor $\varepsilon_x, \varepsilon_y, \varepsilon_z, \varepsilon_{xy}, \varepsilon_{yz}, \varepsilon_{zx}$.

The change of the plastic potential with the stress change from σ_i to σ_j is expressed as $\Delta \sigma_{eff}$, i.e., $\Delta \sigma = \sigma_j - \sigma_i$. An adequate invariant of the deviator part of the deformations tensor is ε_{eff}^p .

4.4.3 secondary creep

The common form of the relation between the stress and the strain of the secondary creep is described by the differential equation:

$$\left\{ \frac{\partial \varepsilon^s}{\partial t} \right\} = \frac{1}{\eta_s} H \left\{ \frac{\partial \sigma_{eff}}{\partial \{\sigma\}} \right\} ; \quad (5)$$

where:

$$H = P_o \left(\frac{\sigma_{eff}}{P_o} \right)^n ; \quad (5.1)$$

$$\eta_s = \frac{P_o}{a} ; P_o = 1.0 \text{ MPa} ; \quad (5.2)$$

- a - is the creep parameter
- n - is the normalized stress exponent (for secondary creep)

Secondary creep is described by two parameter constants of material a and n .

In a regression analysis based on the results of the creep tests on uniaxial specimens, the material parameters of the marl were defined, which describe the creep after total or partial unloading.

The components of the rheological model that appear as soon as the conditions of release are reached have not been the subject matter of this research, and they are not presented in detail (for details readers can refer to the papers of Wallner [11] and Doring and Kiehl [8]).

4.4.4 equation for uniaxial stress state

Considering that the conducted laboratory creep tests were carried out under a uniaxial stress state, a transfer to the creep equation for this specific stress case from general equations is of the most significant interest for the following analysis. After the inclusion of the uniaxial stress state and the appropriate processing, an equation describing the creep under a uniaxial stress state is obtained:

$$\varepsilon = \frac{1}{E} \Delta\sigma_1 + \frac{3}{2} \left(\frac{\Delta\sigma_1}{E_p} \right)^m \left(1 - e^{-\frac{2E_p}{3n_p} t} \right) + a (\Delta\sigma_1)^n t ; (6)$$

where the first element describes the elastic, the second element describes the primary creep and the third element describes the secondary creep. The material parameters of the marl were defined and they describe the components of the primary and secondary creep (Table 1) for the uniaxial stress state (for details, readers can refer to the papers of Tomanovic [10]).

Table 1. Values of the material parameters of the marl for primary and secondary creep after loading.

Parameters	Primary creep			Secondary creep	
	E_p [MPa]	μ_p [MPa.d]	m	a [1/d]	n
Marl	225	425	0.06	$2.71 \cdot 10^{-4}$	2.5
Rock salt	180	900	2	$3.40 \cdot 10^{-10}$	5

5 INFLUENCE OF K_0 ON VERTICAL DEFORMATION

5.1 INFLUENCE OF HORIZONTAL STRESS ON THE VERTICAL DEFORMATION WITH PLANE STRESS

A comparative diagram of the aggregate vertical deformation (stress dependent + creep deformation) of plate specimens shows that the applied lateral (horizontal) pressure reduces the vertical deformation. The diagram in Fig. 15 shows the values of the approximate measured vertical strain 45 days after the loading for different ratios of the horizontal and vertical stresses applied to the specimen.

The influence of the lateral pressure on the vertical deformation can be sufficiently well approximated with a linear function. The regression analysis with the application of the over-squares method resulted in an empirical dependence:

$$\varepsilon_1 = \varepsilon_1(\sigma_h = 0) - 0.88K_0 ; (7)$$

where:

- ε_1 - the vertical strain for $K_0 = 0$ to 1.0;
- $\varepsilon_1(\sigma_h = 0)$ - the vertical strain of the plate specimen when the lateral pressure equals zero;
- K_0 - the ratio of the horizontal and vertical stress
 $K_0 = \sigma_h / \sigma_v$.

According to the above-mentioned vertical strain with plane stress under the lateral pressure the influence can be reduced by up to 30% (where $K_0 = 1.0$) compared to the vertical strain developed without the influence of lateral pressure.

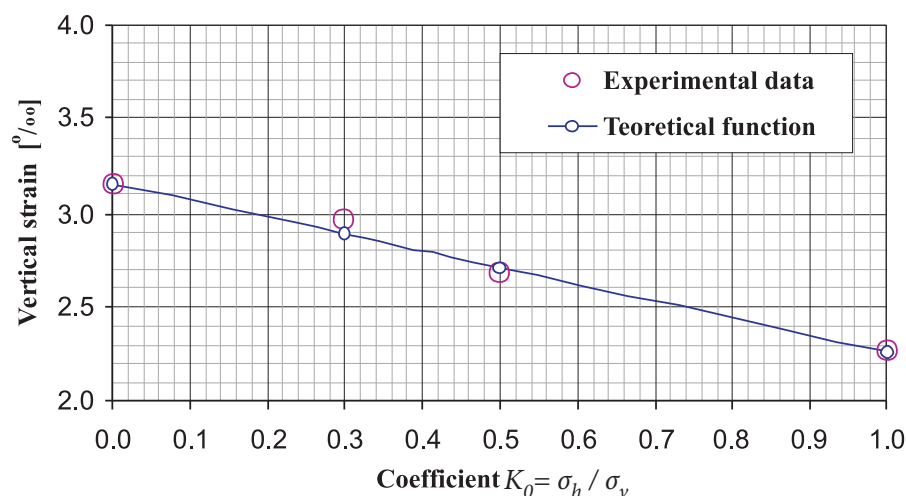


Figure 15. Total vertical strain of plate specimens 45 days after creep, depending on the ratios of the applied horizontal and vertical stresses.

5.2 INFLUENCE OF LATERAL STRESS $\sigma_2 = \sigma_3$ ON THE AXIAL DEFORMATION WITH A ROTATIONALLY SYMMETRICAL STRESS STATE

The comparative diagram of the total vertical-axial deformations (stress dependent + creep deformations) of the cylindrical specimens of marl with a conventional three-axial test shows that the applied lateral-radial pressure influences the reduction of the axial deformations. The diagram in Fig. 16 shows the values of the approximate measured deformation 3 days after the moment of loading for different ratios of the applied lateral and axial stresses on the specimen. The total deformation of the examined marl is two times smaller, with ratios $\sigma_h/\sigma_v = 1.0$, in relation to the uniaxially loaded specimens with $\sigma_h = 0$.

The influence of the lateral pressure on the vertical deformation can be well approximated in a linear function. The regression analysis with the application of the method of the over-squares method led to an empirical dependence, as follows:

$$\varepsilon_1 = \varepsilon_1(\sigma_h = 0) - 0.994K_0 ; \quad (8)$$

where:

- ε_1 - the vertical stain for $K_0 = 0$ to 1.0;
- $\varepsilon_1(\sigma_h = 0)$ - the vertical-axial strain of the cylindrical specimen where the lateral stress equals zero
- K_0 - the ratio of the horizontal (radial) and axial (vertical) stresses $K_0 = \sigma_h/\sigma_v$;

According to the previously illustrated, the total axial deformation (stress dependent + time dependant

component) in the conditions of rotationally symmetrical pressure can be smaller by up to 100% (where $K_0 = 1.0$) than the axial deformation developed without the impact of lateral pressure. With the plate specimens loaded in their plane at the plane stress state, the influence of the horizontal stress leads to a reduction of the vertical deformation up to a maximum of 30%, which indicates that borderline conditions have a large influence on the current deformations induced by the stress change and on the time-dependent deformations.

6 CONCLUSION

Creep tests conducted on uniaxial loaded prismatic specimens indicate that marl with a constant uniaxial pressure shows significant time deformations, i.e., creep, and thus the creep deformation that develops within 6 months almost reaches the value of the current deformation induced by the initial change of stress. In the first 20 days after loading, the increase in the deformation was non-linear in relation to the time. This is the zone of intensive creep of the material in the axial direction, i.e., primary creep. After this period the deformations of the creep are smaller and the increase in the deformations is almost linear, i.e., secondary creep. Additionally, the gradient of the deformation increase over time is larger with specimens loaded with a higher stress pressure.

The lateral (horizontal) pressure with bi-axially loaded plane specimens significantly changes the deformation picture of both initial deformations induced by the stress change and the creep deformations as a consequence of the different boundary conditions of different test methods. With ratios $K_0 = \sigma_h/\sigma_v = 1.0$ for the plate

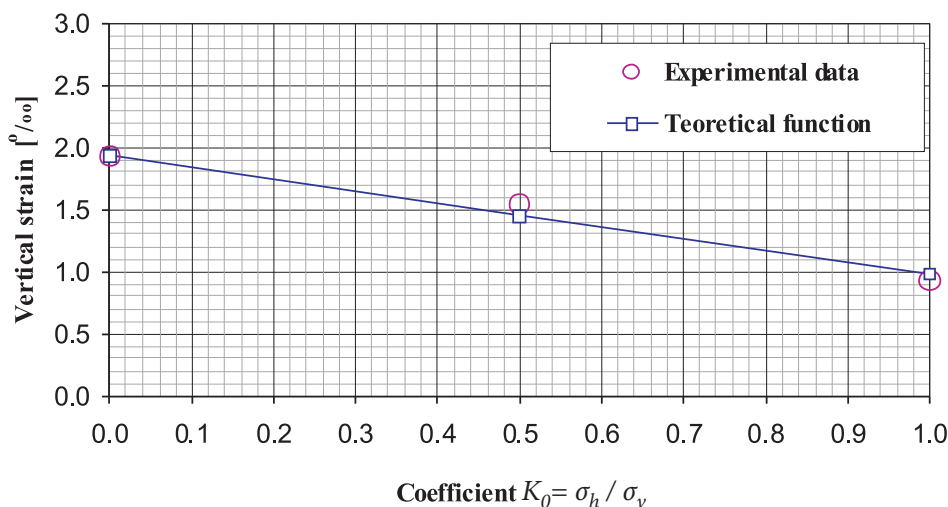


Figure 16. Total deformation of cylindrical specimens 3 days after creep, depending on the ratio of the applied horizontal and vertical stresses.

specimens, the initial and time-dependent vertical deformation very slightly differ from the deformation of the uniaxially loaded prismatic specimens. With a reduction of the ratios $K_0 = \sigma_h / \sigma_v$ from value 1.0 towards the uniaxial stress state, the increase in the initial and time-dependent vertical deformations grows, which is the consequence of the release of the lateral expanding of the specimen.

The comparative diagram of the overall vertical deformation (stress dependent + creep deformation) of the plate specimens shows that the applied lateral (horizontal) pressure reduces the vertical deformation and this influence can be sufficiently well approximated in an empirical function (7). The vertical deformation at the plane stress state due to the impact of the lateral pressure can be reduced by 30% (where $K_0 = 1.0$) in comparison to the vertical deformation, developed without the influence of lateral pressure, i.e., under a uniaxial stress state.

The effect of the influence of lateral pressure, the stress on the axial deformation during a conventional test of triaxial compression is significantly larger compared to the influence of the lateral pressure during a bi-axial load. The axial deformation in the conditions of rotationally symmetrical pressure can be reduced by as much as 100% (where $K_0 = 1.0$) compared to the axial deformation, developed without the impact of the lateral pressure. The influence of the lateral pressure can, with a rotationally symmetrical stress state, be sufficient to approximate an empirical function (8).

For practical applications with an acceptable approximation, the materials constants can be used as well as the parameters of the materials obtained in uniaxial tests, where the obtained values of all the deformations (short + creep deformations) should be corrected in line with the developed empirical formulas for plane and rotationally symmetrical stress states based on the dominant stress state of the matter considered.

REFERENCES

- [1] Bergues, J., Nguyen D., Hoetit, N. (1998). Time dependent behaviour of hard marls. *The Geotechnics of hard Soils-Soft Rock*, Evangelista & Picarelli, Balkema, Rotterdam.
- [2] Cristescu, N.D. (1988). *Rock Rheology*. Kluwer Academic Publishers.
- [3] Cristescu, N.D., Hunsche, U. (1998). *Time effects in Rock Mechanics*. John Willey & Sons.
- [4] Doring, T., Kiehl, J.R. (1993). Das primäre, sekundäre und tertiäre Kriechen von Steinsalz - Ein dreidimensionales rheonomes Stoffgesetz. *Geotechnick* 3, 194-199.
- [5] Ewy, R.T., Cook N.G.W. (1990). Deformation and Fracture Around Cylindrical Openings in Rock - I. *Int. J. rock Mech. Min. Sci.*, 27, 5, 387-407.
- [6] Keith, I.J.R., Reim, J. (1999). A three-dimensional constitutive law for rock salt including transient, steady state and accelerated creep, failure as well as post failure behaviour. *Proc. 9th ISRM Congress*, Vol. 2, Paris, 917-920.
- [7] Kemeny, J.M., Cook, N.G.W. (1991). Time-dependent borehole stability under mechanical and thermal stress: Application to underground nuclear waste storage. *Rock Mechanics as a Multidisciplinary Science*, Balkema, Rotterdam, pp. 997-986.
- [8] Kharchafi, M., Descoedres, F. (1995). Comportement differe des roshes marneuses encaissant les tunnels (Behaviour of tunnels in creeping marls). Ecole Polytechnique federale de Lausanne, Laboratoire de Mecanique des Roshes, Suisse.
- [9] Ladanyi, B., Gill D.E. (1996). Tunnel Lining in a Creeping Rock. *Canadian Tunnelling Canadian*.
- [10] Tomanovic, Z. (2006). Rheological model of soft rock based on test on marl. *Mechanics of Time-Dependent Materials*, 10, 2, 135-154.
- [11] Wallner, M. (1983). Stability calculation concerning a room and pillar design in rock salt. *International Congress for Geotechnics*, Melbourne.

RAZISKAVE SEIZMIČNEGA VPLIVA LOKALNIH TAL NA OBMOČJU BREŽIC Z METODO MIKRO-TREMORJEV

ANDREJ GOSAR

o avtorju

Andrej Gosar
Univerza v Ljubljani,
Naravoslovnotehniška fakulteta
in Agencija RS za okolje,
Urad za seizmologijo in geologijo
Dunajska 47, 1000 Ljubljana, Slovenija
E-pošta: andrej.gosar@gov.si

izvleček

Širše območje Brežic je eno potresno najbolj dejavnih v Sloveniji. Potres z $M_L=5.7$, ki je najbolj prizadel Brežice, se je zgodil 1917 in je dosegel največjo intenziteto VIII MSK. Seizmične vplive lokalnih tal zaradi kvartarnih sedimentov lahko pričakujemo na celotnem območju mesta. Ker je za oceno vpliva lokalnih tal na voljo zelo malo podatkov vrtin in geofizikalnih raziskav, smo izvedli študijo z metodo spektralnega razmerja vodoravnih in navpične komponente (HVSR) mikrotremorjev v 113 merskih točkah na prostem površju. Na splošnem smo dobili jasne spektralne vrhove, nekaj pa je bilo tudi območij s sploščeno krivuljo spektralnega razmerja, ki kaže na majhen kontrast v akustični impedanci med sedimenti in skalno podlago. Izrisana karta resonančne frekvence sedimentov kaže frekvenčni razpon 1-15 Hz. V južnem delu mesta odražajo višje frekvence tanko plast sedimentov (Brežiška terasa in srednja Savska terasa). Visoke amplitude HVSR vrhov kažejo na velik impedančni kontrast s sarmatijsko ali badenijsko podlago. Za severni del so značilne nizke frekvence, ki kažejo na debelo plast plio-kvartarnih sedimentov in majhen impedančni kontrast s pontijskim laporjem. Prehod med območjem višjih in nižjih frekvenc je razmeroma strm. Dodatno smo izvedli meritve v dvanajstih značilnih hišah za določitev vzdolžne in prečne frekvence stavbe. Ugotovljeno frekvenčno območje 5-10 Hz kaže na nekaj območij v južnem delu mesta, kjer obstoja potencialna nevarnost za resonanco med tlemi in objekti. Za dve stavbi smo neposredno ugotovili možnost takšne resonance. Glede na opravljene raziskave lahko pričakujemo bolj izrazite lokalne seizmične učinke v južnem delu Brežic.

ključne besede

vibracije tal, mikrotremorji, spektralno razmerje med vodoravnima in navpično komponento (HVSR), seizmični vpliv lokalnih tal, resonanca med tlemi in objektom

A MICROTREMOR HVSR STUDY OF THE SEISMIC SITE EFFECTS IN THE AREA OF THE TOWN OF BREŽICE (SE SLOVENIA)

ANDREJ GOSAR

About the author

Andrej Gosar
University of Ljubljana,
Faculty of Natural Sciences and Engineering
and Environmental Agency of Slovenia,
Seismology and Geology Office
Dunajska 47, 1000 Ljubljana, Slovenia
E-mail: andrej.gosar@gov.si

Abstract

The wider region of Brežice is one of the most seismically active areas of Slovenia. The most damaging earthquake occurred in 1917, when Brežice was hit by an $M_L=5.7$ earthquake that had an VIII MSK maximum intensity. Seismic site effects due to Quaternary sediments can be expected in the whole area of the town. Since there is a lack of boreholes and geophysical data to assess the site effects, the microtremor (ambient vibrations) horizontal-to-vertical spectral ratio (HVSR) method was applied at 113 free-field measuring points. In general, clear spectral peaks were obtained, but there were also examples of flat spectral ratios indicating a low impedance contrast between the sediments and the bedrock. A map of the sediment resonance frequency was drawn, which shows a frequency range of 1–15 Hz. In the southern part of the town higher frequencies correspond to the thin sediments (the Brežice terrace and the middle Sava terrace) and the high HVSR peak amplitudes indicate a great impedance contrast with the Sarmatian and Badenian bedrock. The northern part is characterized by very low frequencies, indicating thick sediments (Plio-Quaternary gravel) and a small impedance contrast with Pontian marl. The transition between the high and low frequencies is relatively steep. In addition, measurements were performed in 12 characteristic houses to assess the longitudinal and transverse building frequencies. The established building frequency range of 5–10 Hz indicates some areas in the southern part of the town where there is a potential danger of soil-structure resonance. Two buildings show direct evidence of a potential soil-structure resonance. According to this study, more pronounced seismic site effects are expected in the southern part of Brežice.

Keywords

ambient vibrations, microtremors, horizontal-to-vertical spectral ratio (HVSR), seismic site effects, soil-structure resonance

1 INTRODUCTION

The wider region of Brežice is one of the most seismically active areas of Slovenia (Fig. 1). The most damaging earthquake in the history of the town occurred on 29 January 1917, when Brežice was hit by an $M_L=5.7$ earthquake that had an VIII MSK maximum intensity (Lapajne, 1990). According to the seismic hazard map of Slovenia for a 475-year return period (Lapajne et al., 2001), a relatively high design ground acceleration value of 0.225 g for a rock site is ascribed to the Brežice area. Most of the town of Brežice is built on a mid-Pleistocene terrace composed of sandy gravel. Such relatively soft sediments can considerably enhance the seismic ground motion in the case of an earthquake and thus enhance the damage to buildings. Situations when soil-structure resonance occurs are particularly dangerous.

The only existing microzonation of Brežice (Vidrih et al., 1991) was based on surface geological data, since no subsurface geological or geophysical information was available. It was prepared for use together with the old seismic hazard map of Slovenia for a 500-year return period showing the intensity on the MSK scale (Ribarič, 1987), in which Brežice is estimated to have an VIII MSK. This microzonation showed that the maximum expected intensity due to the effects of soft sediments could be increased by $\frac{1}{2}$ – $\frac{3}{4}$ intensity grade. Today, the town of Brežice has around 5,000 inhabitants but, together with neighbouring villages, the population is more than 8,000. There are several important industrial and transport facilities in the area, which should be considered in any seismic risk-assessment study.

In order to study the site effects in more detail and in view of the fact that almost no subsurface geological

and geophysical information is available that would allow a modelling approach, we decided to perform a study based on a microtremor Horizontal-to-Vertical Spectral Ratio (HVSR) method (e.g., Bard, 1999). Microtremors were measured at 113 points and a map of the fundamental frequency of the sediments was prepared. In addition to this, microtremor measurements were performed inside 12 buildings to determine the buildings' fundamental frequencies and to identify possible soil-structure resonance.

2 SEISMOGEOLOGICAL CHARACTERISTICS

The town of Brežice is located in the Krško basin (southeastern Slovenia), which is situated in the transition zone between the tectonic units of the Dinarides and Pannonian basin. The wider area is characterised by a relatively high seismicity (Fig. 1).

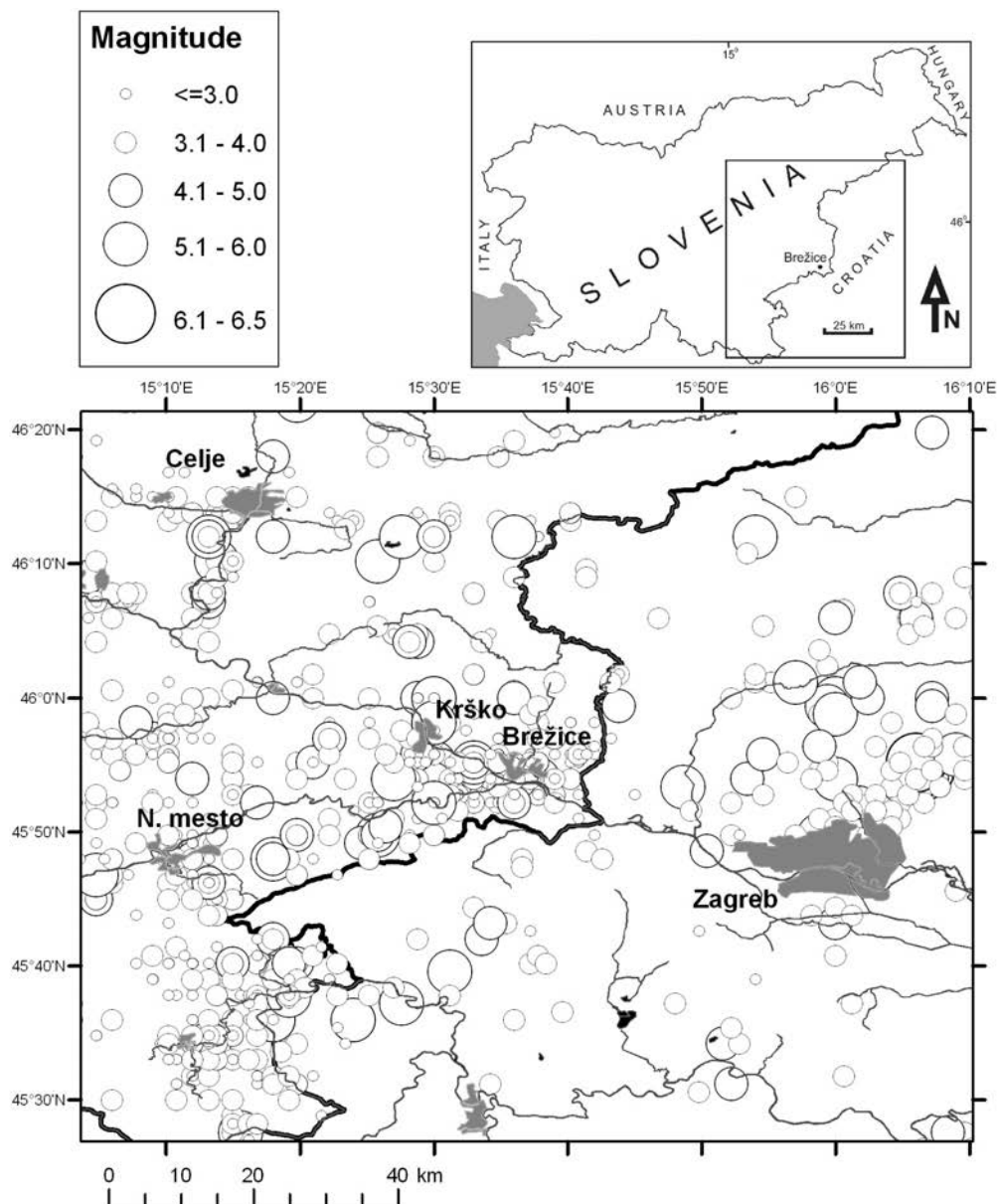


Figure 1. Seismicity of the wider Brežice area from the EARS (2008) catalogue.

Table 1. List of earthquakes with magnitudes equal to, or greater than, 5.0 that have epicentres within 60 km of Brežice (EARS, 2008).

Date	Lat °N	Lon °E	Depth (km)	Magnitude	Distance from Brežice (km)
/ /567	45.6	15.3		5.7	49
/ /1097	45.6	15.3		5.7	49
26/03/1502	45.9	16.0		5.2	45
17/06/1628	45.98	15.5	6.5	5.0	13
/ /1645	45.6	15.4		5.2	42
15/03/1697	45.62	15.46		5.2	36
11/02/1699	45.63	15.32	6.1	5.0	43
04/04/1877	46.17	15.23	3.6	5.1	36
09/01/1880	45.91	16.11		6.5	58
17/12/1905	45.9	16.1	7.0	5.6	56
02/01/1906	45.92	16.1	5.0	6.1	56
29/01/1917	45.9	15.57	13.2	5.7	4
03/12/1924	45.9	15.6	12.5	5.0	3

In the earthquake catalogue (EARS, 2008) there are 13 earthquakes with a magnitude of 5.0 or greater that have epicentres within 60 km of Brežice (Table 1). Presumably, the greatest damage to the town was caused by the Brežice earthquake on 29 January 1917, which had a $M_L=5.7$ and an VIII MSK maximum intensity (Lapajne, 1990). The last event with greater damage occurred on 3 December 1924. It had a $M_L=5.0$ and an VII MSK maximum intensity. After this event the seismicity over the past 85 years has remained high, but limited to small-to-moderate magnitudes.

A geological map of the study area is shown in Fig. 2. The Krško basin is filled with up to 2 km of Neogene to Quaternary sediments. It has a synclinal shape and is composed of two depressions: the Raka depression in the west and the Globoko depression in the east (Gosar & Božiček, 2006). The town of Brežice is located at the southern rim of the Globoko depression. Seismic reflection data indicate a dip of the seismic horizons within the Neogene sediments towards the north by 15–30° under the Brežice area (Persoglia, 2000). Most of the seismic horizons outcrop within the study area. The Badenian limestone outcrops south of the Sava river at Čatež. Sarmatian is represented by marl, sandstone and limestone. These layers outcrop at the foot of the Brežice terrace in the south and south-west. Pontian marl layers outcrop at the western and south-eastern rim of the terrace (Šikić et al., 1977). From the seismological point of view the Badenian and Sarmatian layers represent a hard bedrock, while the Pontian layers are

softer and have a lower impedance contrast with the sediment cover. The Neogene sediments are overlain by a succession of Sava river glaciofluvial sandy gravel deposits and fine-grained sediments from local sources (Verbič, 2004). The thickness of the Plio-Quaternary deposits is highly variable. In a borehole in Šentlenart, north of Brežice, they are 80 m thick, but only 200 m to the south-west they are completely eroded. Almost the whole town of Brežice lies on the mid-Pleistocene Brežice terrace composed of sandy gravel, which is partly cemented in a conglomerate. The thickness of the Brežice terrace is 5–10 m. It is overlain by very thin (0.2–1 m) alluvium composed of sandy-silt sediments. The Brežice terrace is uplifted with respect to the surrounding Holocene surface for around 25 m (Verbič, 2004). The area around the Brežice terrace is covered with the lower and middle Sava terraces and alluvium (Holocene).

According to the described general geological setting the thickness and physical properties of the soft sediments under the town of Brežice can vary considerably. Both influence the fundamental frequency of the sediments and the amplification of the seismic ground motion. Due to a lack of boreholes and geophysical data the extent of these variations is not known. Also the physical properties (the shear-waves velocity and density) of the "seismological" bedrock are, according to the known lithology, highly variable. This significantly influences the impedance contrast at the sediments-bedrock boundary.

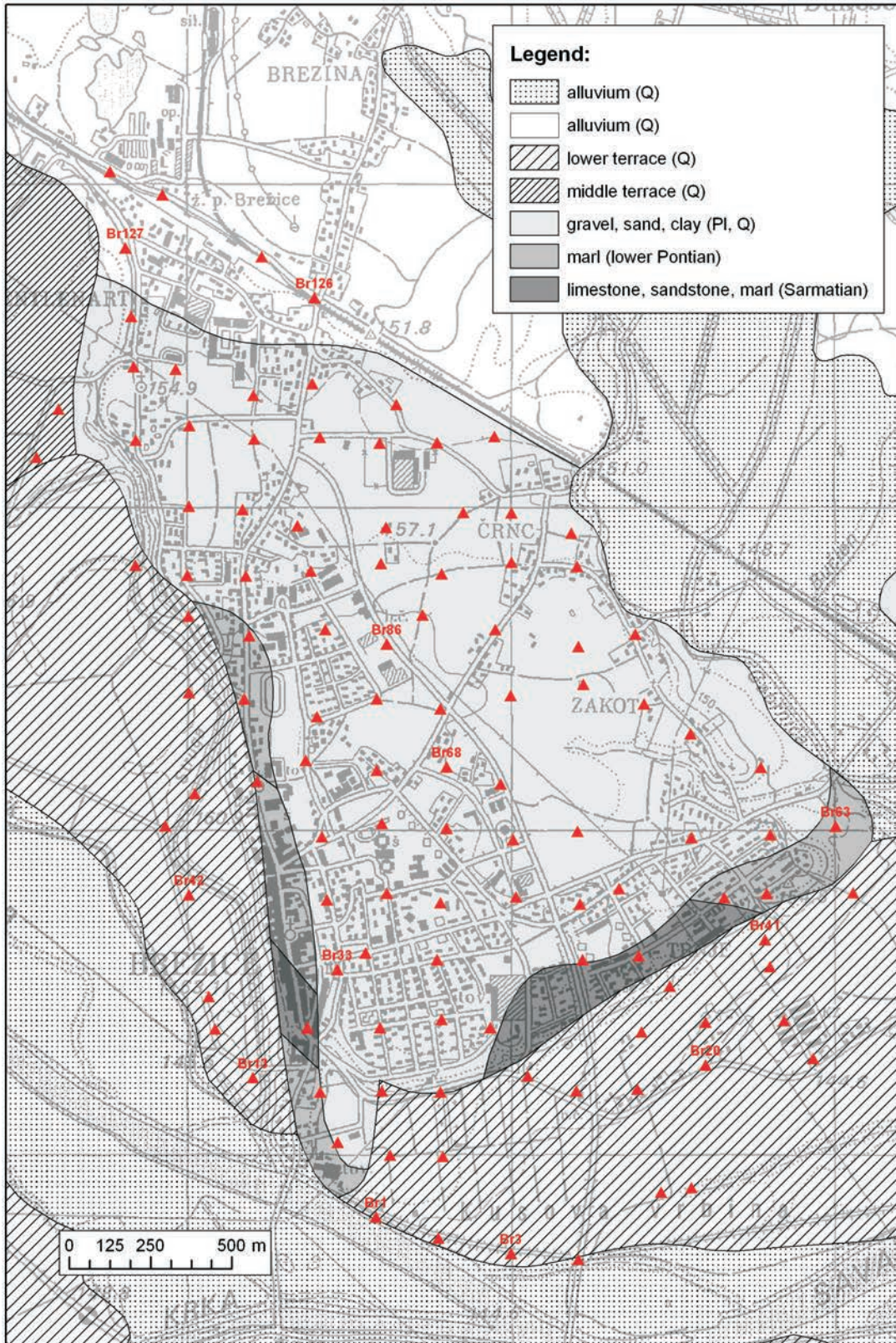


Figure 2. Geological map of the Brežice region, after Šikić et al. (1977). The transfer to GIS was made by the Geological Survey of Slovenia. The red triangles indicate the points of the microtremor measurements, while the labelled triangles are examples of the HVSR analyses shown in Fig. 3.

The existing microzonation of Brežice (Vidrih et al., 1991), which is based on surface geological data, ascribes two regions of different intensity increment due to soft sediments in the Brežice area. The whole Brežice terrace is classified as an VIII₂ intensity, which means a ½ intensity grade increment with respect to an VIII MSK intensity from the seismic hazard map. All the remaining area covered with the middle and lower Sava terraces and alluvium (Holocene) is classified as an VIII₃ intensity, which means a ¾ intensity grade increment.

3 METHODOLOGY

In the past ten years the microtremor HVSR method has been widely used for microzonation and site-effect studies. Reviews of the method can be found in Bard (1999). However, the theoretical basis of the HVSR method is still debated, and different explanations have been given. Nakamura's (2000) "body-waves" explanation is based on the S-wave resonance in soft sediment layers with a minor or negligible influence of the surface waves. More widely accepted (Bard, 1999; Bonnefoy-Claudet et al., 2006) is the "surface-waves" explanation, in which HVSR is related to the ellipticity of the Rayleigh waves, which is frequency dependent. HVSR therefore exhibits a sharp peak at the fundamental frequency of the sediments, when there is a high impedance contrast between the sediments and the underlying bedrock. Criticism of the HVSR method is often related to the fact that there is no common practice for data acquisition and processing (Mucciarelli & Gallipoli, 2001). Attempts to provide standards have been made only recently (SESAME, 2004). Today, it is widely accepted that the frequency of the HVSR peak reflects the fundamental frequency of the sediments. Its amplitude depends mainly on the impedance contrast with the bedrock and cannot be used as site amplification. In addition, HVSR does not provide any estimate of the actual bandwidth over which the ground motion is amplified. The main advantages of the HVSR method are a direct estimate of the resonance frequency of sediments without knowing the geological and S-velocity structure of the underground, and simple, low-cost measurements. Using the microtremor method, a much denser grid of measurements is possible than with any other method based on earthquake recordings, geophysical investigations or drilling. Any knowledge about the thickness and/or velocity of the sediments and the comparison of HVSR results with other methods and with the observed earthquake damage can significantly improve the reliability of the results (Bard, 1999).

The use of microtremors was later extended to an identification of the fundamental frequencies of buildings and soil-structure resonance (Mucciarelli et al., 2001; Gallipoli et al., 2004a). Damage enhancement and soil-structure resonance were recently studied using microtremors for the Umbria-Marche earthquake (Mucciarelli & Monachesi, 1998; Natale & Nunziata, 2004), the Thessaloniki earthquake (Panou et al., 2005) and the Molise earthquake (Gallipoli et al., 2004b). In Slovenia, examples of possible soil-structure resonance were found in the Bovec basin (Gosar, 2007), in Ilirska Bistrica (Gosar & Martinec, 2009) and in Ljubljana (Gosar et al., 2009).

4 MICROTREMOR MEASUREMENTS AND ANALYSES

In the Brežice area, measurements of the ambient vibrations were performed using portable Tromino seismographs (Micromed, 2005) composed of three orthogonal electrodynamic velocity sensors, a GPS receiver, a digitizer and a recording unit with a flash-memory card. All the parts are integrated in a common case to avoid electronic and mechanical noise, which can be introduced by wiring between the different parts of the equipment. In the frequency range 0.1–10 Hz, the self-noise of the seismograph is much lower than the standard seismic noise models of the Earth.

4.1 FREE-FIELD

An area of 4.7 km² was surveyed over an approximate 200 m x 200 m grid (Fig. 2). Altogether, 113 free-field measurements were performed. On average, there were 24 measuring points per square kilometre. GIS was used for planning the measurements and later for drawing the maps. The measuring locations were carefully selected to avoid, as far as possible, the influence of trees, buildings, underground structures and traffic. However, in the built-up urban environment this was not always possible. Good ground coupling on the soft soil was obtained by using long spikes mounted at the base of the seismograph. The sampling frequency was 128 Hz and the recording time was 20 minutes.

The HVSR analysis was performed in the following way. The recorded time series were visually inspected to identify any possible erroneous measurements and stronger transient noise. Each record was then split into 30-second-long non-overlapping windows, for which the amplitude spectra were computed using a triangular

window with 5% smoothing and corrected for the sensor-transfer function. The smoothing percentage determines the width of the mobile window centred at each frequency. The HVSR was computed as the average of both horizontal component spectra divided by the vertical spectrum for each window. From the colour-coded plot of the HVSR functions for all 40 windows, the windows including strong transient noise (the bypassing of a heavy truck or a train, for example), were identified in order to be excluded from further computation. Although the effect of transient seismic noise is still debated, this is a generally recommended procedure in HVSR analysis. Castellaro & Mulargia (2009), for example, have shown that a few windows with strong transient noise severely affect the average HVSR curve below 2 Hz. Also, in our experience, it is important to remove the stronger transient noise to improve the stability of the HVSR curve at low frequencies. On the other hand, Parolai and Galiana-Merino (2006) claimed that transients have little or no effect on the HVSR. Finally, the average HVSR function of all the windows, with a corresponding 95% confidence interval, was computed. In addition, a directional HVSR analysis was performed in 10° angular steps to identify possible directions of the noise sources.

4.2 MEASUREMENTS INSIDE BUILDINGS

Measurements were performed in 12 characteristic buildings to assess the main resonance frequencies. Two- and three-storey residential houses prevail in the area, together with some multi-dwelling buildings of up to five stories. Most houses are masonry with RC floors.

For measurements inside buildings, short spikes mounted at the bottom of the seismograph were used to enable precise levelling, but to avoid vibration of the unit. The recording time was 10 minutes. Two horizontal components were oriented in the longitudinal and transverse directions of the building. The measurements were usually performed on all the floors of the building. The instrument was placed as close as possible to the mass centre of the building (to avoid the influence of torsion) and close to a wall. Outside each building, but far enough so as to avoid its influence, a free-field measurement was also performed.

Each record was split into 10-second-long non-overlapping windows, for which the amplitude spectra were computed using a triangular window with 3% smoothing. Windows including strong transient noise were excluded from further computation, although some investigations indicate that the influence of the transients is negligible (Yuen et al., 2002). For both hori-

zontal components the average amplitude spectra were computed for each floor. As proposed by Gallipoli et al. (2004a), a separate HVSR for each horizontal component to the vertical component was also computed. A directional analysis was performed in 10° angular steps for easier recognition of the two main frequencies in the longitudinal and transverse directions.

5 RESULTS AND INTERPRETATION

5.1 FREE-FIELD RESULTS AND A MAP OF THE SEDIMENT RESONANCE FREQUENCY

HVSR analyses of 113 free-field measurements taken on an approximate 200 m x 200 m grid showed that most of them (76 %) fulfil the criteria defined by the European SESAME project for a reliable curve and a clear peak (SESAME, 2004). Three of these criteria for a reliable HVSR curve are based on the relation of the peak frequency to the window length, the number of significant cycles and the standard deviation of the peak amplitude. The next six criteria for a clear peak are based on the relation of the peak amplitude to the level of the HVSR curve elsewhere, and standard deviations of the peak frequency and of its amplitude (the amplitude should decrease rapidly on each side). If all three criteria for a reliable curve and at least five criteria for a clear peak are fulfilled, the frequency of the peak is considered to be the fundamental frequency of the sediments down to the first strong impedance contrast. The main reasons for the failure of the above criteria are: a) the high level of industrial or traffic noise or b) the amplitude of the peak or flat spectral ratio being too small. The latter does not mean a failure of the measurement, but that the impedance contrast between the sediments and the bedrock is too small. On the other hand, this means that only small site effects can be expected in areas with flat spectral ratios.

Twelve characteristic results of the HVSR analyses are shown in Fig. 3 in the direction from south to north. In the southern-most part (the middle Sava terrace – Kusova vrbina) the points Br1, Br3, Br20 and Br41 show very clear peaks in the frequency range 7.0–9.3 Hz, which have relatively high amplitudes (5–9). This indicates a relatively thin sedimentary cover and a strong impedance contrast with the bedrock. Points Br13 and Br42, which are also located on the middle Sava terrace (but west of Brežice), also show high frequencies (5.9–10.0 Hz), but the peak amplitudes are much

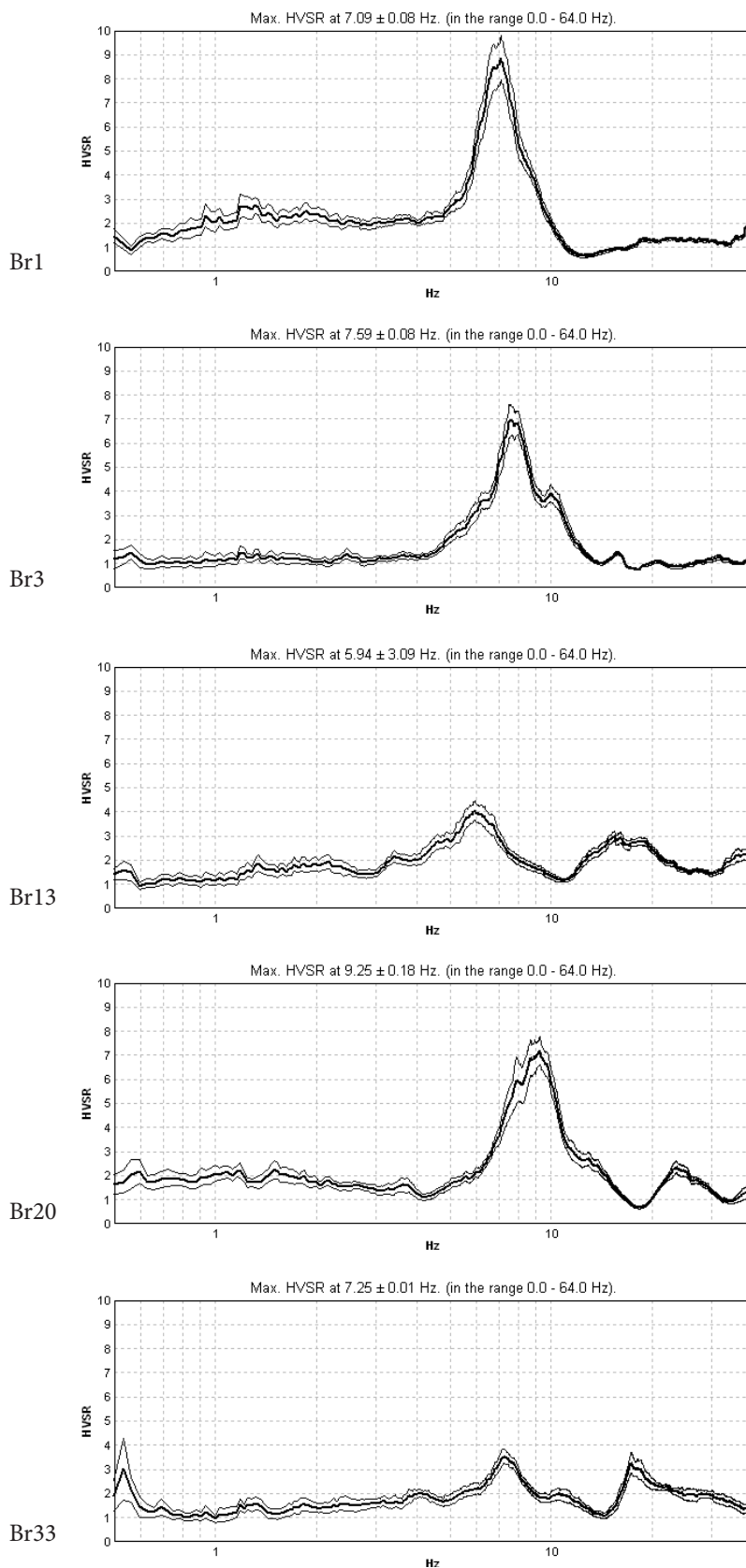


Figure 3 (part 1). Examples of microtremor HVSR curves. The locations of the measurements are shown in Fig. 2. The thin lines represent the 95% confidence interval.

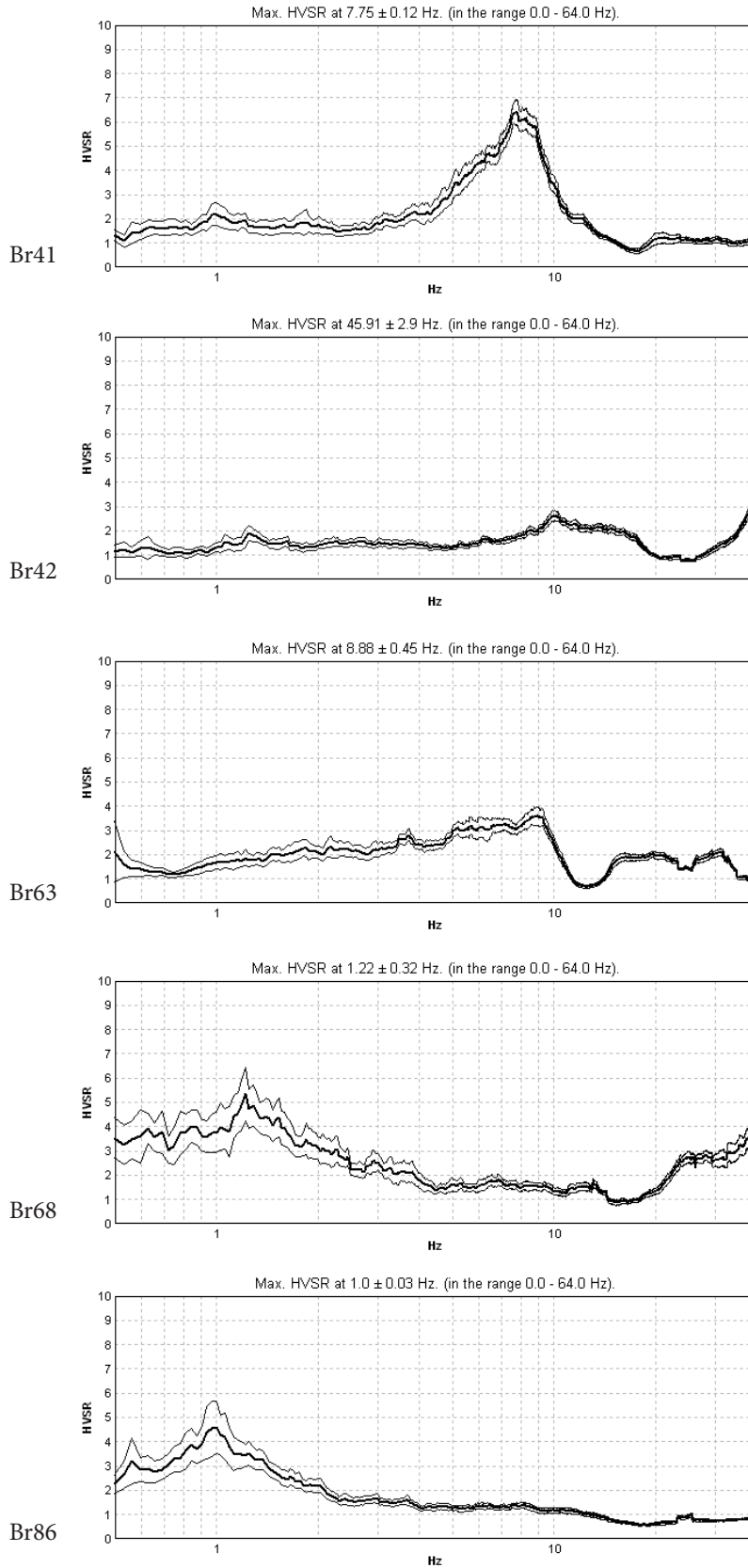


Figure 3 (part 2). Examples of microtremor HVSR curves. The locations of the measurements are shown in Fig. 2. The thin lines represent the 95% confidence interval.

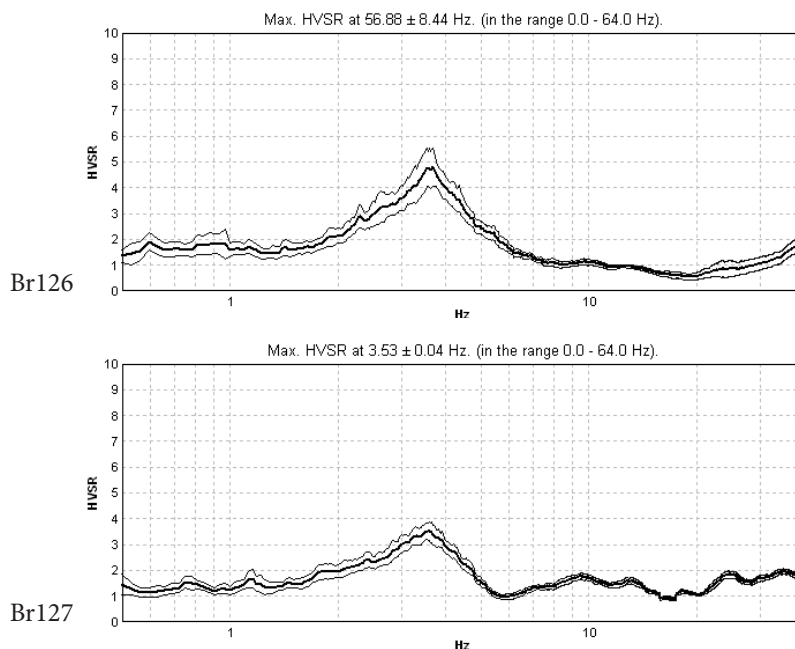


Figure 3 (part 3). Examples of microtremor HVSR curves. The locations of the measurements are shown in Fig. 2. The thin lines represent the 95% confidence interval.

smaller. This indicates that in this part the impedance contrast between the sediments and the bedrock is smaller. Point Br63, which is located on the outcrop of Pontian marl, is characterized by a not-well-expressed peak at 8.9 Hz. For the narrow belt of Sarmatian limestone, sandstone and marl in the central southern part of the town, very high frequencies (above 13 Hz) are characteristic, indicating only a thin weathered layer on top. In the southern part of the Brežice terrace (Br33) the peaks in the frequency range 6.5–14.6 Hz prevail. They reflect a thin layer of sediments (Brežice terrace is only 5–10 m thick) underlain by Sarmatian limestone, sandstone and marl. Towards the north there is a steep transition to very low frequencies, which are characteristic for the whole northern part of the Brežice terrace. Most measurements in the northern part of the terrace (Br68 and Br86) are very similar. They are characterized by a broad low-frequency peak (1.0–1.8 Hz) and a small amplitude. This is an indication of a thick layer of sediments and a small impedance contrast with the bedrock. This is in agreement with the known thickening of Plio-Quaternary gravel in the same direction from 0 m to 80 m (Verbič, 2004). Plio-Quaternary gravel is underlain by Pontian marl, indicating a small impedance contrast. A gradual increase of the impedance with depth inside the sedimentary layer due to compaction and the confining pressure is also probable. The lower signal-to-noise ratio in this area (Br68 and Br86) is reflected in a wider

95% confidence interval. The most northern part of the surveyed area (Šentlenart) lies on alluvium. The measurements in this area (Br126 and Br127) are characterized by slightly higher frequencies (2.5–3.8 Hz) and slightly better expressed peaks.

The frequencies of the HVSR peaks determined at 86 points were used to contour the iso-frequency map (Fig. 4), showing the resonance frequency of the sediments. The map shows the frequency distribution in a relatively large range of 1.0–15.1 Hz. For the southern-most part (Kusova vrbina), which lies on the middle Sava terrace, the frequency range 7.1–15.1 Hz is typical. This indicates a thin sedimentary cover, under which Badenian or Sarmatian limestone is expected. Also, the southern-most part of the Brežice terrace is characterized by high frequencies (6.5–14.1 Hz). These correspond to the known thickness of the Brežice terrace (5–10 m) and the Sarmatian limestone, sandstone and marl in the bedrock known from the outcrops at the foot of the terrace. Towards the north there is a steep transition to very low frequencies (1.0–1.8 Hz) that prevail in the whole northern part of the Brežice terrace, indicating the great thickness of unconsolidated sediments. There are two reasons for the lower frequencies and the lower amplitude of the HVSR peaks in this area. The first reason is the thickening of the Plio-Quaternary sand and gravel towards the north (from 0 to 80 m); the second reason is the change

of the bedrock lithology from Sarmatian lithified layers to Pontian marl. The latter results, together with a probable gradual increase of the shear-waves velocity and the density inside the sand and gravel, in only a small impedance contrast between the sediments and bedrock. There are only two measurements in the central part

of the terrace that show a higher resonance frequency (3.6 Hz). In the most northern part of the surveyed area (Šentlenart), which lies on alluvium, the sediment frequency is in the range 1.6–3.8 Hz. Higher frequencies (2.7–4.0 Hz) were also observed west of the Brežice terrace at points measured on the middle Sava terrace.

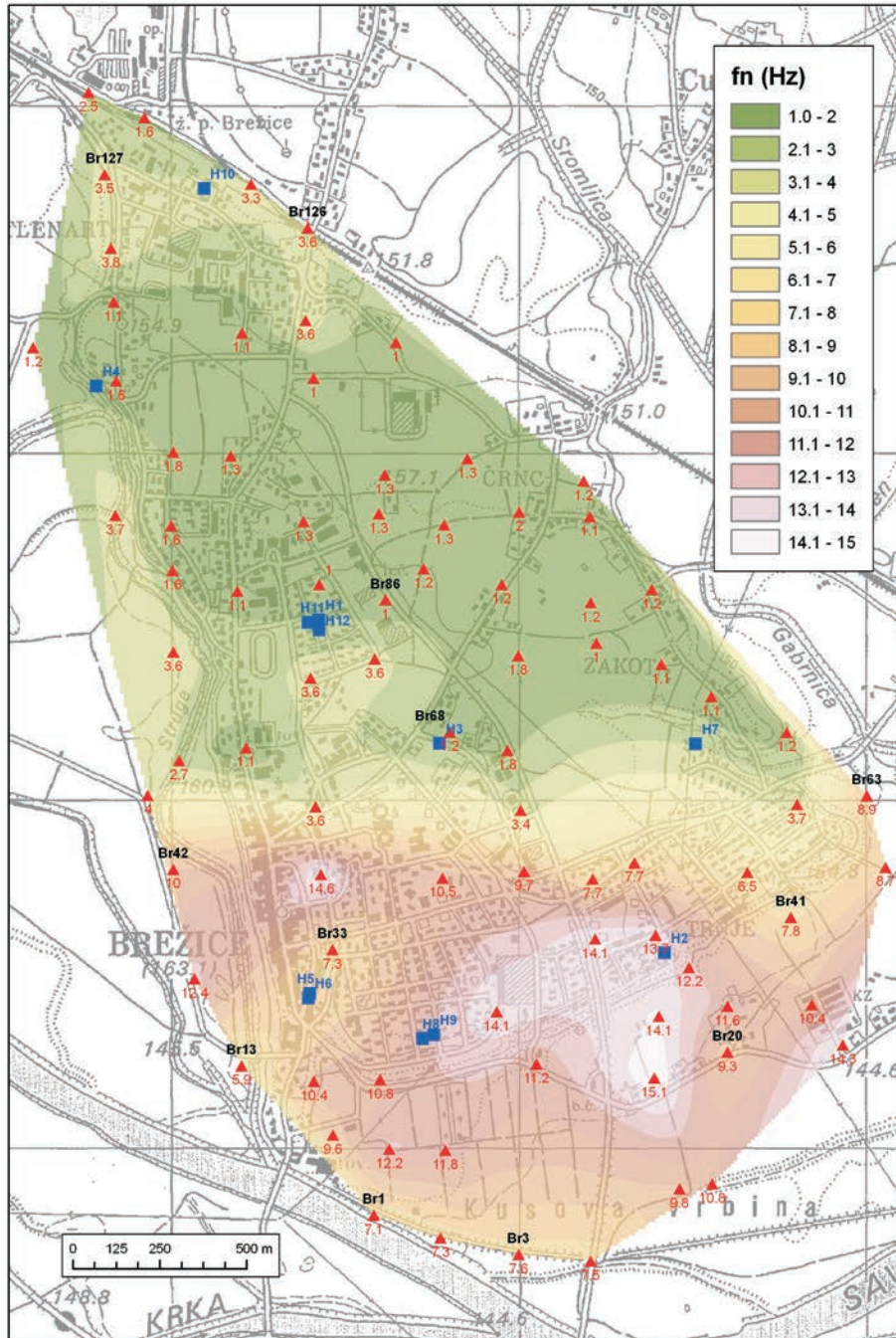


Figure 4. Map of the sediments' resonance frequency derived from free-field microtremor data. The red triangles indicate free-field measurements for which the resonance frequency can be determined; the red labels indicate the resonance frequency in Hz; and the blue squares indicate the locations of measurements taken inside buildings.

5.2 RESULTS OF THE MEASUREMENTS INSIDE BUILDINGS

The measurements performed inside the twelve buildings (their locations are shown in Fig. 4) confirmed that microtremors are an effective tool for identifying the main building frequencies. For ten of the measured buildings it was possible to identify the longitudinal and transverse frequencies from both amplitude spectra. A good correspondence in the frequency of the peaks from measurements taken at different floors in the same building was observed, showing an increasing amplitude response at higher levels. Since it is not the

purpose of this paper to discuss the dynamic behaviour of the buildings, but to identify possible soil-structure resonance, only the results from the highest floor of each building are presented below.

Two- and three-storey residential houses (masonry with RC floors) prevail in Brežice, but there are also some taller multi-dwelling buildings. The results of the measurements in 4 two-storey, 5 three-storey and 1 five-storey buildings are shown in Fig. 5. For each building two amplitude spectra are presented. The "N-S" component corresponds to the longitudinal and the "E-W" component to the transverse direction of the building.

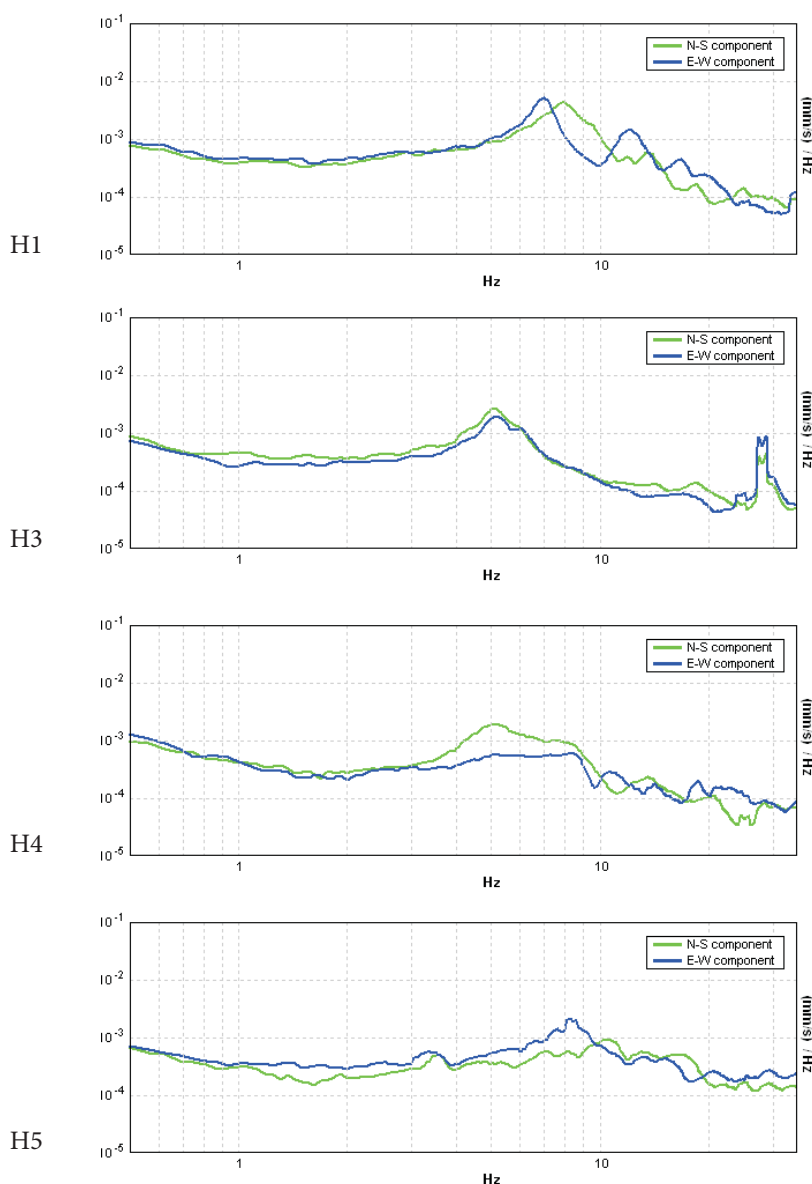


Figure 5 (part 1). Amplitude spectra of the measurements inside the buildings. Green is the longitudinal component; blue is the transverse component. The locations of the buildings are shown in Fig. 4.

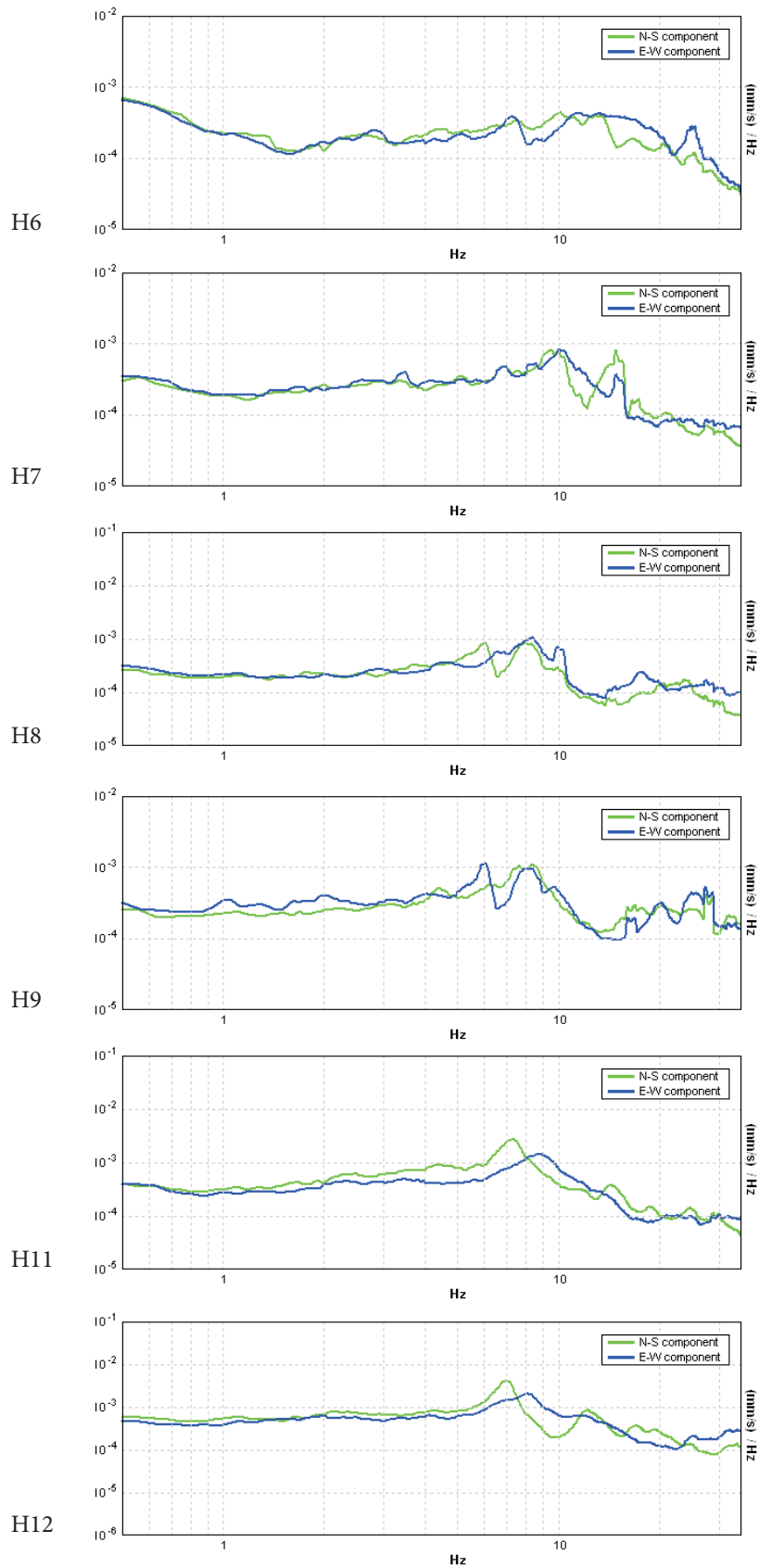


Figure 5 (part 2). Amplitude spectra of the measurements inside the buildings. Green is the longitudinal component; blue is the transverse component. The locations of the buildings are shown in Fig. 4.

The determined longitudinal and transverse building frequencies are shown in Fig. 6, and together with a free-field frequency derived from the iso-frequency map of sediments (Fig. 4), summarized in Table 2. The frequency difference between the longitudinal and transverse directions is, in general, small (<1.5 Hz). The two-storey buildings are characterized by the frequency

range 7.6–10.1 Hz, the three-storey buildings by the range 6.0–8.2 Hz and the five-storey by the range 5.1–5.2 Hz. There is a clear dependence of the frequency on the building's height. These values correspond well to the frequencies determined inside similar building types in the Bovec basin (Gosar, 2007), in Ilirska Bistrica (Gosar & Martinec, 2009) and in Ljubljana (Gosar et al., 2009).

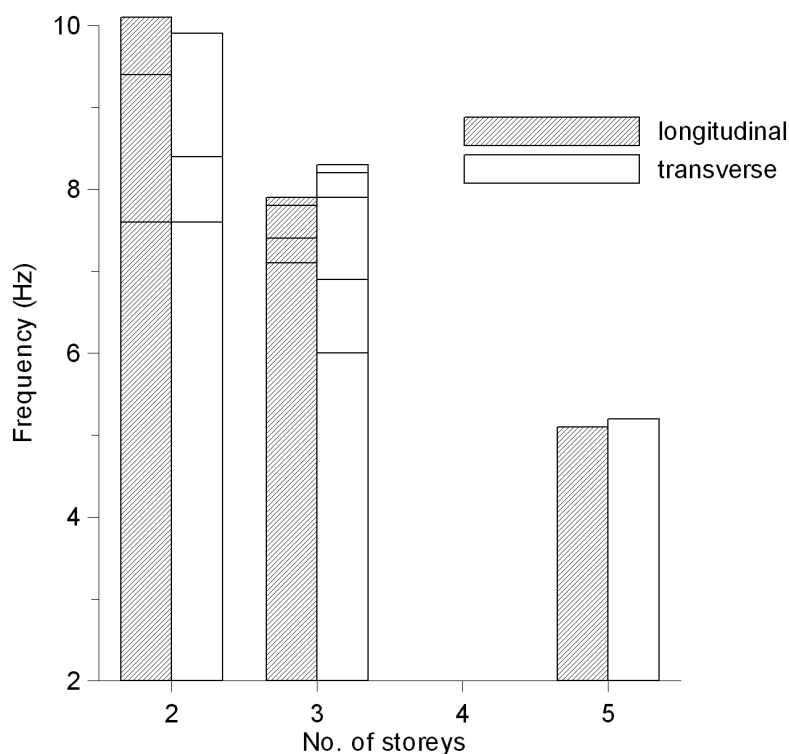


Figure 6. Plot of the building's main frequency vs. height (no. of storeys) for the ten examined buildings: 4 two-storey, 5 three-storey, and 1 five-storey.

Table 2. Main results of microtremor measurements inside buildings.

Building	Number of stories	Longitudinal freq. (Hz)	Transverse freq. (Hz)	Free-field freq. (Hz)
H1	3	7.9	6.9	2.1
H3	5	5.1	5.2	1.9
H4	2	7.6	8.4	1.7
H5	2	10.1	7.6	8.2
H6	2	10.1	7.6	8.3
H7	2	9.4	9.9	2.9
H8	3	7.8	8.3	11.7
H9	3	7.4	6.0	11.9
H11	3	7.4	8.2	2.0
H12	3	7.1	7.9	2.2

Two buildings, which are practically identical and located one beside the other in the old town centre, show direct evidence of soil-structure resonance danger. Their longitudinal and transversal frequencies are 10.1 Hz and 7.6 Hz, respectively, and the free-field frequency at their location is 8.2–8.3 Hz. Both buildings are located in the transition zone for which a steep change of sediment resonance frequency in the south-north direction is characteristic. Taking into account the whole range of the established buildings' main frequencies, which is roughly 5.0–10.0 Hz, and by comparing this range with the iso-frequency map of sediments (Fig. 4), we can see that the possible areas of soil-structure resonance are relatively narrow and limited to the transition zone in the central part of the Brežice terrace. Similar values are also observed in the southern-most part of the surveyed area (Kusova vrbina on the middle Sava terrace). At the moment there are almost no buildings in this area. Since microtremor measurements also indicate a high impedance contrast with the bedrock in this area (the high amplitudes of the HVSR peaks), site effect should be considered in any future spatial planning in this region.

6 CONCLUSIONS

Since the geotechnical characteristics of sediments and their thickness are poorly known in the Brežice area, due to lack of borehole or geophysical data, microtremor investigations have proved to be an effective tool for assessing the fundamental frequency of these sediments. A large area can be surveyed with a dense grid of free-field measurements, and a sample of buildings can be measured in a reasonable time and with relatively low costs in order to detect the potential danger of soil-structure resonance.

A map of the fundamental frequencies of the sediments shows a distribution in a wide range 1.0–15.1 Hz. There is a good correlation of different frequency ranges with a known lithology and thickness of the Quaternary sediments and lateral variations in the bedrock lithology. The high-frequency range is characteristic of the southern part of the town, where the sediments are thin (the Brežice terrace and the middle Sava terrace). The high amplitudes of the HVSR peaks indicate a great impedance contrast with the Sarmatian or Badenian bedrock. The northern part of the town is characterized by very low sediment frequencies, indicating thick Plio-Quaternary sediments. The low amplitude of the HVSR peaks indicates a low impedance contrast with Pontian marls in the bedrock or even a gradual increase of the shear-waves velocity and density with the depth within sediments due to compaction and the increasing confining pressure. The transition

between higher frequencies in the southern part and lower frequencies in the northern part is surprisingly steep.

The measurements inside buildings showed comparable longitudinal and transverse frequencies, as were obtained in similar building types in the Bovec basin (Gosar, 2007), Ilirska Bistrica (Gosar & Martinec, 2009) and Ljubljana (Gosar et al., 2009). There is a clear dependence of the main building frequencies on the building height. Since two- to five-storey buildings prevail in Brežice, the areas of potential danger for soil-structure resonance are limited to sediments in the frequency range 5–10 Hz. This frequency range was obtained in some areas of the southern part of the town. There are two direct observations of the potential soil-structure resonance among the surveyed buildings.

The only existing microzonation of Brežice (Vidrih et al., 1991) based on surface geological data does not distinguish significant variations in the sediment properties and thickness under the Brežice terrace revealed with this study, but classifies the whole Brežice terrace as the same VIII₂ MSK category. According to our study there is a big difference in the expected site effects between the southern and northern parts of the town. The sediments in the northern part are characterized by a low seismic amplification at low frequencies, and thus a small danger of soil-structure resonance. On the other hand, the strong influence of sediments on the seismic ground motion can be expected in the southern part of Brežice and on the middle Sava terrace (Kusova vrbina), which is not yet urbanised. In these areas the strong impedance contrast with the bedrock partly coincides with potential soil-structure resonance. Both can considerably enhance the damage in case of an earthquake.

To better understand the site effects in the Brežice area, additional geophysical measurements of the shear-waves velocity and the thickness of the sediments are recommended. In particular, the active and passive Multichannel Analysis of Surface Waves (MASW) method (Park et al., 2007) can provide valuable data on the shear-waves velocity at reasonable costs. On the other hand, knowledge of the soil-structure resonance can be enhanced with additional microtremor measurements inside buildings.

ACKNOWLEDGMENTS

The study was realized with the support of NATO SfP project 98057 "Assessment of seismic site amplification and seismic building vulnerability in FYR of Macedonia, Croatia and Slovenia" and research program P1-0011 financed by Slovenian Research Agency. The author is indebted to Jaka Žibrat and Pavel Osojnik for their help with the field measurements.

REFERENCES

- Bard, P.Y. (1999). Microtremor measurements: a tool for site effect estimation? In: Irikura, K., Kudo, K., Okada, H., Sasatami, T. (eds.) *The Effects of Surface Geology on Seismic Motion*. Balkema, Rotterdam, pp. 1251-1279.
- Bonnefoy-Claudet, S., Cornou, C., Bard, P.Y., Cotton, F., Moczo, P., Kristek, J., Fäh, D. (2006). H/V ratio: a tool for site effects evaluation. Results from 1-D noise simulations. *Geophys. J. Int.*, 167, 827-837.
- Castellaro, S., Mulargia, F. (2009). V_{S30} estimates using constrained H/V measurements. *Bull. Seism. Soc. Am.*, 99/2A, 761-773.
- EARS (2008). *Earthquake catalogue for the years 567-2008*. Environmental Agency of the Republic of Slovenia.
- Gallipoli, M.R., Mucciarelli, M., Castro, R.R., Mochavesi, G., Contri, P. (2004a). Structure, soil-structure response and effects of damage based on observations of horizontal-to-vertical spectral ratios of microtremors. *Soil. Dyn. Earth. Eng.*, 24, 487-495.
- Gallipoli, M.R., Mucciarelli, M., Eeri, M., Gallicchio, S., Tropeano, M., Lizza, C. (2004b). Horizontal to Vertical Spectral Ratio (HVSR) measurements in the area damaged by the 2002 Molise, Italy, earthquake. *Earthq. Spectr.*, 20/1, 81-93.
- Gosar, A., Božiček, B. (2006) Structural maps of seismic horizons in the Krško basin. *RMZ - Materials and Geoenvironment*, 53/3, 339-352.
- Gosar, A. (2007). Microtremor HVSR study for assessing site effects in the Bovec basin (NW Slovenia) related to 1998 Mw5.6 and 2004 Mw5.2 earthquakes. *Eng. geol.*, 91, 178-193.
- Gosar, A., Martinec, M. (2009). Microtremor HVSR study of site effects in the Ilirska Bistrica town area (S Slovenia). *J. Earth. Eng.*, 13, 50-67.
- Gosar, A., Rošer, J., Šket-Motnikar, B., Zupančič, P. (2009). Microtremor study of site effects and soil-structure resonance in the city of Ljubljana (central Slovenia). *Bull. Earthq. Eng.* (in press).
- Lapajne, J. (1990) Veliki potresi na Slovenskem IV, Brežiški potres leta 1917. *Ujma*, 4, 72-75.
- Lapajne, J., Šket-Motnikar, B., Zupančič, P. (2001). Design ground acceleration map of Slovenia. *Potresi v letu 1999*, 40-49.
- Micromed (2005). *Tromino user manual*. Micromed, Treviso.
- Mucciarelli, M., Monachesi, G. (1998). A quick survey of local amplifications and their correlation with damage observed during the Umbro-Marchesan (Italy) earthquake of September 26, 1997. *J. Earth. Eng.*, 2/2, 325-337.
- Mucciarelli, M., Gallipoli, M.R. (2001). A critical review of 10 years of microtremor HVSR technique. *Boll. Geof. Teor. Appl.*, 42, 255-266.
- Mucciarelli, M., Contri, P., Mochavesi, G., Calvano, G., Gallipoli, M.R. (2001) An Empirical Method to Assess the Seismic Vulnerability of Existing Buildings Using the HVSR Technique. *Pure. Appl. Geoph.*, 158, 2635-2647.
- Nakamura, Y. (2000). Clear identification of fundamental idea of Nakamura's technique and its applications. 12. Wprld Conference on Earthquake Engineering, Aucland.
- Natale, M., Nunziata, C. (2004). Spectral amplification effects at Sellano, Central Italy, for the 1997-98 Umbria seismic sequence. *Nat. Haz.*, 33, 365-378.
- Park, C B, Miller, R D., Ryden, N. Xia, J., Ivanov, J. (2007). Multichannel analysis of surface waves (MASW)-active and passive method. *The Leading Edge*, 26/2, 303-308.
- Panou, A.A., Theodulidis, N., Hatzidimitriou, P., Stylianidis, K., Papazachos, C.B. (2005). Ambient noise horizontal-to-vertical spectral ratio for assessing site effects estimation and correlation with seismic damage distribution in urban environment: the case of city of Thessaloniki (Northern Greece). *Soil. Dyn. Earth. Eng.*, 25/4, 261-274.
- Parolai, S., Galiana-Merino, J.J. (2006). Effects of transient seismic noise on estimates of H/V spectral ratios. *Bull. Seism. Soc. Am.*, 96/1, 228-236.
- Persoglia, S. (ed.) (2000). *Geophysical research in the surroundings of the Krško NPP*. Slovenian nuclear seismic administration, Ljubljana.
- Ribarič, V. (1987). *Seismological map of Slovenia for 500 years return period*. Seismological survey of Slovenia, Ljubljana.
- SESAME (2004). *Guidelines for the implementation of the H/V spectral ratio technique on ambient vibrations: measurements, processing and interpretation*. <http://sesame-fp5.obs.ujf-grenoble.fr/Delivrables/Del-D23 HV User Guidelines.pdf>.
- Šikić, K., Basch, O., Šimunić, A. (1977). *Osnovna geološka karta SFRJ 1:100.00, list Zagreb*. Geological Survey of Sloveia, Ljubljana.
- Yuen, K.V., Beck, J.L., Katafygiotis, L.S. (2002). Probabilistic approach for modal identification using non-stationary noisy response measurements only. *Earth. Eng. Struct. Dyn.*, 31/4, 1007-1023.
- Verbič, T. (2004) *Stratigrafija kvartarja in neotektonika vzhodnega dela Krške kotline 1. del: stratigrafija*. Razprave IV.raz SAZU, XLV-3, 171-225.
- Vidrih, R., Godec, M., Lapajne, J. (1991). *Potresna ogroženost Slovenije*. Seismological Survey of Slovenia, Ljubljana.

SAMODEJNA RAZPOZNAVA PRIHODA VALOV "S" PRI LOKALNIH POTRESIH

IZIDOR TASIČ IN FRANC RUNOVC

o avtorjih

Izidor Tasič
Agencija Republike Slovenije za okolje
Vojkova cesta 1b, 1000 Ljubljana, Slovenija
E-pošta: izidor.tasic@gov.si

vodilni avtor

Franc Runovc
Univerza v Ljubljani,
Naravoslovnotehniška fakulteta
Aškerčeva 12, 1000 Ljubljana, Slovenija
E-pošta: franc.runovc@ntf.uni-lj.si

izvleček

V primeru močnega lokalnega potresa pričakujemo občani, pristojne službe in sredstva javnega obveščanja hitro informacijo o njegovi lokaciji in veličinah. Poročila, kjer se ta podatek nahaja, so večinoma ustvarjena samodejno. Pri samodejnih postopkih je najpomembnejša naloga zaznava prihoda različnih tipov seizmičnega valovanja. Za zaznavo začetka valov P je znanih več različnih postopkov, ki se rutinsko uporabljajo po seizmoloških mrežah po svetu. V primerih, ko ima seizmološka mreža na razpolago malo število potresnih opazovalnic, pa je potreben tudi samodejen način zaznave začetka valov S. V članku je prikazan ravo postopka za samodejno zaznavo začetka prihoda valov S iz tri-komponentnega seizmičnega zapisa. Trije parametri seizmičnega signala so izračunani iz teh podatkov, začetek prihoda valov S pa je določen, ko zmnožek teh parametrov preseže referenčno vrednost. Tak, tako imenovani izbiralnik začetka valov S, uporablja Državna mreža potresnih opazovalnic Republike Slovenije za samodejno analizo podatkov o lokalnih potresih.

ključne besede

seizmični valovi, valovi P in S, analiza seizmograma, postopek za samodejno zaznavo valov S, izbiralnik začetka valov S, potresna opazovalnica, mreža potresnih opazovalnic

AUTOMATIC S-PHASE ARRIVAL IDENTIFICATION FOR LOCAL EARTHQUAKES

IZIDOR TASIČ and FRANČ RUNOVC

about the authors

Izidor Tasič
Environmental Agency of the Republic of Slovenia,
Vojkova cesta 1b, 1000 Ljubljana, Slovenia
E-mail: izidor.tasic@gov.si

corresponding author

Franč Runovc
University of Ljubljana,
Faculty of Natural Sciences and Engineering
Aškerčeva cesta 12, 1000 Ljubljana, Slovenia
E-mail: franc.runovc@ntf.uni-lj.si

abstract

In the case of a strong local earthquake, a quick report about the earthquake's location is expected. Such reports are usually performed automatically, where the identification of the seismic-phase arrival of the various seismic waves on the seismogram is the most important task. For this purpose, numerous detecting methods for the first P-wave arrival identification and determination are used. But in some cases, where the number of seismic stations in a local seismic network is very small, an automatic reading of the S-wave arrival is required. An algorithm for the automatic picking of the S wave arrival from three-component seismic data has been developed. Three parameters of the signal are calculated from these data and the S phase arrival is declared when the product of the three parameters increases above a reference level. Such a so-called S-phase picker is used to automatically analyze the data from local earthquakes in Slovenia's seismic network.

keywords

seismic waves, P and S waves, analysis of seismogram data, algorithm of the automatic picking of the S-wave arrival, S-phase picker, seismic station, seismic network

1 INTRODUCTION

The seismic-phase arrival identification of the various seismic waves on the seismogram is the most important task for a seismologist; it is the basic input data for additional geophysical and seismological studies, where earthquakes are the source of information. The complexities of different earthquake source mechanisms, the effects of propagation through inhomogeneous media, scattering, reflection and refraction on different boundaries of the earth's interior and the vast amount of seismic data mean that this task is very complicated and is performed by human experts who have to recognize the arrival of different types of seismic waves and their phases, which are frequently covered by seismic noise or the seismic waves themselves. In addition, the further the earthquake is from a seismic station, the more complex is the seismic record of such an earthquake.

For local earthquakes there are two important seismic wave identifications. A seismic station first detects the arrival of the P (primary) waves, which are compressional elastic waves; then it detects the arrival of the S (secondary) waves or transverse waves. The experts, who analyze the records of a local earthquake, usually denote just the entry of the first P seismic waves on the vertical record of the earth's movements, while the S seismic waves are marked on the horizontal record. The entry of the S seismic wave appears within the scattered P seismic waves; therefore, it is less conspicuous. To distinguish one from another, an expert must pay attention to the amplitude, the frequencies and the motion change, as well as to the position of the extreme of the amplitude. Consequently, it is not always easy to fix the entry of the phases in time. When both entries are well defined, the time difference between the entries is used to calculate the distances of the seismic station from the earthquake's hypocenter, and when this distance is known, the magnitude of the earthquake can also be estimated.

The very first and most basic purpose of a local seismic network is an accurate determination of the earthquakes' locations. This is also the goal of governments, which often finance the local seismic network. In the present era of a rapid exchange of information, many organizations, such as civil defense, expect a quick report about the earthquake's location. The civil defense uses this information to mitigate the social and economic consequences in the case of a strong earthquake. Such reports are usually performed automatically and depend on the quality of the local network of seismic stations, as well as on the information infrastructure, and on the algorithms, which perform the automatic phase-arrival identifications and consequently automatically estimate the basic parameters of an earthquake, such as its location and its magnitude. A modern seismic station consists of an acquisition unit, which digitizes the analogue signals from the seismometer and sends seismic data in real time to the supervision center, and a broadband seismometer, where three sensors detect the ground motion in the vertical and two horizontal directions (usually the east-west and north-south directions). When the seismic signal is received at the supervision center, a seismic-wave (or seismic-phase) arrival identification is automatically performed, and based on this information the basic parameters of the earthquake are calculated.

In recent years, numerous detection methods for the first P-wave arrival identification and determination have been developed and brought into use, from a very simple threshold algorithm to more sophisticated, adaptive methods, including neural networks and pattern matching [1],[2],[3],[4],[5],[6],[7],[8],[9],[10],[11]. Although these methods still cannot completely replace expert knowledge, they play a significant role in any automated location procedure, which provides the first information about an earthquake's parameters for an emergency centre. The number of seismic stations that provide earthquake-waveform data (or information about trigger times) and pass them to the center in real-time play an important role in the automatic procedure. For sufficient information, the number of seismic stations should be as high as possible. In some cases, however, the number of seismic stations in a local seismic network, which contribute their information to supervision center, can be very low. For this reason, an automatic reading of the secondary-waveform arrival is recommended. But the automatic S-wave arrival-identification methods are very few [12],[13],[14],[15], and they tend to be relatively complex. The reason why there are so many first P-wave arrival detectors compared to just a few first S-wave arrival detectors lies in fact that the seismic signal is, especially for a strong earthquake, significantly higher than the seismic noise, while the S seismic waves travel

with a lower velocity than the P seismic waves, and the first S-wave arrival can be hidden in the P seismic waves.

For this reason we have developed our own S phase detector for the local earthquake waveforms. The algorithm is fairly simple, efficient and also provides good information in spite of the higher seismic noise. Since the end of 2002 this algorithm has been working automatically in the Slovenian seismic network, and in the case of the strong earthquake in 2004, contributed to the rapid automatic location of this earthquake.

2 ALGORITHM AND METHOD

A three-component seismic station monitors the ground motions, usually the velocities along the east-west (E-W), north-south (N-S) and vertical (V) directions. With the help of an automatic first P-wave arrival detector the measuring system prepares a set of data containing a record of the local earthquake. Let us define the vectors for all three components as

$$\mathbf{Y}_e = (e_1, e_2, \dots, e_k) \quad (1)$$

$$\mathbf{Y}_n = (n_1, n_2, \dots, n_k) \quad (2)$$

$$\mathbf{Y}_v = (v_1, v_2, \dots, v_k) \quad (3)$$

The subscripts e , n and v indicate the east, north and vertical velocity components, respectively, and k is the number of samples. Let the first P seismic wave arrive at the sample i_p and the first S seismic wave arrive at the sample i_s , where $1 < i_p < i_s < i_k$. The following vector

$$\mathbf{O} = (o_1, o_2, \dots, o_k) \quad (4)$$

with the components

$$o_i = e_i^2 + n_i^2 + v_i^2 \quad \text{for } i = 1, \dots, k-l$$

can be used to estimate the relative total energy of an earthquake [16], [17]. This vector can also be expressed as the square of an envelope function, which is thought of as a positive outline of the seismogram [18]. In a similar way, we define the envelope function for earthquake records in horizontal planes, in a non-rotated data system, as the following vectors

$$\mathbf{E} = (|e_1|, |e_2|, \dots, |e_k|) \quad (5)$$

$$\mathbf{N} = (|n_1|, |n_2|, \dots, |n_k|) \quad (6)$$

The S-wave picker algorithm was developed on the basis of an energy analysis, where the idea of minimalism is followed: “the less the filtering, the better the algorithm” [19]. The energy analysis was based on the ratio of the short-term average (STA) energy to the long-term average (LTA) energy level, derived from the same seismogram [17]. These types of algorithms are referred to as STA/LTA detectors. Today, the ‘short-time-average through long-time-average trigger’ (STA/LTA) is the most broadly used algorithm for a P phase picker because of its simplicity and efficiency. Several different algorithms have been developed, but the most popular is the procedure where the average values of the absolute amplitude of a seismic signal are continuously calculated in two consecutive moving-time windows [24]. The short-time average is sensitive to seismic events, while the long-time average provides information about the temporal amplitude of the seismic noise at the measurement site. When the ratio of both exceeds a pre-set value, an event is ‘declared’ and data starts being recorded in a computer data file. Because the first S-wave arrival is hidden in the P seismic waves, this algorithm is not useful for S-wave detectors. For this reason, we define a transformation $f(x)$ for the vector x , where $f(x_i)$ is given by

$$f(x_i) = \frac{\frac{1}{l} \sum_{j=i}^{i+l-1} |x_j|}{\frac{1}{k-i+1} \sum_{j=i}^{k-1} |x_j|} \quad \text{for } i = 1, \dots, k-l \quad (7)$$

and l is the number of samples in an STA window. While the nominator still follows the idea of STA and is ‘sensitive’ to local changes in the amplitudes, the denominator provides information about the amplitude variation from the sample i to the end of the signal. Because, generally, the amplitudes of the S seismic waves for a local earthquake are about five times larger than those of P seismic waves, and also S seismic waves are much more strongly attenuated than P seismic waves [24], the value of the denominator is expected to be higher in the cases where i is before the first S-wave arrival, $i < i_s$. Using equation (7), the transformation of the total energy presented by (4) reduces to

$$\mathbf{f}_O = (f(o_1), f(o_2), \dots, f(o_{k-l})) \quad (8)$$

Similarly, the transformations of the envelopes of the horizontal components, presented with (5) and (6), are then given by

$$\mathbf{f}_E = (f(e_1), f(e_2), \dots, f(e_{k-l})) \quad (9)$$

$$\mathbf{f}_N = (f(n_1), f(n_2), \dots, f(n_{k-l})) \quad (10)$$

The relative position of the seismic station with reference to the source mechanism of an earthquake means that it is not possible to predict on which horizontal component the S-wave’s arrival will be more accurately detected. Because of this uncertainty, we create the following, so-called characteristic, vector [12]

$$\mathbf{C} = (c_1, c_2, \dots, c_k) \quad (11)$$

with the components

$$c_i = f(e_i)f(n_i)f(o_i) \quad \text{for } i = 1, \dots, k-l \quad (12)$$

The S-wave arrival is declared when the characteristic function increases above the threshold. It is chosen at a sample c_s , where the threshold is for the first time lower than the values in the characteristic function

$$c_s \ni (c_1, \dots, c_{i-1} \leq \text{threshold}) \wedge (c_i > \text{threshold}) \\ \text{for } i = 1, \dots, k-l \quad (13)$$

To simplify the search procedure, the S-wave arrival can be searched in the interval between the previous automatically defined P-wave arrival and the maximum value of the characteristic function. It is unlikely that the first S-wave arrival will fall outside this time window. For each record the value of the threshold is defined with regard to the characteristic vector. For example, in his picking procedure Cichowicz [12] uses the average value and the variation of its characteristic function. We simplify the procedure. The threshold is related to the maximum value of our characteristic function:

$$\text{threshold} = \text{constant}(\max(C)); 0 < \text{constant} < 1 \quad (14)$$

The constant is defined from the set of earthquake records with known P and S wave arrival times.

2.1 CALCULATION OF THE WINDOW WIDTH L AND THE THRESHOLD CONSTANT

Two unknown parameters have to be evaluated, the length of the STA window l and the values of the constant in the threshold definition. The STA window’s length and the constant are parameters that can be chosen arbitrarily after gaining some experience from the real data. These parameters were prepared from the set of 109 earthquake records from the years 1997 and 1998, with the local magnitudes ranging from 1.3 to 5.6, and with the epicenter distances ranging from 16 km to 160 km. The distribution of the epicenter distances with

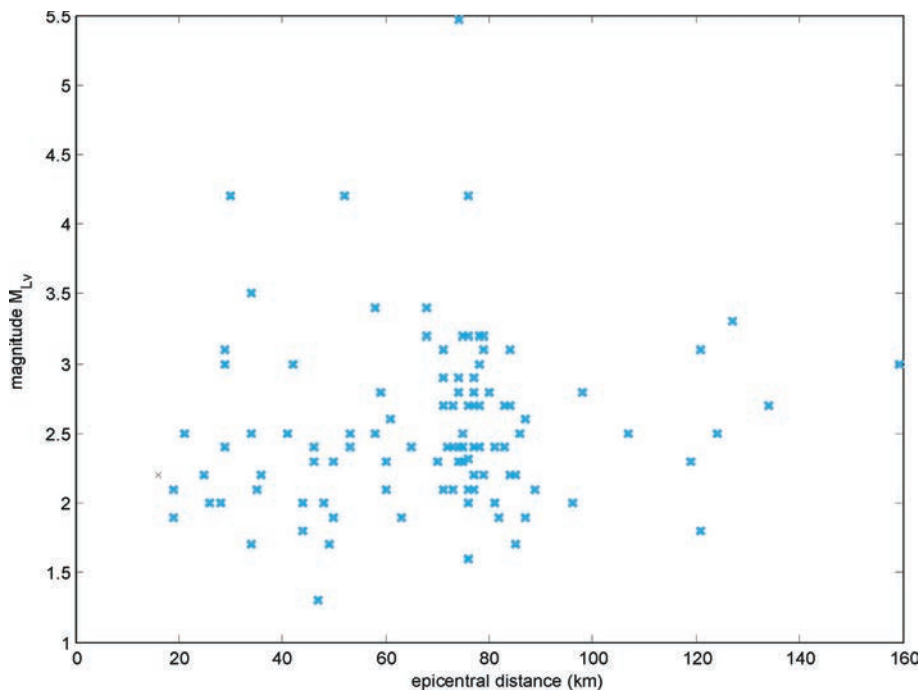


Figure 1. The distribution of epicentral distances with regard to the local magnitude of 109 earthquake records, recorded at the seismic station LJU, which were used to estimate the parameters used in the algorithm.

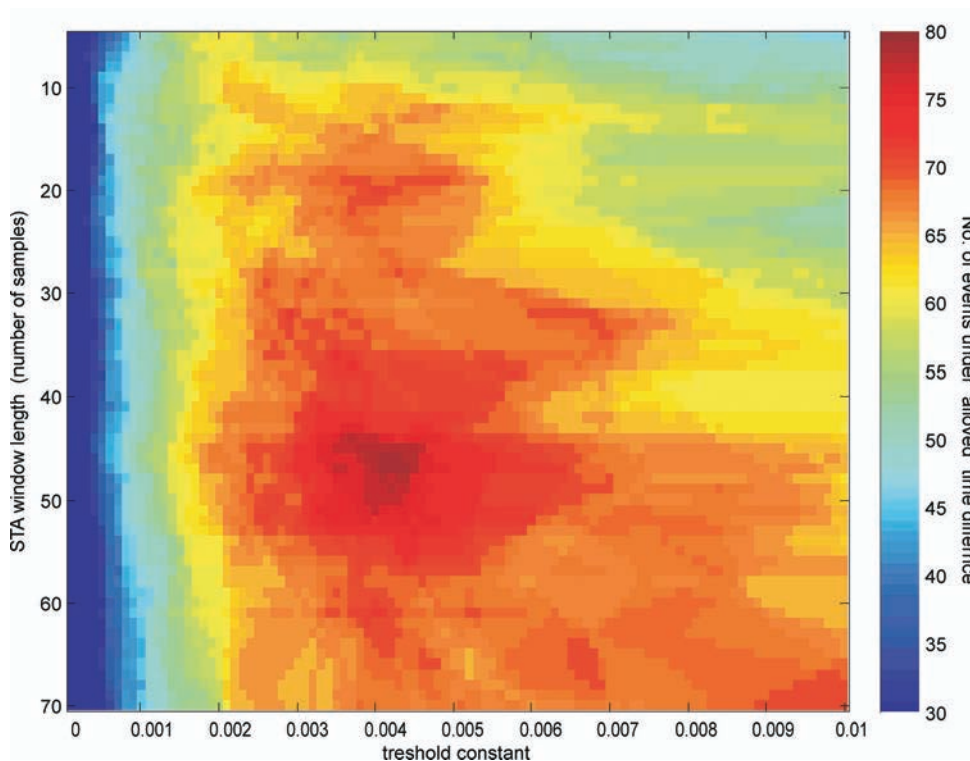


Figure 2. The number of events (colored), where the time difference between the "correct" first S seismic waves and the automatically estimated ones is less than 0.3 seconds. The sampling rate is 200 sps.

regard to the local magnitude is shown in Figure 1. All the events were detected and recorded automatically at the seismic station LJU, which is located near Ljubljana (Slovenia) and is equipped with a Guralp CMG40T seismometer and a Nanometrics RD3 digitizer. The sampling rate used at this station is 200 sps, and the pre-trigger time for automatic P seismic wave arrival detector is set to 10 seconds. Some of these earthquake records were very noisy. All these events were then manually checked by an expert (a seismologist on duty), who manually declared the time of the first P and S wave arrivals. Let us define that this is our reference time, which might not always be correct [17]. The fact is that a simple automatic procedure cannot replace expert knowledge, and for an automatic procedure it is difficult to estimate the allowed time difference between the "correct" manual picking of the first S seismic wave and the automatically estimated one. We will "define" the allowed time difference on the basis of using a single

station for an earthquake's location [18]. The time difference between the first S and P entries is proportional to the distance between the seismic station and the earthquake's hypocenter [19]. If the error between the "correct" and the estimated time difference is about 0.3 s, then the error in the estimated epicenter distance is less than 3 km, and in the case of using a single station for an earthquake's location, this error can be taken into account. If more than two seismic stations contributed in the automatic evaluation and these stations were distributed around the hypocenter, the error with respect to the earthquake's hypocenter location could be smaller, or even neglected [24]. We will use the value of 0.3 s as an allowed time difference in the procedure of the window length \mathcal{T} and the threshold constant definition. From Figures 2 and 3, the following parameters were evaluated: the window length (l) is 50 samples and the relative threshold level is 0.004.

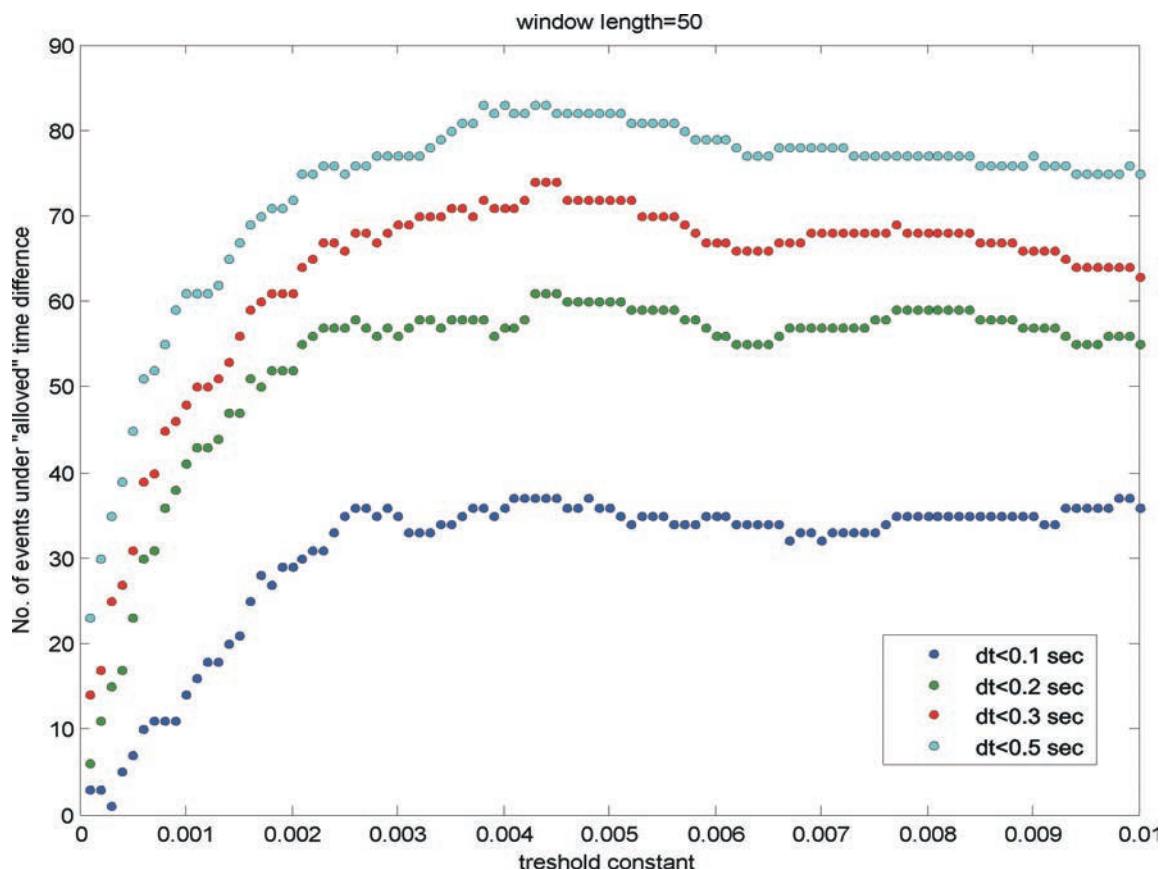


Figure 3. The number of events for different time differences between the "correct" first S seismic waves and the automatically estimated ones, for the STA window with 50 samples (the sampling rate is 200 sps), with regard to the constant value of the threshold level.

3 TEST AND RESULTS

Figures 4 and 5 depict two different earthquake records (their E-W, N-S and Z components), their characteristic signal and the evaluated S-wave arrival. The local magnitude of both events M_{LV} is 2.5, they differ with respect to the epicentral distances. In both cases the error between the "correct" and the estimated time difference is less than 0.1 s. For this time difference no manual retiming is needed [13]. However, for a deviation larger than 0.1 s, a retiming has to be performed, but under the assumption that more seismic stations will contribute their data in the procedure of the automatic location definition of the earthquake's parameters, a time interval, which was less than 0.3 s with regard to the "correct" time, will still give well-defined earthquake parameters. From our test set of 109 earthquake records this happens in 70% of cases. In reality, the automatic procedure is important in the case of a strong earthquake, where the earthquake's signal in a record is not affected by the seismic noise, and the probability that the location of an earthquake is defined correctly, is higher than from our test sets of data. Also, the time difference, which is larger than 0.3 s, can still present a satisfactory automatically calculated location of the earthquake. This statement can be presented in the next example of an earthquake (Figures 6 and 7), which occurred on 23 January 2009 at 04:28 local time. Its

local magnitude was 3.0 and it was felt in Ljubljana and Škofja Loka (Slovenia). The epicenter of this earthquake was estimated by an expert (using data from 29 seismic stations) as 14.41° longitude and 46.09° latitude. Figure 5 shows three seismograms of the vertical components recorded at seismic stations in the Slovenian seismic network (DOBS Dobrina, CESS Cesta, LJU Ljubljana). These stations are equipped with an NMX acquisition system [20] where our system of automatic location works, and for this earthquake only these stations contributed their data to the software for the automatic epicenter location. On each recording the arrivals of the P (red line) and S (green line) waves were automatically denoted and the earthquake's parameters, such as the coordinates of the epicenter (14.44° lon, 46.07° lat) and its magnitude (3.0), were calculated. For a comparison, the automatic and 'expert' times of the S wave's arrival at the station LJU are given in Table 1. The time difference between the manual and the automatic evaluation was 0.85 s, but the automatically defined location is still close to the real one (Figure 6).

Table 1. The automatic and the 'expert' times of the S-wave arrival at the station LJU for the earthquake in Figure 5.

	Time (UTC)
Manual (expert)	03h 28min 05.98sec
Automatic	03h 28min 06.82sec

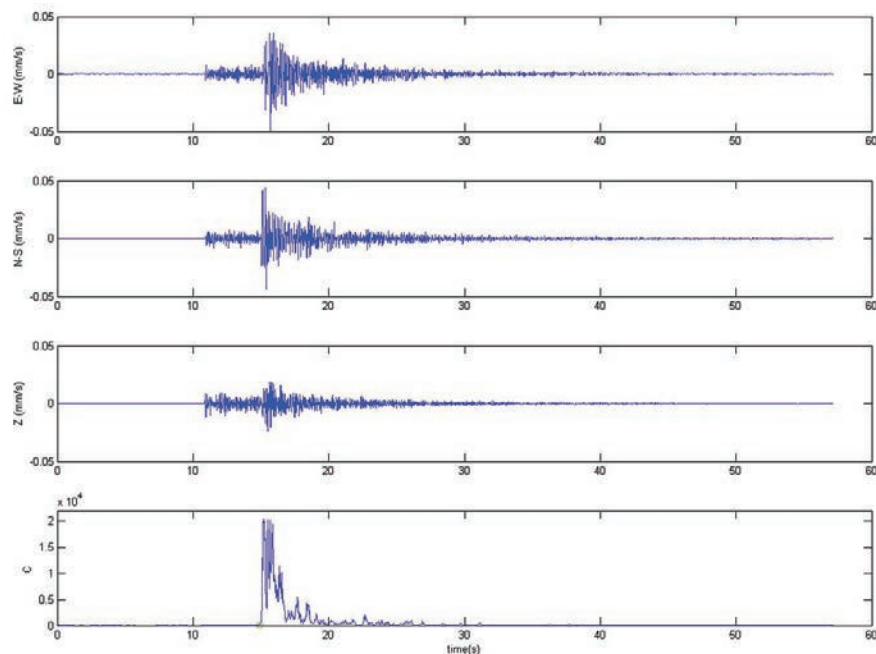


Figure 4. An event with magnitude M_{LV} 2.5 recorded at the three-component seismic station LJU at an epicentral distance of 29 km (E-W, N-S, Z traces). The system output is represented by a green circle, which represents the S arrival (C trace). The error between the "correct" and the estimated time difference is 0.07 s.

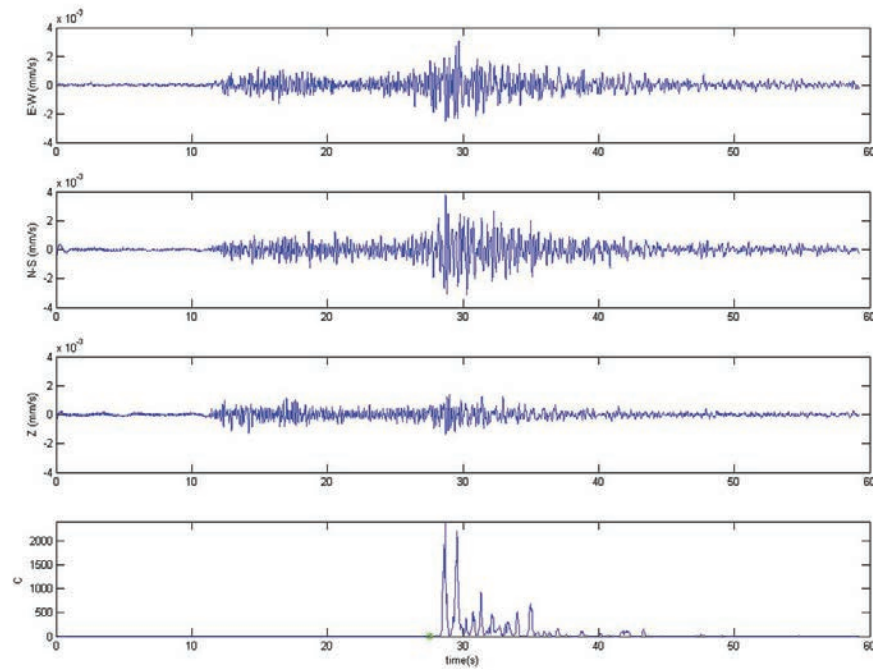


Figure 5. An event with magnitude M_{LV} 2.5 recorded at the three-component seismic station LJU at an epicentral distance of 124 km (E-W, N-S, Z traces). The system output is represented by a green circle, which represents the S arrival (C trace). The error between the "correct" and the estimated time difference is 0.09 s.

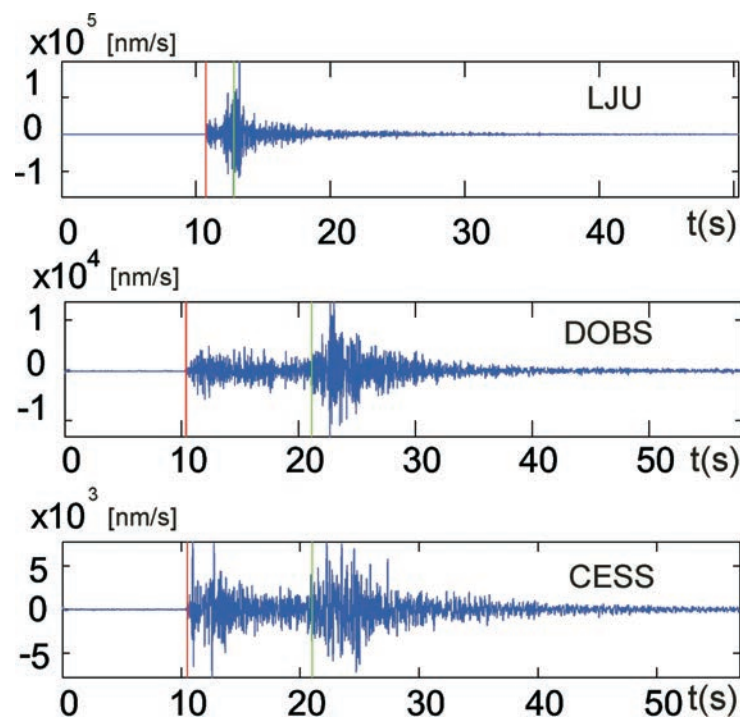


Figure 6. The record of an earthquake that occurred on 23 January 2009 at 04:28 local time. The seismograms of the vertical components were recorded at the seismic stations DOBS (Dobrina), CESS (Cesta) and LJU (Ljubljana). The arrival of the P (red line) and S (green line) waves was automatically denoted.

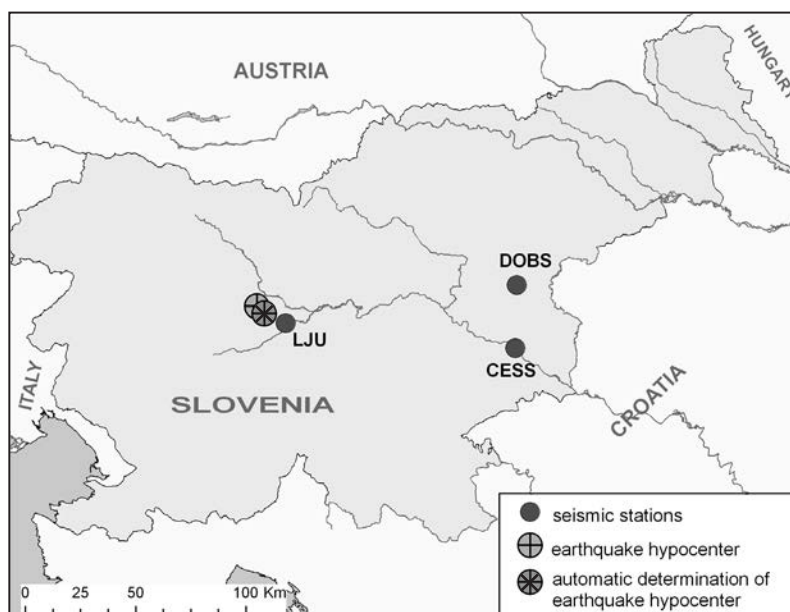


Figure 7. The map showing the locations of the seismic stations that contributed their data to the automatic determination of the earthquake's parameters, the hypocenter of the earthquake and the automatic determination of the hypocenter's location. Even with this small number of seismic stations, the automatic location is still close to the real one.

4 CONCLUSIONS

An automatic procedure for the P and S phase picking could not completely replace the human experts and their knowledge, but are very important for the primary and rapid estimation of the earthquake's parameters. The clearest phase to pick is usually the P wave, which is also the case in the automatic procedure. When a small number of seismic stations contribute their data to the automatic procedure, S-phase picking is desired. Using phases with different velocities enables a better estimation of the epicenter's location. Our procedure to estimate the S-wave arrival time has been in practical daily use in the seismic network of Slovenia since 2002. The energy analysis used in our procedure is primarily suitable for local earthquakes. A procedure, also taking the frequency content into account, should be used for earthquakes with larger epicentral distances.

REFERENCES

- [1] Freiberg, W.F. (1963). An approximation method in signal detection. *Quart. J. App. Math.* 20, 373-378.
- [2] Joswing, M. (1990). Pattern recognition for earthquake detection. *Bulletin of the Seismological Society of America*, 80, 170-186.
- [3] Allen, R. V. (1978). Automatic earthquake recognition and timing from single traces. *Bulletin of the Seismological Society of America*, 68, 1521-1532.
- [4] Houlston, D.J., Waugh, G., Lazughlin, J. (1984). Automatic Real-Time Event Detector for Seismic Networks. *Computers and Geosciences*, 10, 431-436.
- [5] Bear, M., Kradofler, U. (1987). An automatic phase picker for local and teleseismic event. *Bulletin of the Seismological Society of America*, 77, 1437-1445.
- [6] Pisarenko, V. F., Kushnir, A. F., Savin, I.V. (1987). Statistical adaptive algorithms for estimation of onset moments of seismic phases. *Physics of Earth and Planetary Interiors*, 47,4-10.
- [7] Roberts, R. G., Christofsen, A., Casidy, F. (1989). Real time event detection, phase identification and source location estimation using single station three-component seismic data. *Geophysical Journal International*, 97, 471-480.
- [8] Takanami, T., Kitagawa, G. (1993). Multivariate time-series model to estimate the arrival times of S waves. *Computers and Geosciences*, 19, 295-301.
- [9] Charutti, C., Salemi, G. (1993). Artificial intelligence techniques in the analysis of digital seismograms. *Computers and Geosciences*, 19, 149-156.

- [10] Joswing, M. (1995). Automated classification of local earthquake data in the BUG small array. *Geophysical Journal International*, 120, 262-286.
- [11] Dai, H., MacBeth, C. (1995). Automatic picking of seismic arrivals in local earthquake data using an artificial neural network. *Geophysical Journal International*, 120, 758-774.
- [12] Cichowicz, A. (1993). An automatic S-phase picker, *Bulletin of the Seismological Society of America*, 83, 180-189.
- [13] Wang, J., Teng, T. (1997). Identification and picking S phase using an artificial neural network. *Bulletin of the seismological Society of America*, 87, 1140-1149.
- [14] Tasič, I. (2000). Characterization of seismic waves arrival with simulated neural networks. Faculty of Mechanical Engineering, Ljubljana 2000.
- [15] Saragiotis, C.D., Hadjileontiadis, L.J., Savva, A.S., Papazachos, C.B. Panas, S.M. (2000). Automatic S-phase arrival determination of seismic signals using nonlinear filtering and higher-order statistics, Geoscience and Remote Sensing Symposium, 2000. *Proceedings. IGARSS 2000. IEEE 2000 International*, Vol 1, 292-294., 24-28 July 2000.
- [16] Tong, C. and Kennett, B.L.N. (1996). Automatic seismic event recognition and later phase identification for broadband seismograms. *Bull. Seism. Soc. Am.* 86, 1896-1909.
- [17] Bai, C.Y., Kennett, B.L.N. (2001). Phase identification and attribute analysis of broadband seismograms at far-regional distances. *Journal of Seismology* 5, 217-231.
- [18] Earle, P. (1997). The Picking Procedure http://mahi.ucsd.edu/research_projects/Autopicker/autopicker/node3.html.
- [19] Douglas, A. (1997). Bandpass filtering to reduce noise on seismograms: Is there a better way? *Bull. Seism. Soc. Am.* 87, 770-777.
- [20] Tasič, I. (2001). Nanometrics's Digital Seismic Network, Potresi v letu 1999 (ed. R. Vidrih), ARSO, Urad za seizmologijo, 68-72.
- [21] Tasič, I. (2001). Classification Of Arrival Times Of Local Earthquake Seismic Waves, Potresi v letu 1999 (ed. R. Vidrih), ARSO, Urad za seizmologijo, 83-93.
- [22] Tasič, I. (2006). Automatic Quantification Of Earthquake Parameters At A Single Seismic Station, Potresi v letu 2004 (ed. R. Vidrih), ARSO, Urad za seizmologijo, 83-93.
- [23] Lay, T., Wallace, T.C. (1995). *Modern Global Seismology*. Academic Press, S. Diego, USA.
- [24] Bormann P. Ed. (2002). *New Manual of Seismological Observatory Practice*. GFZ Potsdam, Germany.

MERJENJE IN INTERPRETACIJA TOGOSTI MELJASTEGA PESKA IZ BOŠTANJA PRI ZELO MAJHNIH DEFORMACIJAH

GREGOR VILHAR IN VOJKAN JOVIČIČ

o avtorjih

Vojkan Jovičič
Inštitut za rudarstvo, geotehnologijo in okolje (IRGO)
Slovenčeva 93, 1000 Ljubljana, Slovenija
E-pošta: vojkan.jovicic@irgo.si

vodilni avtor

Gregor Vilhar
Zavod za gradbeništvo Slovenije (ZAG Ljubljana)
Dimičeva 12, 1000 Ljubljana, Slovenija
E-pošta: gregor.vilhar@zag.si

izvleček

V članku je predstavljeno merjenje in interpretacija meritev z bender elementi na meljastem pesku iz Boštanja. Vzorci so bili pripravljani pri različnih začetnih količnikih por in obremenjeni v izotropni kompresiji do 5MPa. Tehniko merjenja z bender elementi smo uporabili za določitev dinamičnega strižnega modula (G_0) materiala pri zelo majhnih deformacijah. Zanesljivost meritev smo povečali z uporabo skupine signalov z različnimi frekvencami vzbujanja. Togost G_0 je bila določena z uporabo treh različnih pristopov, in sicer: a) časovnega prihoda vala, b) spremembe faze in c) navzkrižne korelacije. V članku so pojasnjene razlike med vrednostmi G_0 glede na uporabo določenega pristopa, ki so se sistematično pojavljale. Prikazano je spreminjanje togosti G_0 meljastega peska iz Boštanja v ravnini $\log G_0 - \log p'$ in primerjave z drugimi peski.

ključne besede

meljast pesek, triosne preiskave, togost pri zelo majhnih deformacijah, bender elementi, meritve v časovni in frekvenčni domeni

MEASUREMENT AND INTERPRETATION OF THE SMALL STRAIN STIFFNESS OF BOŠTANJ SILTY SAND

GREGOR VILHAR and VOJKAN JOVIČIĆ

About the authors

Vojkan Jovičić
Institute of Mining, Geotechnology and Environment (IRGO)
Slovenčeva 93, 1000 Ljubljana, Slovenia
E-mail: vojkan.jovicic@irgo.si

corresponding author

Gregor Vilhar
Slovenian National Building and Civil Engineering Institute
(ZAG Ljubljana)
Dimičeva 12, 1000 Ljubljana, Slovenia
E-mail: gregor.vilhar@zag.si

Abstract

This paper presents measurements, and an interpretation of these measurements, based on the use of bender-element probes for Boštanj silty sand. The samples were prepared at different initial void ratios and isotropically compressed up to 5 MPa. The bender-element technique was used to determine the dynamic shear modulus (G_0) of the soils at very small strains. The multiple bender-element probes were shot at different excitation frequencies in order to increase the reliability of the measurements. The G_0 stiffness was determined by using three different techniques: a) the first-time arrival, b) the phase-change method and c) the cross-correlation method. The systematic differences observed between the G_0 values, calculated using the three techniques, are discussed. The variation of G_0 in the $\log G_0 - \log p'$ plane was evaluated for the Boštanj silty sand and compared with other sands.

keywords

silty sand, triaxial testing, small strain stiffness, bender elements, time-domain and frequency-domain measurements

1 INTRODUCTION

By using bender elements, the shear stiffness (G_0) of a material at very small strains ($\varepsilon < 10^{-5}$) can be measured during conventional laboratory tests. In the past few decades it was recognised that the so-called elastic stress-strain response of soils and soft rocks is highly non-linear and often anisotropic. The bender-element technique represents one of the ways of measuring the stiffness at the very beginning of this non-linearity and it can capture the anisotropic features of small strain stiffness.

The use of bender elements in geotechnics began in the late 1970s with Shirley and Hampton [22] and later with Dyvik and Madshus [10], who showed very good agreement between the results obtained by the bender elements and with resonant-column tests. The advantages of this method lie in its relatively simple installation, low cost and the non-destructive nature of the measurement. It was made possible to install bender elements as a complementary measurement technique in various types of laboratory equipment, such as triaxial cells, oedometers, direct shear, hollow cylinder, true triaxial, cubical cell and the resonant column apparatus, Fonseca et al. [12]. However, some problems concerning the proper use of the technique and the interpretation for the different installations have evolved; see, for example, [7, 23, 17].

The set-up for the bender-element test in a triaxial cell is presented in Figure 1. A bender element is a piezoceramic element made of two transversely poled plates that are bonded together. When one end of the element (the transmitter element in the figure) is fixed the excitation of the external voltage will make the opposite end move and the element will bend in the direction normal to the face of the plates. In ideal conditions the transmitter element, embedded in the soil sample, introduces a shear wave into it. Upon the arrival of the shear wave at the other end of the soil sample the receiver element will move and generate a small voltage, which is detected at the electrode and shown on an oscilloscope. The technique is based on a measurement of the arrival time

of the shear wave, assuming a plane-wave propagation, i.e., the time difference between the excitation of the transmitter and the excitation of the receiver element, as indicated in Figure 1.

On the basis of this assumption, the shear-wave velocity (v_s) can be calculated from the current travel distance of the wave (D) and the time of the arrival of the wave at the receiver element (t_{arr}), according to Equation

(A.1) in the Appendix. The distance D was taken as the current tip-to-tip distance of the bender elements, which is experimentally supported by Dyvik and Madhus [10], Brignoli et al. [6], Viggiani and Atkinson [23], and Fernandez [11]. The shear modulus at a very small strain (G_0) can be calculated from the current bulk density of the material (ρ) and the previously calculated shear-wave velocity, according to Equation (A.2).

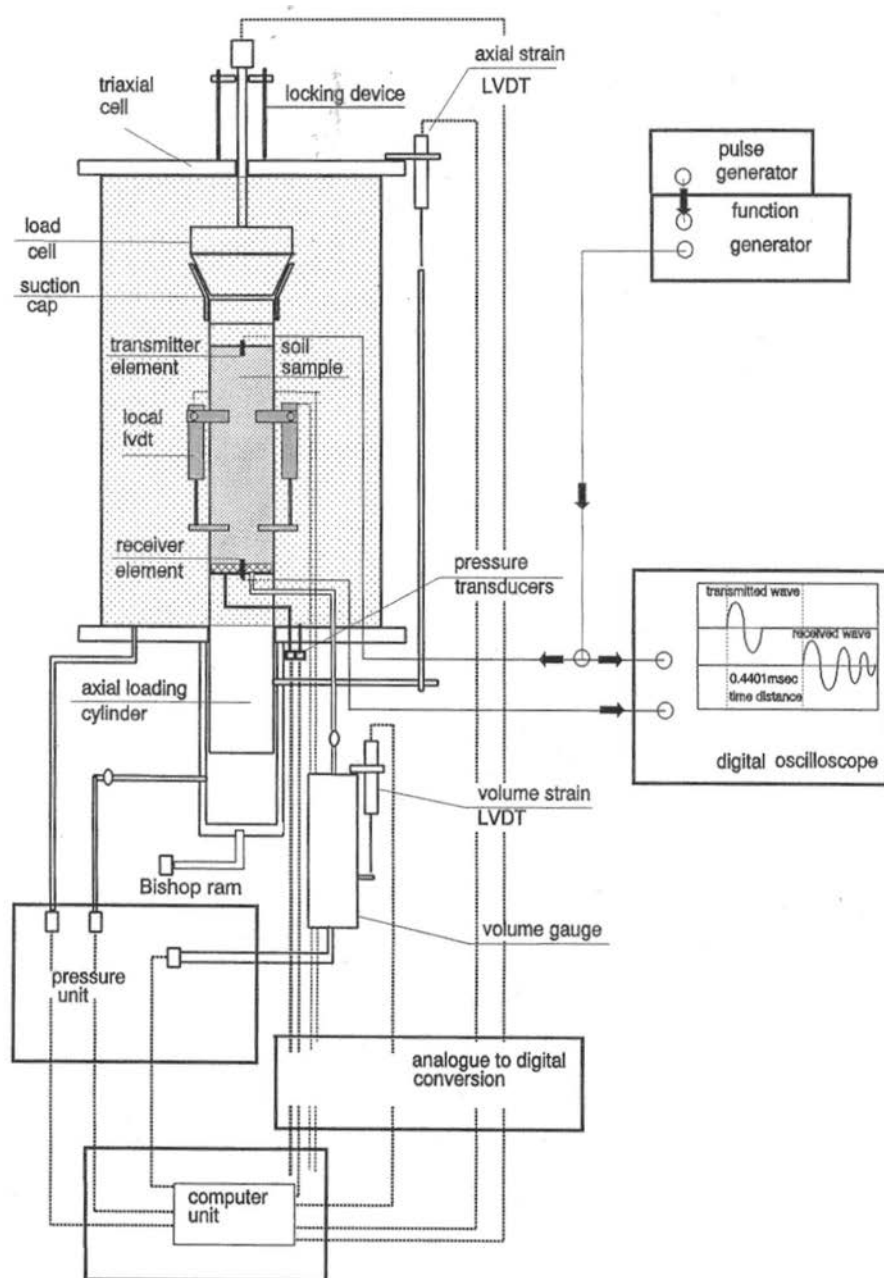


Figure 1. The set-up for the bender-element test in a triaxial cell (after Jovičić [16]).

2 MATERIAL AND LABORATORY TESTING PROCEDURE

The material used for this research was a silty sand from a railway-line embankment near the town of Boštanj, Slovenia. Some aspects of the static and dynamic behaviour of the same material can be found in Lenart [19]. The sieve and sedimentation analyses shown in Figure 2 revealed that Boštanj silty sand consists of fine sand with 30% of non-plastic silt. It is a well-graded material with a uniformity coefficient $C_u = 0.721$ and a mean particle size $D_{50} = 0.11$ mm. The particle specific gravity G_s is 2.75.

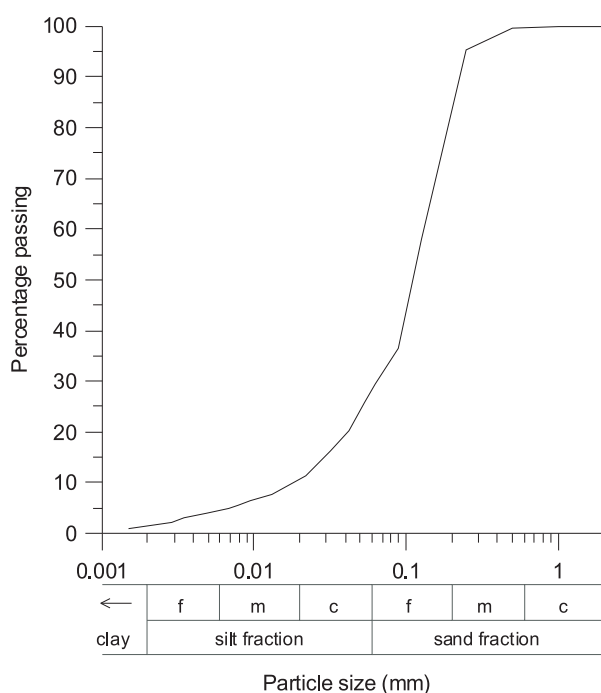


Figure 2. Particle size distribution of the Boštanj silty sand.

In total, nine triaxial tests were carried out with the aim being to measure the effect of the density and the stress state on G_0 in isotropic compression. The samples were prepared at different initial void ratios using the moist-tamping method.

A predetermined amount of slightly wet material, with a water content of $w = 10\%$, was placed in a mould in 10 equal weight portions. Each portion was compacted with a flat tamper of a circular shape with a diameter equal to half of the sample's diameter to achieve the desired equal height of each layer. The samples were saturated by raising the pore-water pressure to reach B values higher than 0.95. Two types of triaxial apparatus were used, i.e., a standard

pressure apparatus achieving a maximum cell pressure of 0.8 MPa and a high-pressure triaxial apparatus achieving a cell pressure of up to 5 MPa, both at Imperial College Soil Mechanics Laboratory. Four tests were performed on the standard pressure apparatus and five tests on the high-pressure apparatus. The schematic diagrams of both apparatus are similar to that shown in Figure 1.

The standard pressure cell is a Bishop & Wesley type of cell. It is a fully computer-controlled cell, equipped with local axial strain-measuring inclinometers, directly glued to the sides of the sample. The cell was also fitted with a pair of bender elements, mounted in the top-cap and bottom-pedestal for measuring the velocity of vertically propagating, horizontally polarised, shear waves. The dimensions of the bottom element were width (13.0 mm) x sample protrusion (4.5 mm) x thickness (1.5 mm), and of the top element were width (15.0 mm) x sample protrusion (4.5 mm) x thickness (1.5 mm). The sample dimensions were around 38.5 mm in diameter and 90.0 mm in height. Such a high slenderness ratio of was used because of the existing mould dimensions.

The high-pressure triaxial cell was capable of applying a maximum radial stress of 5 MPa. Both the cell and axial stresses have alternative low- and high-pressure systems. This cell is also fully computer controlled. A pair of axial LVDTs [9] and a LVDT-fitted radial belt were glued to the sides of the sample. A pair of bender elements for measuring the velocity of axially propagated shear waves was also installed in this cell, having the following dimensions: the bottom element, width (11.5 mm) x sample protrusion (3.8 mm) x thickness (1.5 mm), and the top element, width (11.5 mm) x sample protrusion (5.8 mm) x thickness (1.5 mm). The sample dimensions were around 50 mm in diameter and 110 mm in height.

3 INTERPRETATION OF THE BENDER-ELEMENT TEST ON THE SAMPLES OF BOŠTANJ SILTY SAND

3.1 INTERPRETATION TECHNIQUES

The main reason for the difficulties in the interpretation of the bender-element test was the lack of understanding of the interaction of the bender-element system and the soil sample during the measurement. Most often, this interaction results in dispersion, meaning that the initial excited wave at the transmitter element spreads into different components, propagating at different speeds,

frequencies and along different paths. The presence of the mixture of the components could therefore mask the detection of the actual arrival of the shear wave at the receiver element, which characterises the shear velocity of the medium. Furthermore, to what extent the output signal appears distorted depends directly on the number of vibration modes excited by the propagated wave.

The most widely dealt type of dispersion has been the near-field effect. It is usually recognised as an initial drop in signal, having a different polarity than the driving signal, as shown in Figure 3. Different criteria have

been proposed in order to minimize this effect, mostly in terms of the minimum number of shear wavelengths between the transducers, see, for example, [21, 17, 4]. Taking into account such criteria, the experimental and numerical analyses indicate that other types of dispersion are also supposed to have a strong influence on the observed distortion of the bender-element signals (Arroyo et al. [4]), in particular those still evident at higher frequencies than the near-field criteria would predict. Current knowledge suggests that there is also an evident geometrical effect on the propagation pattern in the bender-element system, see, for example, [20, 3].

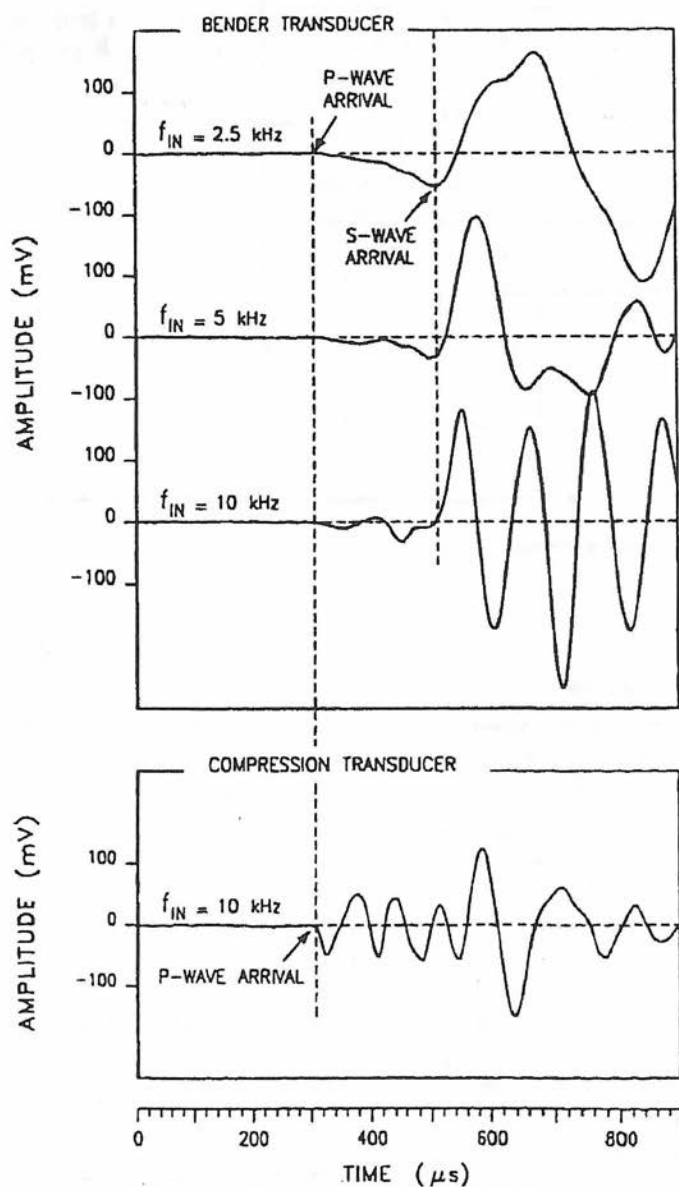


Figure 3. Near-field effect and the detection of the arrival of the compressive components before the actual shear wave with the compression transducer (after Brignoli et al. [6]).

In terms of interpretation, the methods can be classified into two main groups: the time-domain methods and the frequency-domain methods. In the time domain, the user visually determines the arrival time of the shear wave by examining the output and input signal voltages versus time. In the frequency domain, the stored input and output signals are transformed and manipulated in the frequency domain.

Both groups of interpretation methods were focused on minimizing the influence of the dispersion effects. In the time domain this can be achieved by adapting the frequency of the transmitted pulse. The most commonly used type of signal in the time domain is the single sine pulse, as it contains a predominant single frequency and this can help to avoid the near-field effect. The distortion of the right shape of the sine signal was shown experimentally to effectively reduce the near-field effect (Jovičić et al. [17]). The effectiveness of this type of pulse signals has also been proven numerically (Arroyo et al. [4]). All current time-domain methods rely on a visual identification of the arrival time of the shear wave, whereas different researchers have preferred different geometrical features of the output signal as an arrival point (e.g., the first rise of the signal, the first change of curvature, the first peak and the peak-to-peak between the input and output signals). However, the real physical meaning of the arrival time is the first rise of the received signal, and this is why the method was used here for the interpretation. The first change of the curvature or the peak-to-peak are the subject of an interpretation of how the receiver responded to the incoming wave, so that a variability between the results obtained from the different criterion/input signal combination is expected and can be substantial, as shown by Arroyo et al. [4] and Alvarado [1]. Concerning mostly the frequency-domain interpretation, the pulse signals along with the harmonic continuous signals at a constant frequency and linearly swept sine signals of different frequency ranges have also been used [13, 1, 12]. In the present study, the methods of first arrival and cross-correlation were employed in the time domain, while in the frequency domain, the phase-change method was used. All the methods are described in some detail, while the relevant equations are presented in the Appendix. In all the cases, the single sine pulses were used at different excitation frequencies from 1 to 50 kHz. The data were analysed using computer codes written in Matlab 7.3.

The main deficiency of all the interpretation methods is the subjectivity of the user involved in the interpretation of the shear-wave arrival time. There have been some attempts to make the interpretation more objective in the frequency domain using computer software (e.g.,

Fonseca et al. [12]), but the user still has to determine the proper frequency interval and decide among the calculated values of the time arrival. The level of reliability can be different, depending on the different test conditions or materials (Alvarado & Coop [2]). Therefore, the use of a combination of measurement and interpretation methods is proposed, leading to a higher level of confidence in the computed arrival time, whereas no single combination of interpretation criterion/selected input signal is universally accepted. The use of multiple methods has also been supported by the recent reports of Technical Committee TC29 of the ISSMGE [14,24].

Three different ways of interpreting the results were used along with the calculated error in G_0 : the first arrival time, the cross-correlation and the frequency-domain method of the phase change. The single-shot sine pulses have been used as the driving signals for both the time- and frequency-domain interpretations. Figure 4 shows the comparison of the transfer functions calculated using sine-pulse signals at different excitation frequencies and continuous sine signals of discretely varying frequencies for each point for Toyoura sand [1]. The transfer-function gain and the stacked phase are defined in the Appendix using Equations (A.6) and (A.7). In a certain frequency domain, i.e., between 6 and 12 kHz, a good match between the slope of the stacked phase against the frequency is found and, as will be explained later, the group time arrival can be easily calculated.

3.2 INTERPRETATION OF THE TIME-DOMAIN MEASUREMENT

In the time domain, the method of first arrival was used. The signals from the probes with different excitation frequencies in a certain stress state were collected on the same plot. The data were normalised and offset with respect to the beginning of the sent signals, as shown in Figure 5. Afterwards, the arrival time was estimated according to the well-pronounced sharp change in polarity in the same direction and of a similar shape to the input signal. It can be observed in Figure 5 that by increasing the input frequency to 20 kHz the change in the polarity becomes sharper. Higher frequencies are not relevant because of the poor coupling between the bender elements and the soil (the phenomena of overshooting, Jovičić et al. [17]), but are added to the plot as a reference.

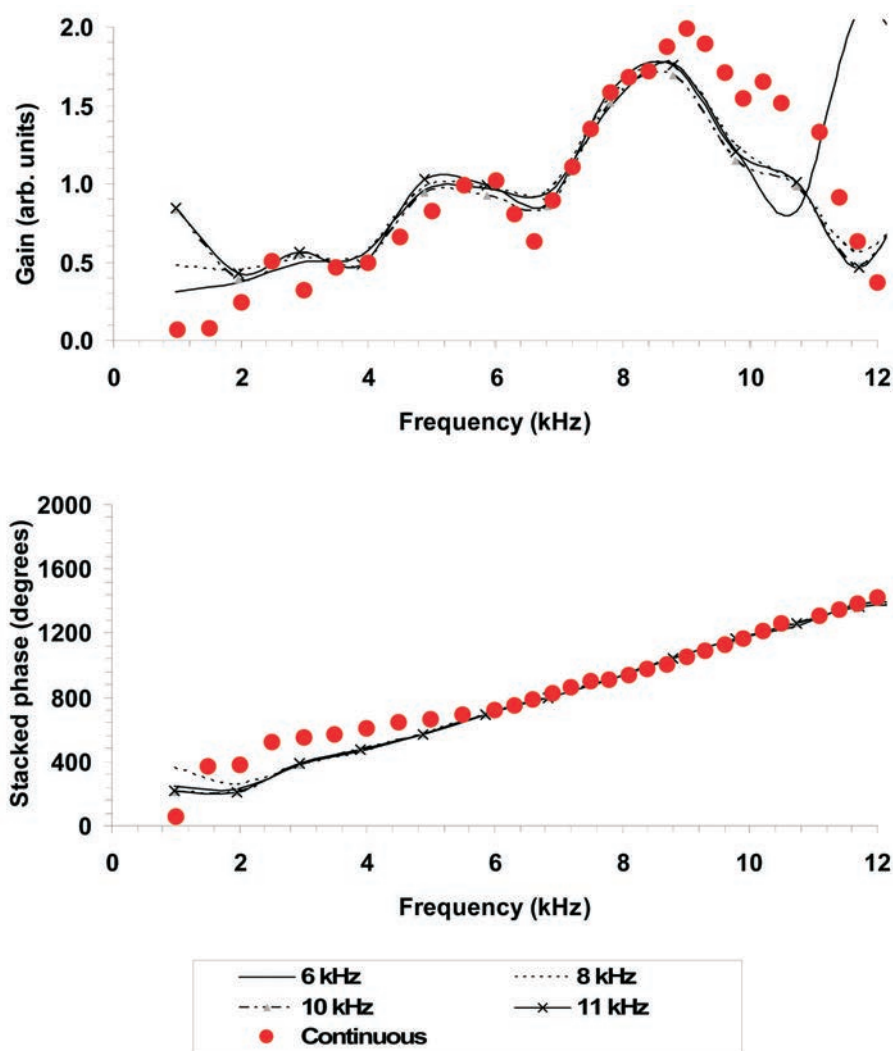


Figure 4. The good match of the transfer function for Toyoura sand at $p' = 220$ kPa, calculated from the sine pulse signals at different excitation frequencies and continuous sine signals with discretely varying frequencies (after Alvarado [1]).

By increasing the mean effective stress p' , the signals become more distorted, but, on the other hand, the arrival points, for certain frequencies, can be distinguished more easily (Figure 6). This method relies on two factors: a) the measurement should be taken at excitation frequencies that ensure a minimisation of the influence of the near-field effect and b) at this range of frequencies a comparison should be made for several different signals on the same plot. In this way the frequency-dependent patterns of the behaviour of the system can be visually recognised and the signal with the sharpest arrival pattern can be chosen to be relevant for the identification of the arrival point.

It can be seen in Figure 6 that the output signals have an initial bump of the same shape and polarity positioned almost at the same time as the bump of the input signals appears. The reason for these bumps is the leakage of the input signal through the conductive medium (i.e., the pore water) from the transmitter to the receiver, called the 'cross-talk' (Figure 7). The solution to this problem is usually the proper grounding of the elements. In our case, the contaminated parts of the signals were replaced by the uniformly distributed pseudo-random noise of small amplitude, using Matlab's rand function. This replacement only has an effect on the frequency-domain calculation, while the cross-talk part contaminates the frequency content of the output signal and, as such, affects the time-arrival calculation.

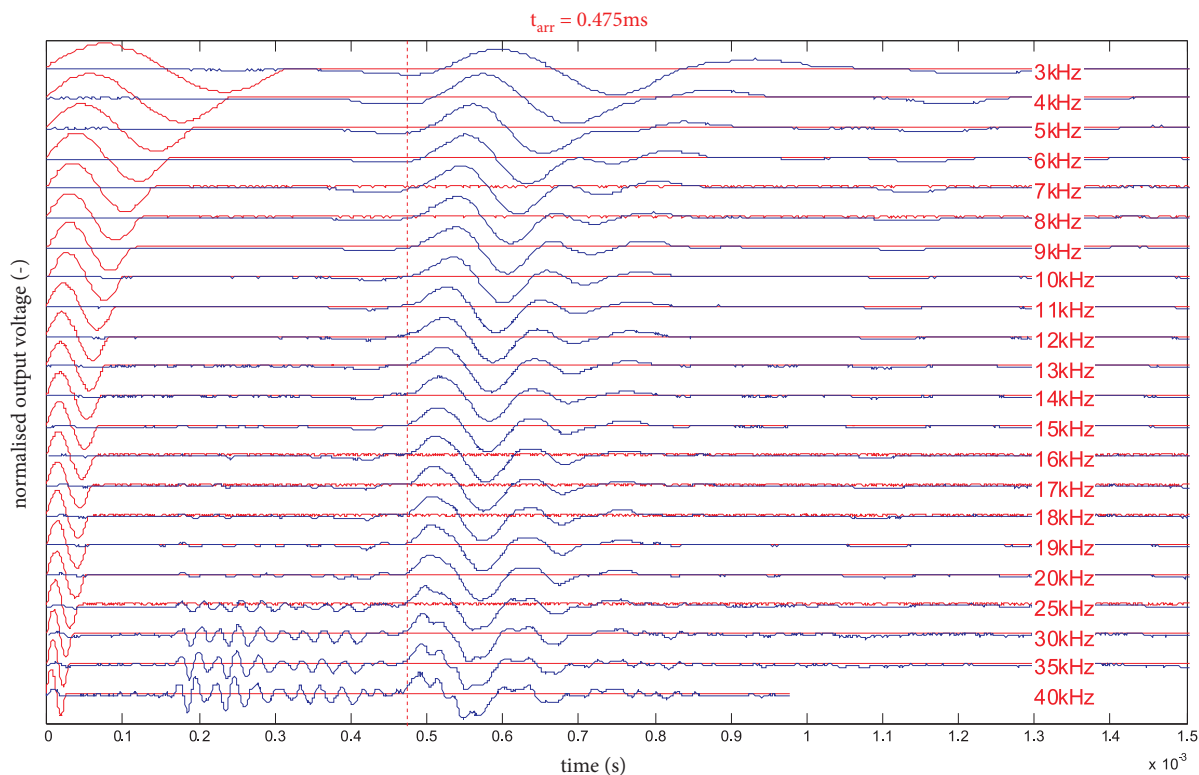


Figure 5. Input (red) and output (blue) signals from the bender-element probes for the sample BO-I-J at $p' = 200$ kPa. The increase in the sharpness of the arrival-time point with increasing frequency up to 20 kHz can be seen.

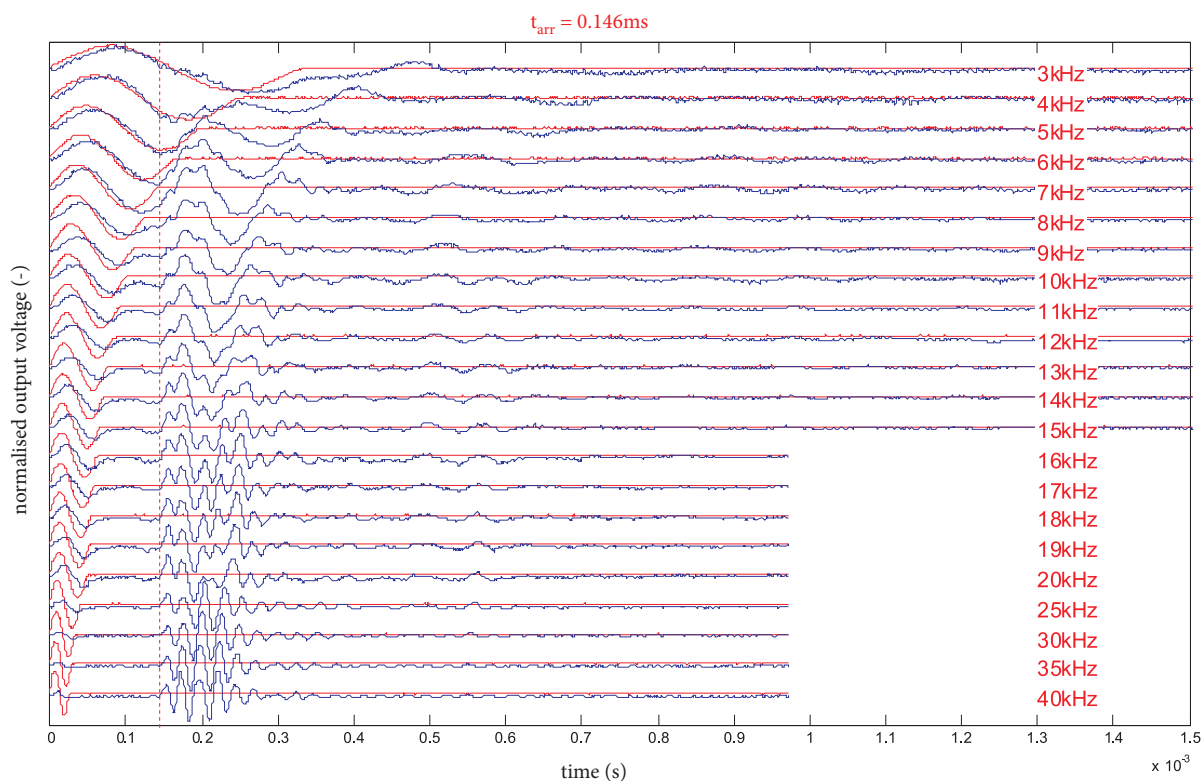


Figure 6. Input (red) and output (blue) signals from the bender-element probes for the sample BO-I-J at $p' = 4700$ kPa. Distorted signals due to high stresses and high density of the sample can be seen. The arrival time can be distinguished more easily.

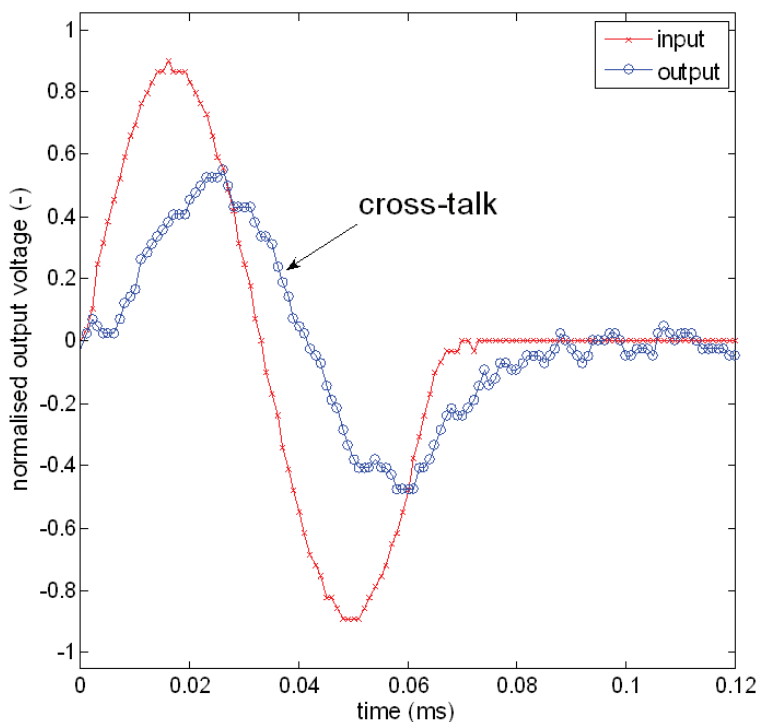


Figure 7. Contamination of the output signal with cross-talk.

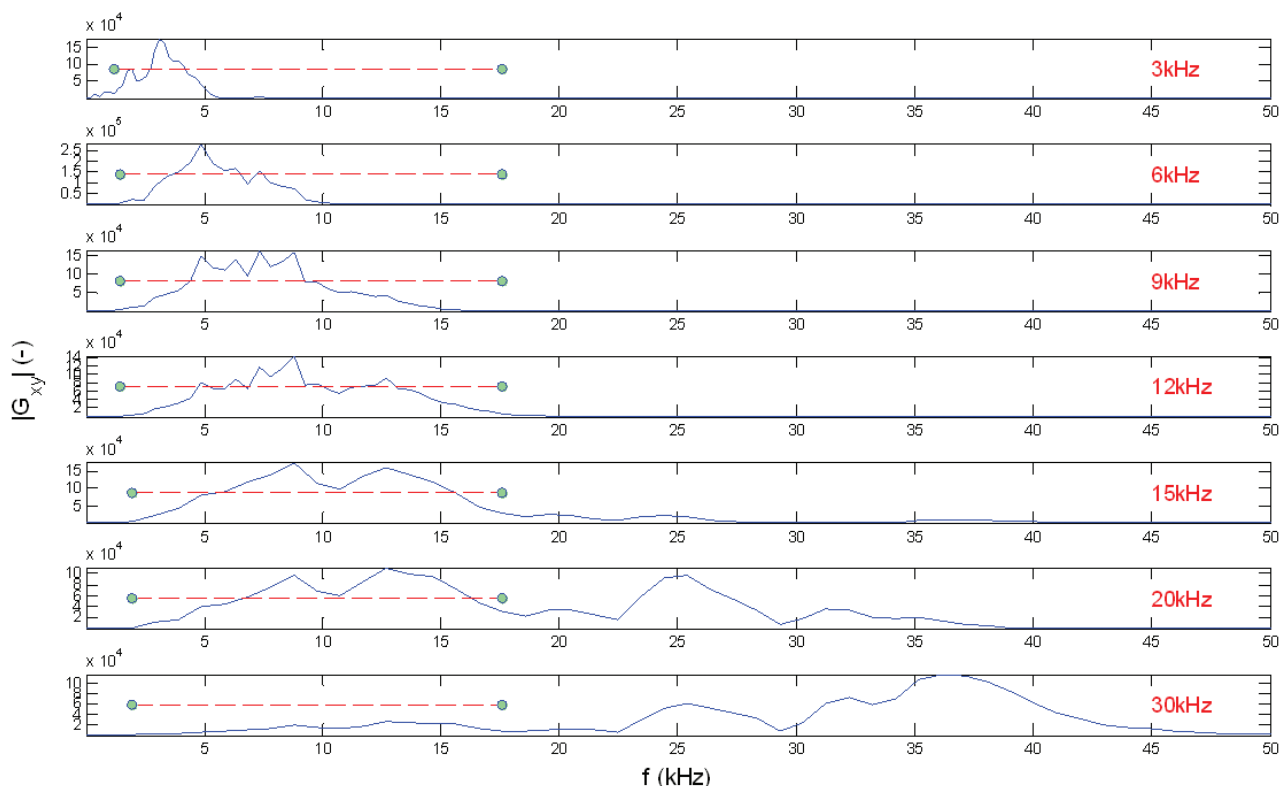


Figure 8. Cross spectrum magnitudes $|G_{xy}|$ versus frequency f for the sample BO-I-J at $p' = 1300$ kPa, using input sine-pulse signals at different frequencies (the values on the right-hand side of plots). The chosen frequency interval for the t_g calculation is also marked.

3.3 INTERPRETATION OF THE FREQUENCY-DOMAIN MEASUREMENTS

The frequency-domain method consists of interpreting the phase change between the transmitted and received signals. The whole input and output signals were transformed into the frequency domain using a fast Fourier algorithm (FFT). The analysis began by plotting the cross-power spectra magnitude $|G_{xy}|$ versus the frequency for selected signals at a chosen stress-state, as shown in Figure 8. The expression for G_{xy} can be found in Equation (A.4). At each frequency, the magnitude $|G_{xy}|$ is a product of the amplitudes of both signals at that frequency.

The analysis proceeded with the plots of the stacked (unwrapped) system phase factor ϕ versus frequency (Equation (A.7)) for all the chosen signals. Figure 9 shows only one such plot (at $f = 15\text{kHz}$) in order to clearly see the content. By plotting $|G_{xy}| - f$, the frequency ranges are observed common to both the input and output signals. The widest possible frequency interval covering the linear relation of $\phi - f$ is then chosen (marked by two blue dots connected with the dashed line in Figures 8 and 9). The chosen interval should cover most of the major amplitudes in the $|G_{xy}| - f$ plots, but the deficiency of the methods is that a slight change in the frequency interval could cause

a big change in the calculated arrival time. Therefore, to increase the robustness of the approach, the widest, still highly linear, interval of f in the $\phi - f$ plot, covering most of the major amplitudes in $|G_{xy}| - f$, must be chosen. From the value of the slopes $\frac{d\phi}{df}$ of the least-squares-fit lines of the chosen frequency interval, the group time arrivals (t_g) were calculated (Equation (A.10)).

The tangents were calculated in the linear range of the strong amplitudes of the transmitted and received signals, meaning that the calculated group time arrival t_g is supposed to be the arrival time of the main shear wave packet and, therefore, the group time arrival is assumed to be equal to the shear-wave time arrival ($t_g \cong t_{arr}$).

All of the signals were then plotted in the time domain along with the marked positions of the calculated group arrival times (Figure 10). The proper value of t_g was then chosen using Figure 8 and all of the $\phi - f$ plots with superimposed linear trends at chosen intervals. The correlation coefficient (ρ_{xy}) between the linear trend and the data can serve as a guide for choosing the right value. In the presented case the t_g values from the signals with 9, 12, 15 and 20 kHz were of the best quality. The signal with the frequency of 30 kHz is likely to experience overshooting because of the high frequency;

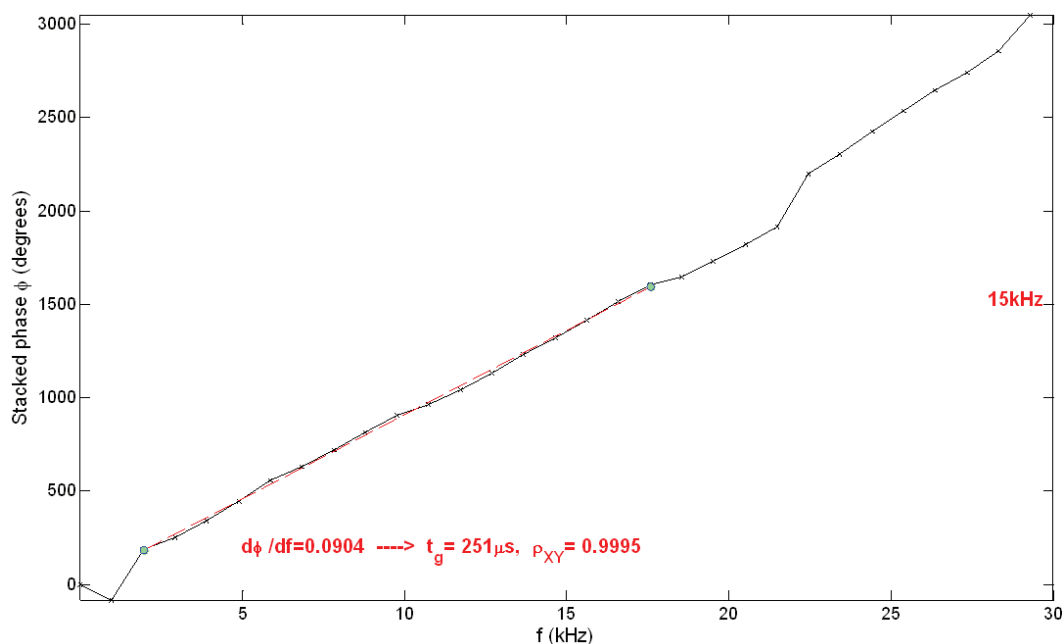


Figure 9. Stacked (unwrapped) system phase factor ϕ versus frequency f for the sample BO-I-J at $p' = 1300\text{ kPa}$, using the input sine pulse signal at 15 kHz . (The properly chosen frequency interval covering the widest linear range is also shown, along with the value of the slope $\frac{d\phi}{df}$, the group time arrival t_g and the correlation coefficient ρ_{xy} between the data and the shown linear trend.)

therefore, it is disregarded from the group. The average value of t_g for the four candidate signals could be taken, or the $t_g = 0.251$ (signal at 15kHz) was chosen due to the highest correlation coefficient. The $\phi - f$ plot of the 15-kHz signal is shown in Figure 9. A good match for the linear least-squares trend and the data can be observed.

It can be seen from Figure 10 that the calculated group arrival time t_g of the four appropriate signals along with the frequency intervals does not depend much on the excitation frequency. The very different values of t_g for the signals of 3 and 6 kHz are likely to be due to the very dispersive nature of both signals caused by the presence of the near-field effect in the receiving wave. Figure 11 demonstrates this, showing the $\phi - f$ plot for 6 kHz along with the poor linear trend. If the frequency interval is changed to cover the narrower range of 2–12 kHz, the calculated t_g value is 0.265 ms and the coefficient of correlation is substantially improved to 0.9959.

3.4 INTERPRETATION OF THE CROSS-CORRELATION MEASUREMENTS

The arrival times t_{arr} were also calculated using the cross-correlation function $CC_{XY}(t)$ (Equation (A.11)). Using this method, it is assumed that the shapes of the transmitted and received signals are very similar, i.e., of equal frequency content. The main deficiency of this method is that this is not necessarily the case in the bender-element measurement, as the shape of the received signal is, by definition, far more complex than the transmitted one. Nevertheless, due to its simplicity of use, it has been chosen as a complementary method in this research.

The cross-correlation function was plotted for the chosen signals of the phase-change method. Figure 12 shows the cross-correlation plots of the data from Figure 10, along with the position of the calculated group arrival times t_g from the phase-change method. It can be seen that for the signals at relevant frequencies (9, 12, 15 and 20 kHz) the peaks of the cross-correlation function are close to the positions of the group arrival times.

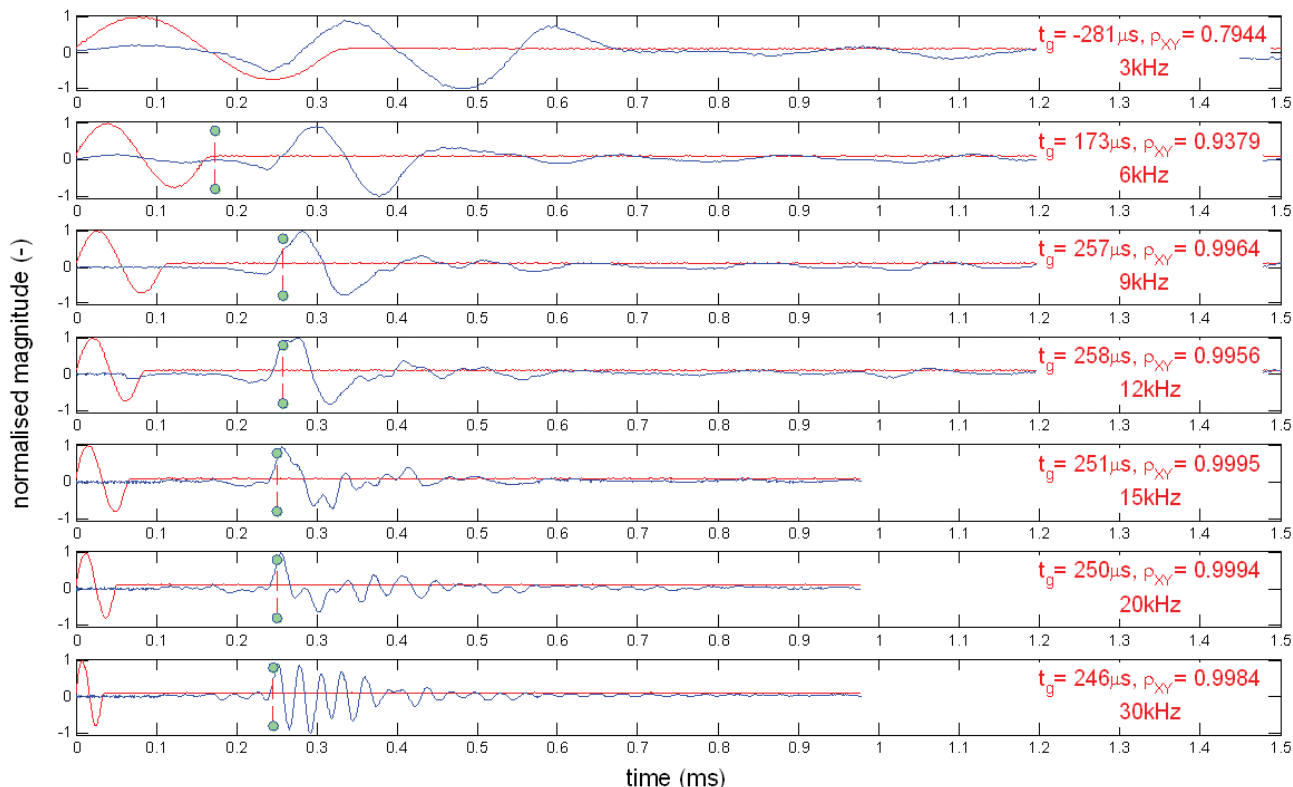


Figure 10. Input and output signals along with the positions of the calculated group arrival times t_g (sample BO-I-J at $p' = 1300$ kPa). (On the right-hand side of each plot the values of the calculated group arrival time (t_g), the correlation coefficient (ρ_{xy}) between the linear trend and the stacked phase and excitation frequency (f) of the pulse are given.)

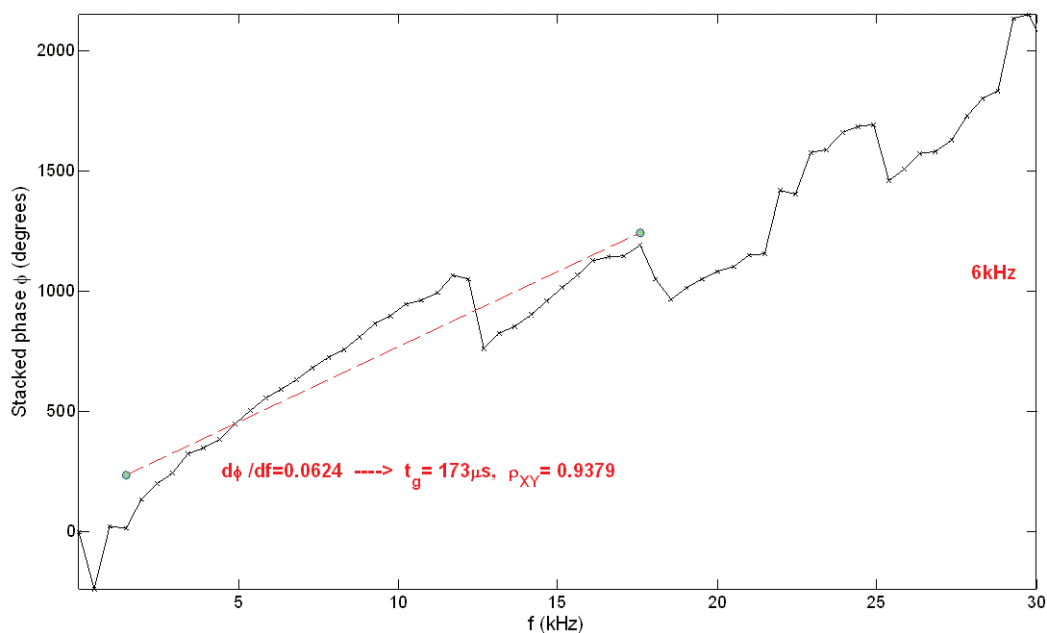


Figure 11. Stacked phase ϕ of the transfer function versus frequency f for the sample BO-I-J at $p' = 1300$ kPa, using an input sine pulse signal at 6 kHz. (The poorly chosen frequency interval covering the widest linear range is also shown, along with the value of the slope $\frac{d\phi}{df}$, the group time arrival t_g and the correlation coefficient ρ_{xy} between the data and the shown linear trend.)

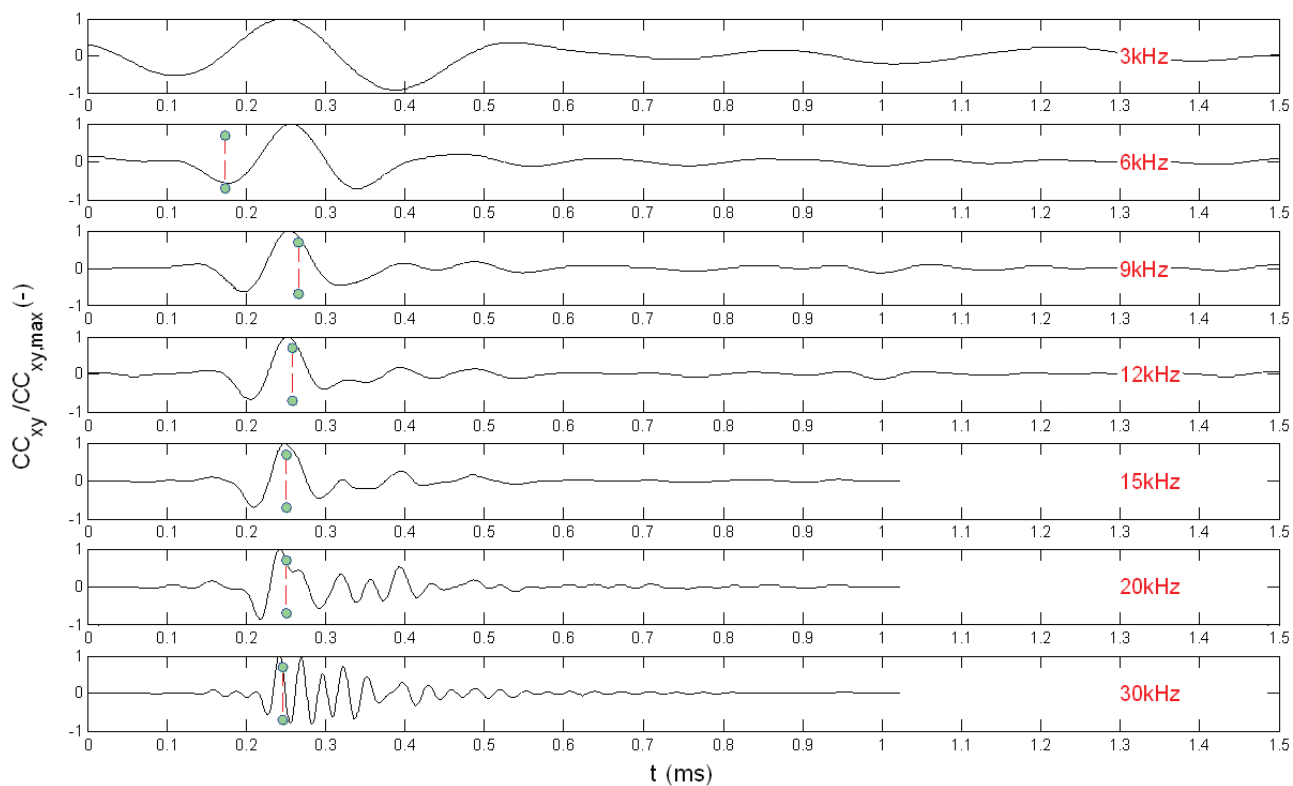


Figure 12. Normalised cross-correlation $CC_{XY} / CC_{XY,max}$ versus time for sample BO-I-J at $p' = 1300$ kPa.

The comparison of the interpretation using different techniques is presented and discussed in Section 5.

4 VARIATION OF G_0 VERSUS THE STATE OF BOŠTANJ SILTY SAND

In total, nine samples of Boštanj silty sand were prepared at different initial void ratios and isotropically compressed in triaxial apparatus. The bender-element tests were carried out with the aim to measure the variation of G_0 with the variation of density and the stress state of the sample during isotropic compression. The loading at higher stresses was employed in order to be able to reach the unique normal compression line (NCL) of the studied granular material (Coop [8]) and measure the G_0 values along it. The isotropic compression data of all the samples in the $e - \log p'$ plane are shown in Figure 13. It can be seen that by increasing the mean

effective stress p' , the isotropic compression lines start to converge towards a unique, straight, normal compression line (NCL) in the $e - \log p'$ plane. The proposed equation for the NCL is also shown on the plot. The bender element method was used to determine the values of G_0 along the isotropic compression lines and the results are shown in Figure 14. It can be seen from Figure 14 that decreasing the void ratio (e) causes the G_0 values to increase. Moreover, by increasing the stress p' the $\log G_0$ values in the $\log G_0 - \log p'$ plane tend to converge to a unique straight line, referred to as the $G_0(NCL)$ line. This line can be mathematically expressed in the form $G_0(NCL) = p_r A (p'/p_r)^n$, where the value of $A = 1459$ represents the intercept of the line and $n = 0.755$ its gradient, while p_r is a reference pressure of 1 kPa, used to make both parameters of the equation dimensionless. Similar observations were made on three other granular materials, as shown in Figure 15, i.e., Dogs Bay sand, Decomposed granite and Ham River sand by Jovičić and Coop [15].

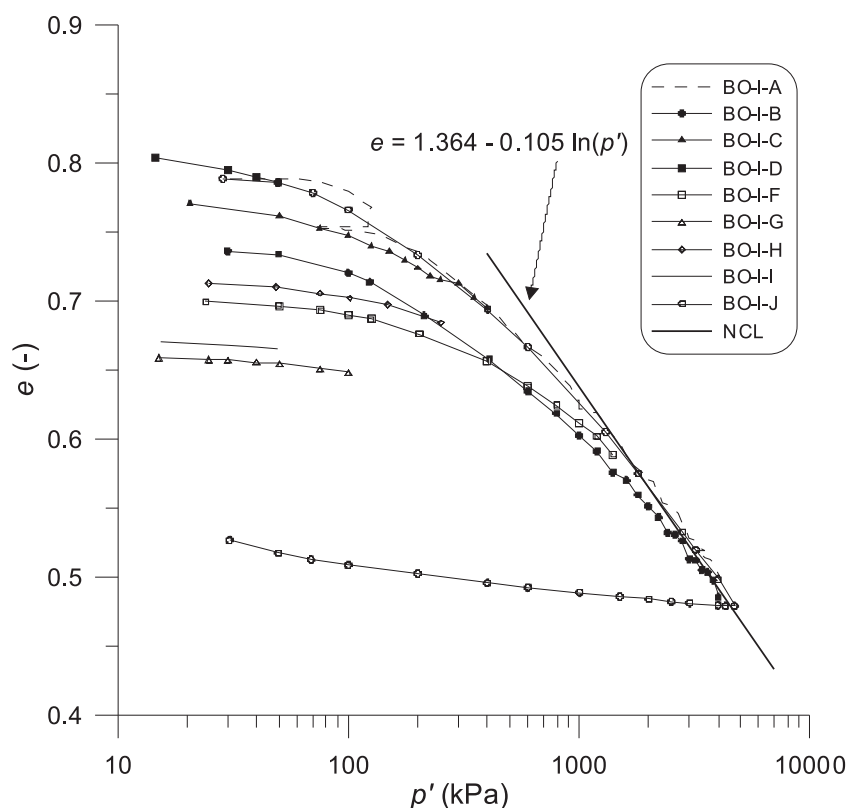


Figure 13. Isotropic compression of Boštanj silty sand in the $e - \log p'$ plane.

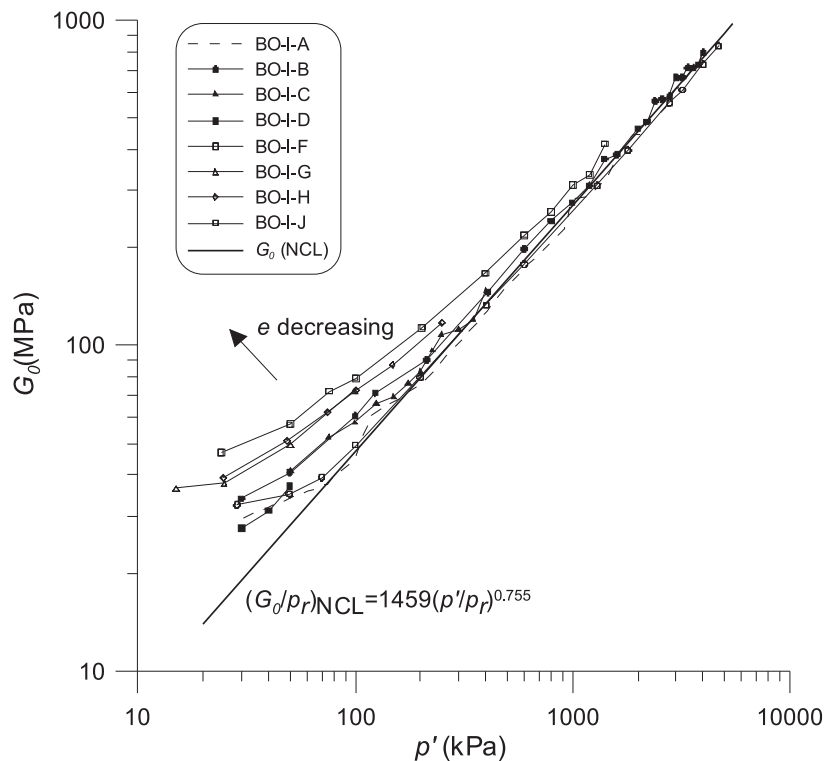


Figure 14. G_0 versus p' during isotropic compression first loading. The $G_0(NCL)$ line along with its equation is also shown on the plot. The G_0 values were calculated using the first-arrival method.

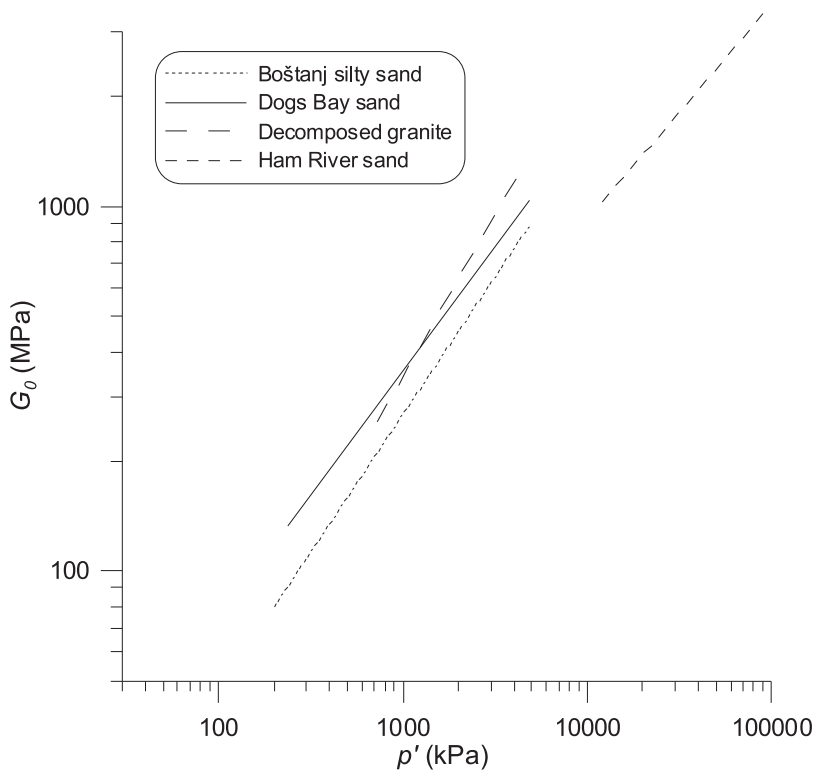


Figure 15. Comparison of G_0 values at NCL for different sands using the first-arrival method (data for Dogs bay sand, Decomposed granite and Ham River sand, after Jovičić and Coop [15]).

5 INTERPRETATION OF THE MEASUREMENTS USING DIFFERENT METHODS

The comparison of the G_0 values calculated using the first-arrival (TD), phase-change (FD) and cross-correlation (CC) methods for the two selected samples is shown in Figure 16. The sample BO-I-B was tested in the 5-MPa triaxial apparatus, while the sample BO-I-C was tested in the 0.8-MPa apparatus. It can be seen that the phase-change and cross-correlation methods give consistently lower values of G_0 compared to the first-arrival method. Moreover, the G_0 values of the phase-change and cross-correlation methods agree well with each other. Among all the tests, the differences between the first-arrival method and the other two methods are the biggest for the tests BO-I-C and BO-I-D, which suggests a system dependence of both methods, while all the other tests were performed in the 5-MPa apparatus.

If the phase-change results are plotted together, the convergence towards the linear trend at higher stresses is poorer compared to the first-arrival results (Figure 17 in

comparison with Figure 14), which is likely to indicate the higher level of inconsistency of the phase-change method compared to the first-arrival method. The same holds true for the cross-correlation method, which is known to be signal dependent.

To quantify the differences in the G_0 calculations using different methods, the relative error (E_r) in the G_0 calculation according to the three different methods is shown in Figure 18. The G_0 values derived using the first-arrival method are taken as reference values and E_r is calculated according to Equation (A.12). It can be seen that the relative errors in G_0 can be as high as 38%, which is significant. Furthermore, the relative errors for the phase-change, and also for cross-correlation method, are distinctively higher in the 0.8-MPa triaxial cell than in the 5-MPa cell. This difference in error shows the inconsistency of the phase-change and cross-correlation methods, according to the different system conditions (i.e., the different sample dimensions, the bender-element dimensions, the boundary conditions, etc.). Similar inconsistencies were also reported in the international inter-laboratory study of the ISSMGE [24], comparing different laboratories worldwide.

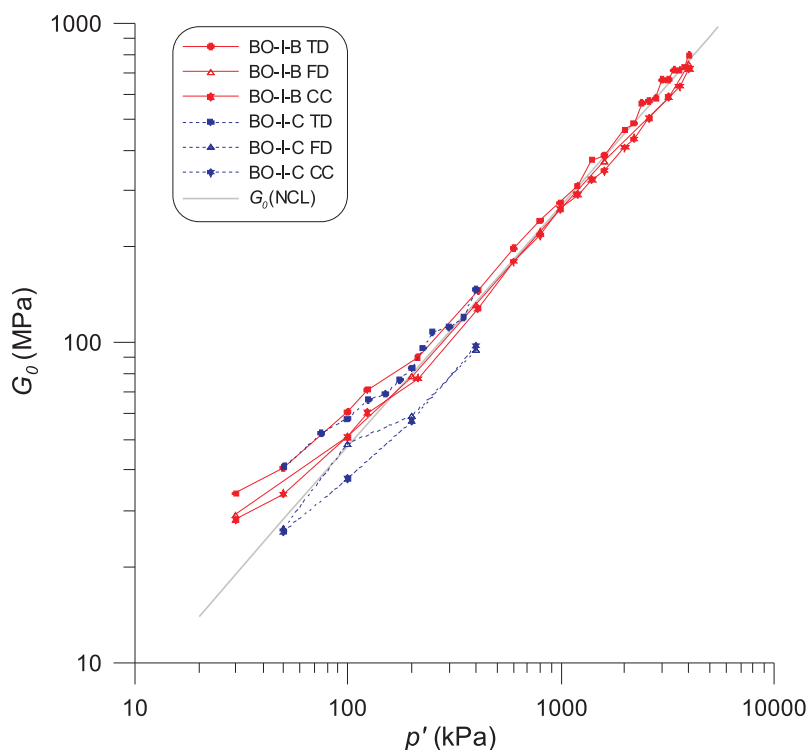


Figure 16. G_0 versus p' for samples BO-I-B and BO-I-C calculated using the first-arrival (TD), phase-change (FD) and cross-correlation (CC) methods.

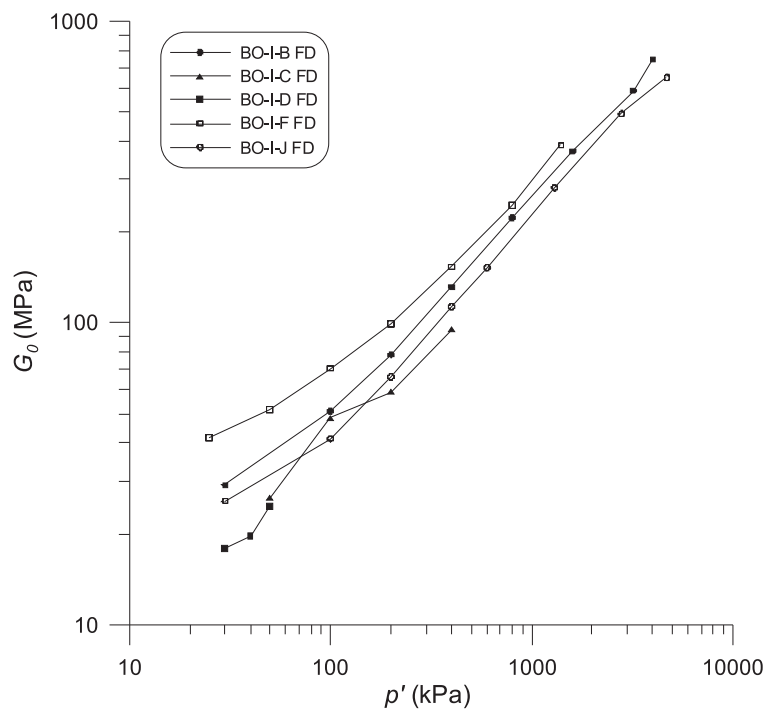


Figure 17. G_0 versus p' during isotropic compression first loading calculated using the phase-change method. The poorer convergence towards the linear trend with increasing p' can be seen according to Figure 14.

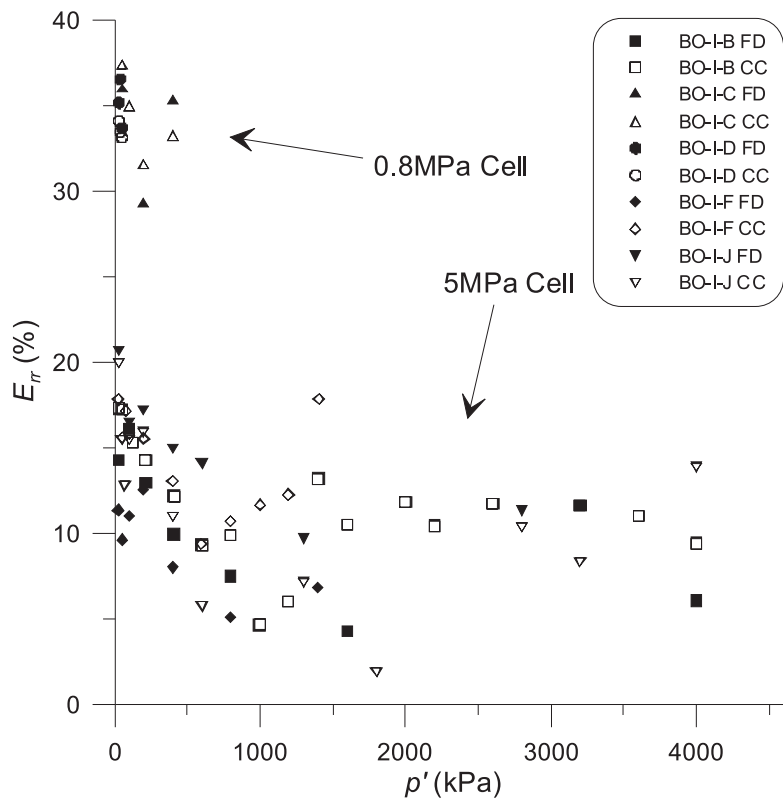


Figure 18. Relative errors E_{rr} in G_0 for the phase-change (FD) and the cross-correlation (CC) methods. The time-domain values are taken as reference values.

The values of G_0 measured by using the bender elements can be verified by employing other techniques for the shear-modulus determination, such as the resonant-column method, the shear-plates method, geophysical methods and static shear probes. All the samples of Boštanj silty sand were equipped with the local strain transducers. Therefore, a comparison between G_0 and the tangent shear stiffness of the static probes can be made. Figure 19 shows the tangent stiffness of the static shear probes from very small to large strains along with the G_0 measurements for all the samples. It can be seen that the G_0 values are higher than the tangent stiffness values at the initial stages of the tests at shear strain levels still reliably measured with static shear probes, which is in accordance with the expected material behaviour, while the G_0 is measured at lower strain levels than the tangent stiffness values at the initial stages of the tests.

6 DISCUSSION AND CONCLUSIONS

In accordance with the recommendations of the ISSMGE [24] and Fonseca et al. [12], three different methods for interpreting the G_0 values were employed in order to interpret the bender-element tests, i.e., the first arrival time, the cross-correlation and the frequency-domain method of phase change. The single-shot sine pulses were used as the driving signals for the time- and frequency-domain interpretations.

The deficiency of the frequency-domain (i.e., phase-change) method seems to be in the fact that the dispersion effects and multiple vibration modes mask the material response, which cannot be easily singled out from the phase-frequency relationship. Such techniques should probably also accommodate for the several frequency-response functions involved in the bender-

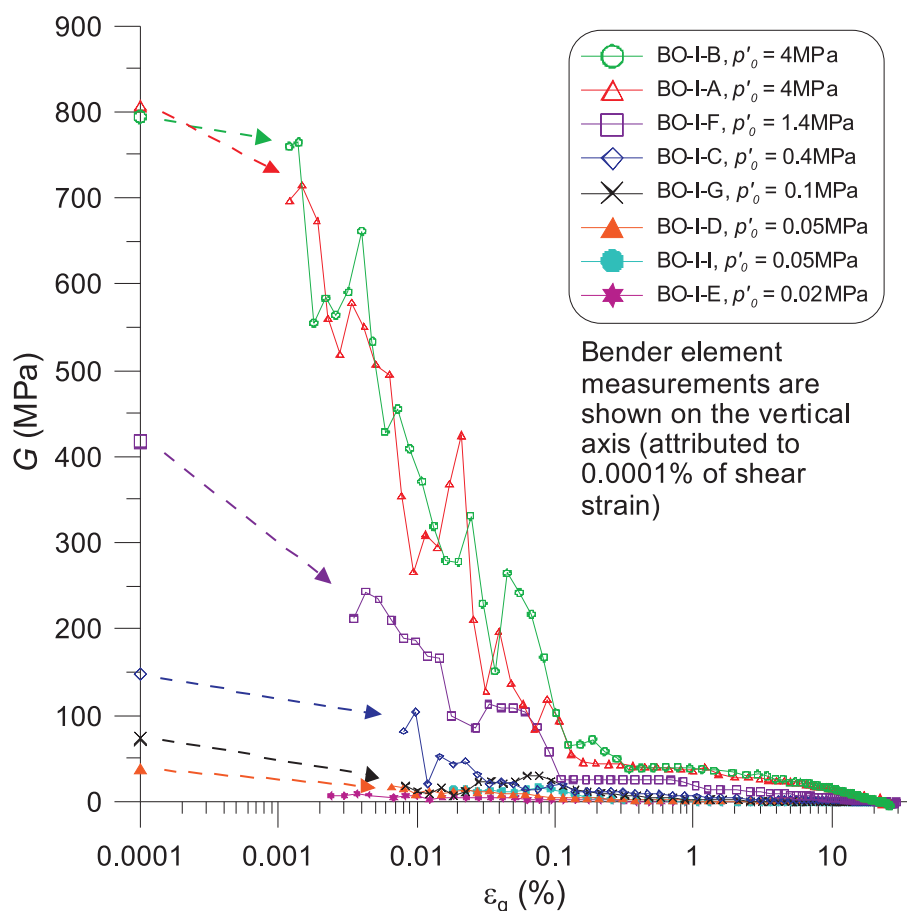


Figure 19. Dependence of the tangent shear stiffness G during the drained triaxial compression tests on the level of shear strain ε_q and the initial effective confining pressure p'_0 for Boštanj silty sand. For comparison, the values of the bender-element G_0 values are also shown in the figure for each sample.

element system to single out the frequency response function that is closer to the one of the soil (Lee & Santamarina [18]). Therefore, identifying the sharp time-arrival points in the time domain by visually inspecting many of the signals produced by pulse input sine signals at different excitation frequencies for samples of Boštanj silty sand was a more reliable approach than the one in the frequency domain.

The differences of G_0 calculated using the time and frequency domains can be very high (up to 38% of relative error), which is significant. The G_0 values calculated by the phase-change method are found to be consistently lower than the G_0 values from time domain. It seems to be a systematic difference, the reasons for which have not yet been fully understood [13,2,12]. One of the explanations is that both methods use the ready signal from the function generator as the transmitted signal, which is, in fact, not the signal that was transmitted to sample. The transmitted signal is the result of the interaction between the bender element and the soil at the time and the place of transmission and this cannot be determined without the use of a self-monitoring element (Jovičić [16]). Also, the phase-change and the cross-correlation methods are shown to be system dependent (type of signal, medium, boundary conditions, etc.) and are, as such, inconsistent.

Due to the reasons explained above, the results of the bender-element measurements were consistently interpreted using the time-domain method of the first arrival time. It was demonstrated that the samples of Boštanj silty sand converge during isotropic compression to a unique, linear, $G_0(NCL)$ line with an increasing mean effective stress p' . The comparable results and similar trends were also observed with the bender-element measurement for the three other granular materials, i.e., Dogs Bay sand, Decomposed granite and Ham River sand (Jovičić & Coop [15]). This demonstrates that in terms of the small strain stiffness, Boštanj silty sand, despite containing a relatively high percentage of non-plastic fines, follows the pattern of behaviour that is characteristic for sands in general.

APPENDIX

The shear-wave velocity is calculated according to the following relation

$$v_s = D/t_{arr}, \quad (A.1)$$

where D is the travelling distance of the wave and t_{arr} is its time arrival. The shear modulus G_0 at very small strains is calculated using the value of v_s and the bulk unit weight (ρ) as:

$$G_0 = \rho v_s^2. \quad (A.2)$$

The linear spectrum $L_x(f)$ of the signal $X(T)$ is its FFT into the complex field (e.g., Viggiani & Atkinson [23]) denoted by

$$L_x(f) = FFT[X(T)]. \quad (A.3)$$

The cross-power spectrum $G_{xy}(f)$ of the signals $X(T)$ and $Y(T)$ is

$$G_{xy}(f) = L_x(f) \cdot L_y(f)^*, \quad (A.4)$$

where $L_y(f)^*$ is a complex conjugate of the linear spectrum of $Y(T)$.

The transfer function $H(f)$ (frequency-response function) of the linear time invariable system is a vector in the complex domain. It can be written in complex polar notation [5] as:

$$H(f) = |H(f)| \exp(-j\phi(f)). \quad (A.5)$$

The absolute value $|H(f)|$ is termed as a system gain factor and the phase angle $\phi(f)$ as system phase factor. $|H(f)|$ denotes the ratio between the signal amplitudes

$$|H(f)| = \frac{|L_y(f)|}{|L_x(f)|}, \quad (A.6)$$

and the phase shift between the signals is equal to the phase factor as

$$\phi(f) = \phi_y(f) - \phi_x(f), \quad (A.7)$$

where ϕ_y and ϕ_x are the stacked phases of the signals $X(T)$ and $Y(T)$.

The phase velocity ($v_{ph}(f)$) of each frequency component can be calculated from the secant of the plot $f - \phi$ as

$$v_{ph}(f) = 2\pi D \frac{f}{\phi(f)}, \quad (A.8)$$

where D is the travelling distance of the travelling wave. The group velocity (v_g) of the wave packet from the chosen frequency interval is calculated from the slope of the tangent $\frac{df}{d\phi}$ from this frequency interval as

$$v_g = 2\pi D \frac{df}{d\phi}. \quad (A.9)$$

If the system was non-dispersive, which is not the case in real bender-element systems, the values of the phase and group velocities would be equal. Of greater practical application is the group time arrival (t_g) of the wave packet from the chosen frequency interval, defined as

$$t_g = \frac{1}{2\pi} \frac{d\phi}{df}. \quad (\text{A.10})$$

In the following, the definition of the cross-correlation function $CC_{xy}(t)$ is given. It is a measure of the degree of correlation of the two signals $X(T)$ and $Y(T)$ and is analytically defined [23] as

$$CC_{XY}(t) = \lim_{T_r \rightarrow \infty} \frac{1}{T_r} \int_{T_r} X(T)Y(T+t)dt, \quad (\text{A.11})$$

where T_r is the length of the sampled signals and t is the time shift between the signals.

The relative error E_{rr} of the G_0 calculation using the phase-change or cross-correlation methods ($G_{0,i}$) according to the G_0 value of the first-arrival method ($G_{0,FA}$) is calculated as

$$E_{rr} = \frac{G_{0,FA} - G_{0,i}}{G_{0,FA}}. \quad (\text{A.12})$$

ACKNOWLEDGMENTS

The research presented in this paper was performed at Imperial College Soil Mechanics Laboratory, London. The authors are grateful to Professor Matthew Coop at Imperial College and Doctor Giovanni Alvarado from Geotechnical Consulting Group, London (formerly a PhD student at Imperial College) for their help and support in measuring, numerical and interpretational issues. The financial support of Imperial College, the Ministry of Higher Education, Science and Technology of the Republic of Slovenia, the AdFutura scholarship fund and the Slovenian National Building and Civil Engineering Institute (ZAG Ljubljana) is gratefully acknowledged.

REFERENCES

- [1] Alvarado, G. (2007). *Influence of late cementation on the behaviour of reservoir sands*. PhD Thesis, Imperial College, University of London.
- [2] Alvarado, G., Coop, M.R. (2004). Experience of bender element measurements on a variety of materials. *Workshop on Bender Element Testing of Soils*, University College, London.
- [3] Arroyo, M., Muir Wood, D., Greening, P.D., Medina, L., Rio, J. (2006). Effects of sample size on bender-based axial G_0 measurements. *Géotechnique*, 56(1), 39-52.
- [4] Arroyo, M., Muir Wood, D., Greening, P.D. (2003). Source near-field effects and pulse tests in soil samples. *Géotechnique*, 53(3), 337-345.
- [5] Bendat, J.S., Piersol, A.G. (2000). *Random data: analysis and measurement procedures*. John Wiley & Sons.
- [6] Brignoli, E.G.M., Gotti, M., Stokoe, K.H. (1996). Measurement of shear waves in laboratory specimens by means of piezoelectric transducers. *Geotechnical Testing Journal*, 19(4), 384-397.
- [7] Brignoli, E.G.M., Gotti, M. (1992). Misura della velocità di onde elastici di taglio in laboratorio con l'impiego di trasduttori piezoelettrici. *Riv. Ital. Geotec.* 26, 1, 5-16.
- [8] Coop, M.R. (2003). On the mechanics of reconstituted and natural sands. Keynote lecture. In: Di Benedetto, H., Doanh, T., Geoffroy, H., Saueat, C. (eds.). *Deformation Characteristics of Geomaterials*. Swets and Zeitlinger, Lisse, Vol. 2, 29-58.
- [9] Cuccovillo, T., Coop, M.R. (1997). The measurement of local axial strains in triaxial tests using LVDTs. *Géotechnique*, 47, 1, 167-171.
- [10] Dyvik, R., Madshus, C. (1985). Lab measurements of G_{max} using bender elements. In: *Proc. of the ASCE Conference on Advances in the Art of Testing Soils under Cyclic Conditions*, Detroit, 186-196.
- [11] Fernandez, A.L. (2000). *Tomographic imaging the state of stress*. PhD Thesis, Civil Engineering, Georgia Institute of Technology, Atlanta.
- [12] Fonseca, A.V., Ferreira, C., Fahey, M. (2009). A framework interpreting bender element tests, combining time-domain and frequency-domain methods. *Geotech. Testing J.*, 32, 2, 91-107.
- [13] Greening, P.D., Nash, D.F.T. (2004). Frequency domain determination of G_0 using bender elements. *Geotechnical Testing Journal*, 27, 3, 288-294.
- [14] Jardine, R.J., Shibuya, S. (2005). TC29 workshop: Laboratory tests. Report. *Proc. of the 16th International Conference on Soil Mechanics and Geotechnical Engineering*, Osaka 5, 3275-3276.
- [15] Jovičić, V., Coop, M.R. (1997). Stiffness of coarse-grained soils at small strains. *Géotechnique*, 47(3), 545-561.
- [16] Jovičić, V. (1997). *The measurement and interpretation of small strain stiffness of soils*. PhD thesis, The City University, London.

- [17] Jovičić, V., Coop, M.R., Simić, M. (1996). Objective criteria for determining G_{max} from bender element tests. *Géotechnique*, 46(2), 357-362.
- [18] Lee, J.-S., Santamarina, J.C. (2005). Bender elements: performance and signal interpretation. *Journal of Geotechnical and Geoenvironmental Engineering*, 131, 9, 1063-1070.
- [19] Lenart, S. (2008). The response of saturated soils to a dynamic load. *Acta Geotechnica Slovenica*, 5, 1, 37-49.
- [20] Rio, J.F.M.E. (2006). *Advances in laboratory geophysics using bender elements*. PhD thesis, University College, London.
- [21] Sánchez Salinero, I., Roesset, J.M., Stokoe, K.H. (1986). Analytical studies of body wave propagation and attenuation. Geotechnical Engineering Report No. GR86-15, Civil Engineering Department, University of Texas at Austin.
- [22] Shirley, D.J., Hampton, L.D. (1977). Shear wave measurements in laboratory sediments. *J Acoust Soc Am*, 63(2), 607-613.
- [23] Viggiani, G., Atkinson, J.H. (1995). Interpretation of bender element tests. *Géotechnique*, 45(1), 149-154.
- [24] Yamashita, S., Fujiwara, T., Kawaguchi, T., Mikami, T., Nakata, Y., Shibuya, S. (2007). International parallel test on the measurement of G_{max} using bender elements. Organized by Technical Committee 29 of the ISSMGE (<http://www.jiban.or.jp/e/tc29>).

GEOMEHANSKO OBNAŠANJE STISLJIVIH MORSKIH MELJEV POD OBREŽNIM VALOLOMOM IZ GRUŠČNATEGA NASIPA

LIEN-KWEI CHIEN, TSUNG-SHEN FENG IN TSUNG-CHING CHEN

o avtorjih

Lien-kwei Chien
National Taiwan Ocean University,
Department of Harbor and River Engineering
No. 2 Pei-Ninig Road, Keelung 202, Tajska
E-pošta: lkchien@mail.ntou.edu.tw

Tsung-shen Feng
National Taiwan Ocean University,
Department of Harbor and River Engineering
No. 2 Pei-Ninig Road, Keelung 202, Tajska
E-pošta: D91520004@mail.ntou.edu.tw

Tsung-ching Chen
National Taiwan Ocean University,
Department of Harbor and River Engineering
No. 2 Pei-Ninig Road, Keelung 202, Tajska
E-pošta: M93520078@mail.ntou.edu.tw

izvleček

V pričujoči študiji so obravnavani stisljivi morski melji pod obrežnim valolomom iz gruščnatega nasipa v Ma-Zu-ju na zahodu Tajvana. Preizkušanci so bili pripravljene z novo metodo, s ponovnim preoblikovanjem vzorcev pri suhi gostoti in konsolidacijskih tlakih. Za določitev pornih vodnih tlakov in parametrov strižne trdnosti so bili izvedeni triaksialni preizkusi strižne trdnosti. Rezultati teh preizkusov so pokazali, da porni vodni tlak postopoma raste in je blizu kritičnih vrednosti, ko raste osna specifična deformacija. Razen tega sta bili, pri izotropni in K_0 konsolidaciji, obe vrednosti c in c' stisljivih morskih meljev enaki 0 kPa, kar pomeni da melji nimajo nobene strižne trdnosti, torej se obnašajo kot tekočina pod valolomom iz gruščnatega nasipa. Na osnovi linearne elastičnosti in eno dimenzionalne teorije konsolidacije so bili v programskem orodju SIGMA/W preračunani posedki in preverjena stabilnost. Rezultati teh analiz so pokazali, da so stisljivi morski melji pri valolomu sprožili deformacije, ki so se zelo povečale z obtežbo zaradi izdelave gruščnatega nasipa. Slike in rezultati kažejo zveze za vrednotenje stabilnosti meljastih naplavin pod valolomom iz gruščnatega nasipa. Rezultati so uporabni pri mehaniki morskih meljev in stabilnostnih analizah za planiranje, projektiranje in podobne raziskave v inženirstvu obrežij.

ključne besede

geomehansko obnašanje, stisljivi morski melji, valolomom iz gruščnatega nasipa, posedek, numerični model

THE GEO-MECHANICS BEHAVIOR OF SOFT MARINE SILTS UNDER A NEARSHORE RUBBLE-MOUND BREAKWATER

LIEN-KWEI CHIEN, TSUNG-SHEN FENG and TSUNG-CHING CHEN

About the authors

Lien-kwei Chien
National Taiwan Ocean University,
Department of Harbor and River Engineering
No. 2 Pei-Ninig Road, Keelung 202, Taiwan
E-mail: lkchien@mail.ntou.edu.tw

Tsung-shen Feng
National Taiwan Ocean University,
Department of Harbor and River Engineering
No. 2 Pei-Ninig Road, Keelung 202, Taiwan
E-mail: D91520004@mail.ntou.edu.tw

Tsung-ching Chen
National Taiwan Ocean University,
Department of Harbor and River Engineering
No. 2 Pei-Ninig Road, Keelung 202, Taiwan
E-mail: M93520078@mail.ntou.edu.tw

Abstract

In this study, the soft marine silts under a rubble-mound breakwater in Ma-Zu of west Taiwan are adopted as a test sample. The specimens were prepared by a new, remolded method at dry density and consolidated stresses. Tri-axial shear-strength tests were performed to evaluate the pore-water pressure and the shear strength. The test results show that the pore-water pressure increases gradually and is close to the critical values as the axial strain increases. In addition, under isotropic and K_0 consolidation, both the c and c' of the soft marine silts were 0 kPa, which means that the silts do not have any shear resistance, just like fluid under a rubble-mound breakwater. Based on the linear-elasticity and the one-dimensional consolidation theory, the model of the settlement and stability was evaluated in SIGMA/W. The results show that the soft marine silts at the breakwater induced a displacement, greatly increasing with the filling rubble-mound loading. The figures and results can be referenced for a stability evaluation of the silt soil deposits under the rubble-mound breakwater. The results are useful for marine silts mechanics and a stability analysis for the planning, design, and related research on near-shore engineering.

Keywords

geo-mechanics behavior, soft marine silt, rubble-mound breakwater, settlement, numerical simulation model

1 INTRODUCTION

In 1995, the geo-structure of the rubble-mound breakwater settled gradually during the construction of Beigan in Ma-Zu. The silt layer at the front section of the rubble-mound breakwater had heaved. When the breakwater at the Fuaao Commercial Port of Nangan, Matzu was expanded in 2002, serious settlement and lateral displacement appeared during the construction. Meanwhile, marine silts caused the foundation settlement of near-shore structures due to the inferior nature of the works, and the settlement quantity is the variable that changes with time, due to unpredictable factors such as storm waves, which are the main reason for the cause of disasters to the shore and harbor engineering (Chien et al., 2007).

In 2005, the breakwater in the north dock named Bai-Sah in Ma-Zu County was extended. The actual amounts of mound were different from the original design. As a result, the extended harbor geo-structure stopped working properly.

Chen (2004) studied the topic of a mound breakwater by physical testing, micro-fabric analysis and mechanics properties, and evaluated the possible factors and stable mechanism. Chien et al. (2005) studied an improved model using the mixing method. Furthermore, the bearing capacity was promoted by using cement-mixed soft silt clay, which also increased the shear strength of the soft clay. Mayne et al. (1990) studied the specimen stress and the corresponding model of the field under different structural loadings.

In order to further discuss the disasters factor caused by marine silts, the ongoing expansion of the breakwaters at the Fuaao Port of Ma-Zu was the research area in this study. A static experiment and a numerical analysis were performed to evaluate the factors causing the breakage

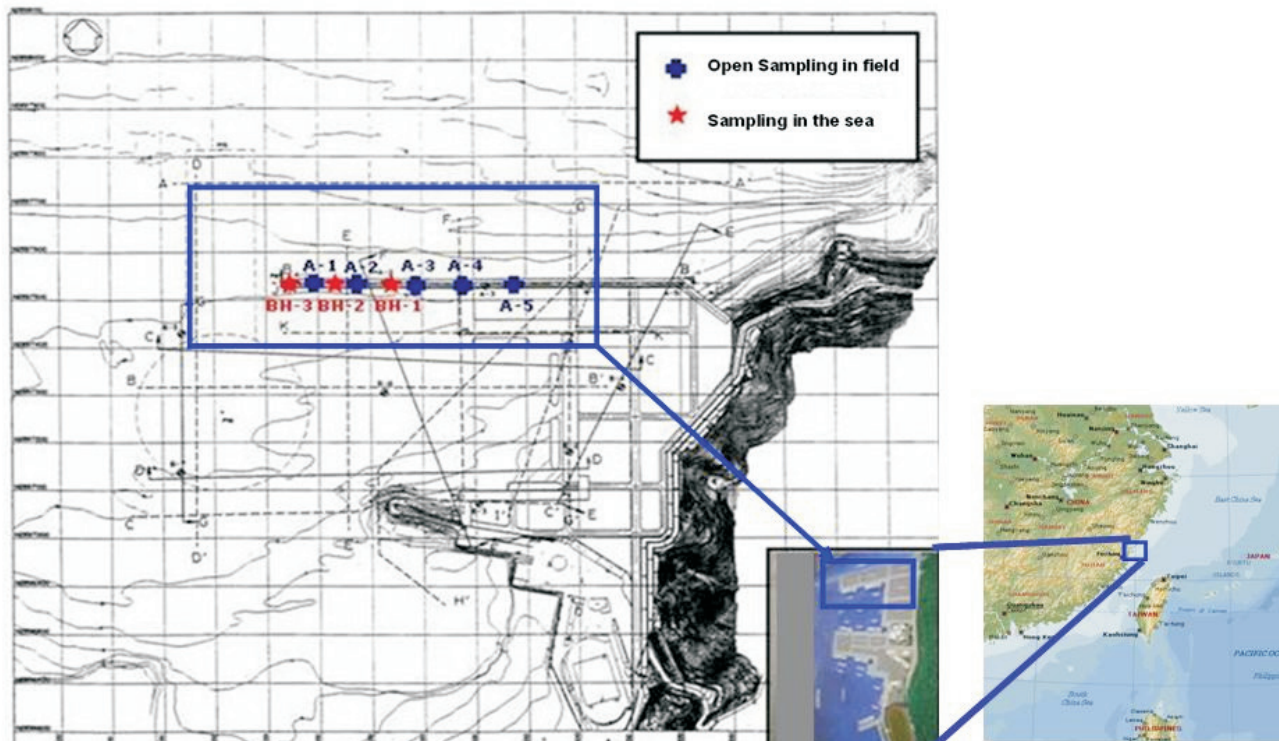


Figure 1. Locations of borings and soil sampling in the Ma-Zu extended breakwater.

of the rubble-mound breakwaters. The figures and the results can be referenced for the stability evaluation of silt soil deposits under the rubble-mound breakwater.

1.1 ANALYSIS OF RESEARCH AREA

Based on the near-shore exploration work, the locations of the borings and the soil sampling in Ma-Zu County are shown in Fig.1. From the near-shore exploration data, most of the mean SPT-N values of the profile below 12 m of the seabed were near 1, and a few of them were 7. The relationship between the SPT-N value and the depth of the exploration at the rubble-mound breakwaters are shown in Fig. 2.

1.2 BASIC PHYSICAL PROPERTIES OF THE SOIL

The liquid limit (LL) of the seabed soils at five different locations ranged from 42% to 47%, the plastic limit (PL) from 26% to 31%, and the plasticity index (PI) from 12% to 20%, based on the results of the Atterberg limit tests.

According to x-ray diffraction of the soft marine silts in Fuao, Matzu and the possible elements judged by EDS, the main chemical compositions of the soft marine

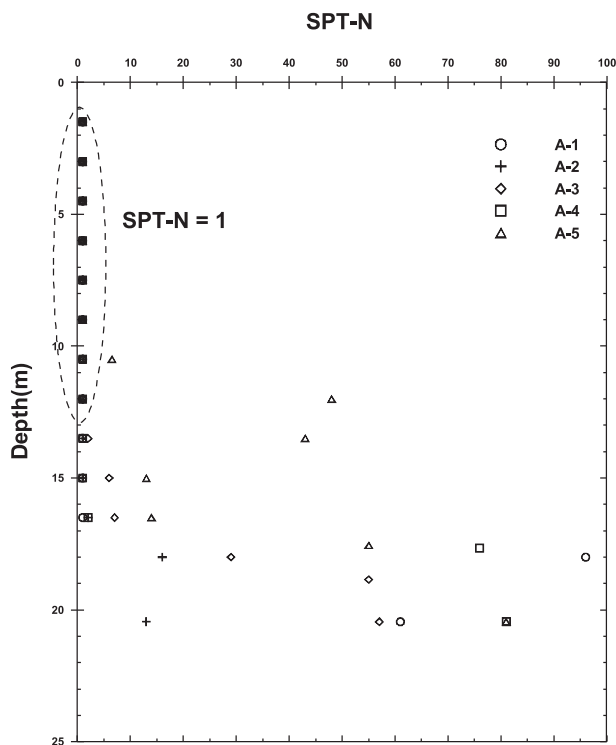


Figure 2. Relationship between the SPT-N value and the depth below the rubble-mound breakwater.

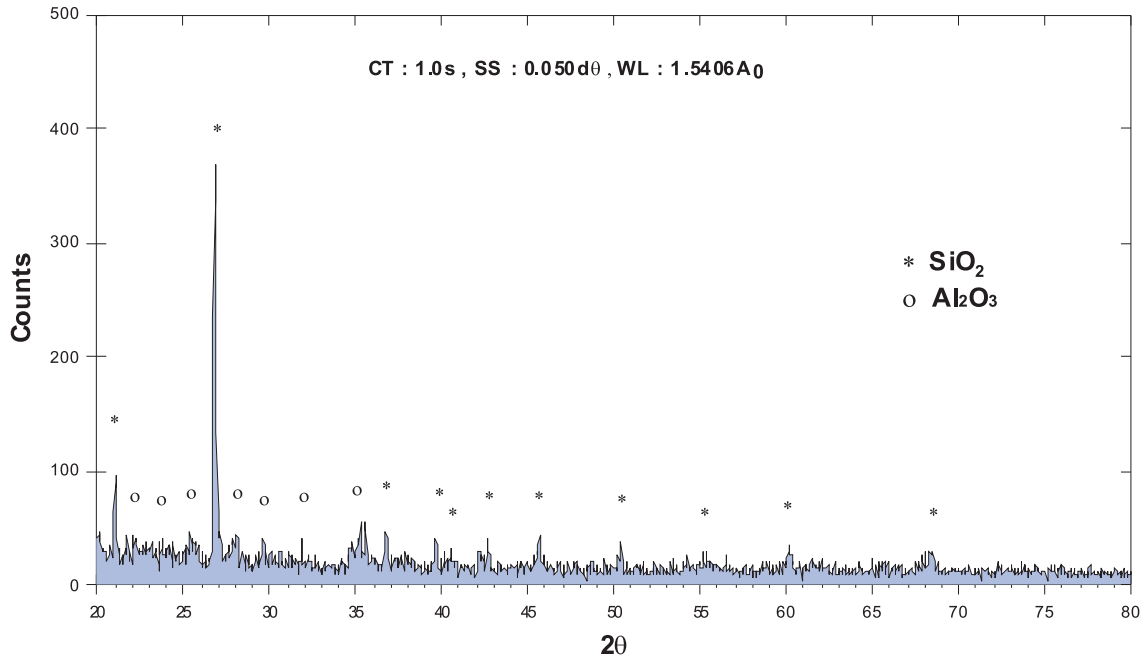


Figure 3. X-ray diffraction of marine soft silts (S-3).

silts are SiO_2 (78.1%) and Al_2O_3 (9.1%). The minor components are K_2O (4.3%), MgO (2.6%), Fe_2O_3 (2.2%), FeO (2.1%), Na_2O (1.2%), and CaO (0.4%). The results of the x-ray diffraction test are also shown in Fig. 3. The specimens were judged as weathered deposits, on the basis of the work of Wright (1981).

The particle-size-distribution curves are plotted for seabed soils taken from five locations (see Fig. 4). According to the results, the approximate contents were gravel and sand (2%), silt (45%), and clay (53%).

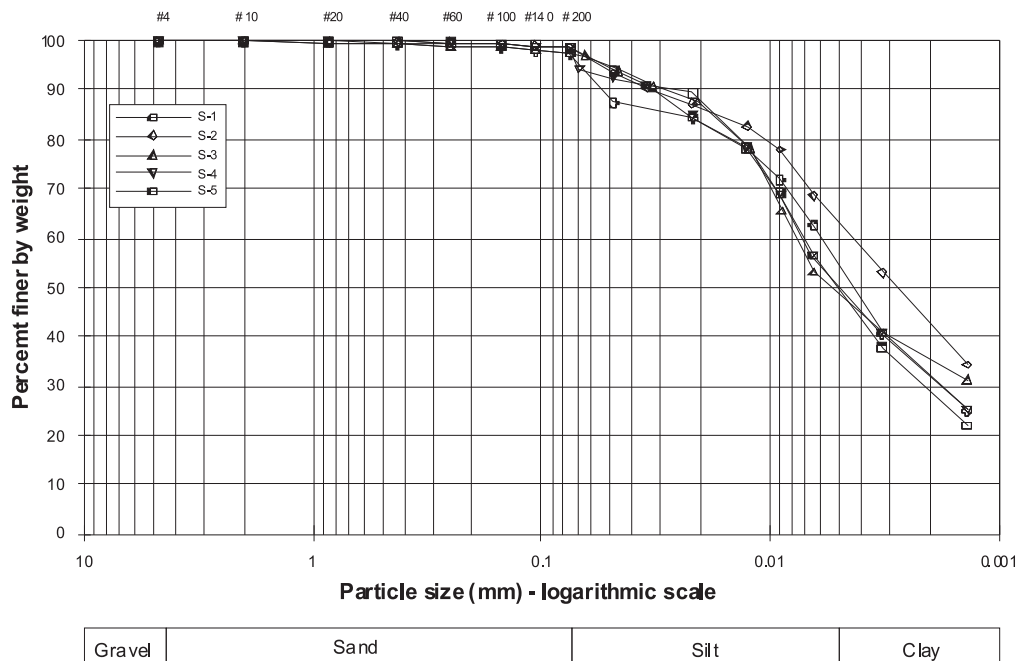


Figure 4. Particle-size-distribution curve of the soils in this experiment.

2 METHODOLOGY

A series of experiments was performed in this study, including one-dimensional consolidation and tri-axial compression tests. In order to understand the soil's basic properties, soft marine soils were prepared by a new method according to the saturated clay density, depending on the water content.

In addition, it was necessary to comprehensively analyze the soil-bearing capacity and the stability related to the slip and breakage of the foundation. The limit equilibrium method was applied to evaluate the stability of the soft ground foundation. The critical slip surface and the corresponding safety factor of the soil foundation and the relevant stress and strain of the interior slip surface can be found from the critical slip surface. The safety factor could also be found by analyzing the possible breakage mechanism.

The study analyzed the in-situ data related to stratum drilling and steel-pipe pilings. As well as the geological sampling, in-situ and laboratory experiment analysis, the density and compressibility of the soil at the soft ground were obtained from these results. The breakage of the soil layer was caused by the loading and the possible amount of settlement was evaluated by a suitable numerical model developed for the prediction of the settlement stability of soft marine ground. The results are very useful as a reference for the marine silts' stability for the planning and design of near-shore engineering.

2.1 TESTING ITEMS

The shear strength of the soft silty clay was obtained from the tri-axial test. Moreover, the specimen was prepared according to the in-situ density. Because the remolded specimen of lower unit weight was too soft, the specimen could not be set up for the tri-axial test. Therefore, a new remolding method was developed in this study. The test's controlled conditions and sets are shown in Table 1.

Table 1. Testing conditions and sets.

Test items	Dry density γ_d (t/m ³)	Consolidation Stress (kPa)	Axial pressure velocity (kPa/min)
CIU	1.00, 1.05 1.10, 1.15	15, 20, 30, 40, 45	list the axial stress velocity recommended by Lambe (1951)
CK ₀ U	1.00, 1.05 1.10, 1.15	30, 60, 90	0.5
Torvane shear test	0.88~1.04	—	—

2.2 TESTING METHODS FOR THE REMOLDED SPECIMENS

It is difficult to control the degree of saturation by using the moist temping method on marine silts. However, the shear strength was decreased with the water-content increase by applying back water pressure to the specimen in tri-axial space. The purposes of the remolded method for producing a saturated specimen were twofold: one is that the behavior of the saturated specimen was more easily controlled than the unsaturated one, and the other is that the shear strengths of the soft marine silts on the seabed were simulated.

In order to remold the very soft specimens, a new remolding method was developed in this study. The specimens were prepared using the constant volume method with dried silt clay and water contents ranging from 1.0 to 2.0%. In the specimen remolded process, a soil water content of about 200% was adopted in the test. The specimens were mixed for about 5–10 minutes at low velocity in a mixer until they became like a fluid. The soils were infiltrated into the remolded specimen instruments (7.0 cm in diameter and 20.0 cm in height) that connect with vacuum pressure. The sedimentation behavior was induced rapidly. The stresses at different steps were applied to remold the specimen gradually to reach the in-situ density, when the sedimentation stops. The remolded specimen-preparation steps are presented in Figs. 5 (a)–(d).

The C.K.C. Automatic Triaxial Test System was applied in this study, as shown in Fig.6. The test system has great advantages in stress, strain and stress path control (Chien, 2002). According to whether it is stress controlled or strain controlled, the air pressure and oil pressure can be adopted for the pressure system in the experiment. All the experimental procedures are performed through a human-computer interface to provide an easy and convenient operating environment.

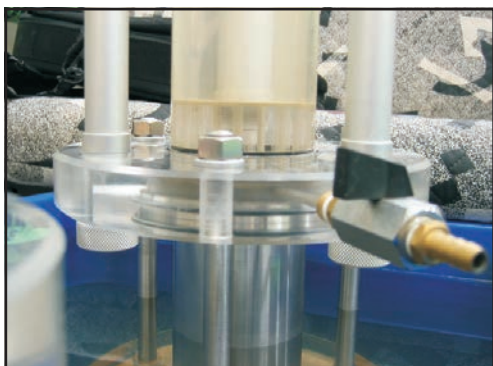
As for the normal consolidated clay, the failure envelopes were calculated from the strength parameters without conducting a consolidation and drainage test. Therefore, the undrained shear strength according to half of the maximum axial differential stress $(\sigma_1 - \sigma_3)_{\max}$ could be determined. When the axial strain exceeded 15%, but did not reach the maximum axial differential stress, the undrained shear strength can be defined according to 15% of the axial differential stress. Chien (2002) studied the effect of the fines content on the liquefaction strength by using the moist temping method at different relative densities and fine contents.



(a) The vacuity before sedimentation



(b) The specimen sedimentation



(c) Applying the steps loading



(d) Reaching the design density

Figure 5. The marine clay remold, specimen-preparation steps.

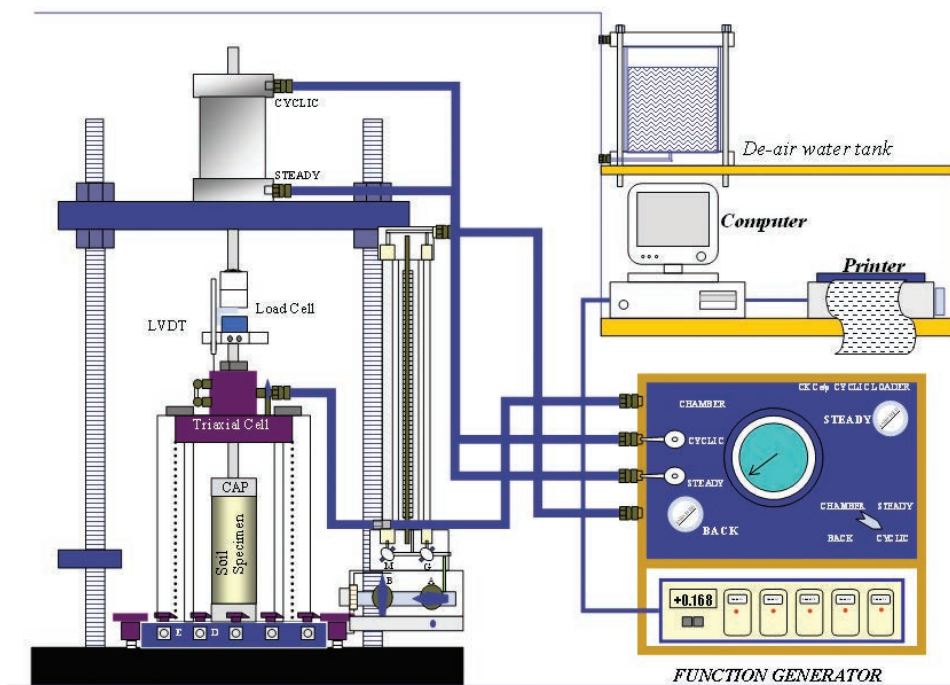


Figure 6. Sketch of the tri-axial test system.

The computer software SIGMA/W was applied to analyze the stress-strain conditions in the silt deposits, induced by the construction of the rubble breakwater structure. In order to evaluate the influence of long-term effects and excessive pore-water pressure on soft marine silts, the settlement caused by the breakwater at the Fuao Port of Ma-Zu was analyzed through a consolidation analysis and SEEP/W. The real-time consolidation and settlement caused by the rubble-mound breakwaters are predicted.

3 EXPERIMENTAL ANALYSIS AND RESULTS

3.1 DENSITY CHANGE AFTER ISOTROPIC AND K_0 CONSOLIDATION

There were four kinds of density soils selected with different initial densities for the isotropic and K_0 consolidation experiments in this study. The changes of the mean dry density (γ_d) can be obtained through different consolidation stresses, and the relationships are shown in Fig.7 and Fig. 8.

During the 45-kPa confining-pressure isotropic-consolidation process, the soil's dry density changed from an initial value of 1.10 t/m^3 to a final value of 1.22 t/m^3 . This was an increase of 10.85%. Under the K_0 consolidation with the axial direction consolidation pressure ranging between 30 and 90 kPa, the soil's dry density increased from 1.7 to 13.4% when the initial dry

density was 1.15 t/m^3 and from 1.9 to 14.0% when the initial dry density was 1.10 t/m^3 .

The increase in the dry density was more under the isotropic consolidation (4.6 to 11.5%) than under the K_0 consolidation (1.7 to 6.4%), when the consolidation stress was equal to 30 kPa. The reason for this result was that the axial stress applied during the K_0 consolidation did not promote consolidation in the radial direction.

3.2 PORE-WATER PRESSURE INDUCED UNDER ISOTROPIC AND K_0 CONSOLIDATION

According to the isotropic and K_0 consolidation under undrained conditions, the relationship between the induced excess pore-water pressure (Δu) and the strain (ϵ) is shown in Fig. 9 and Fig. 10. The figures illustrate that the initial value increased gradually, and the excessive pore-water pressure increased and approached to a positive critical value as the strain increased. This phenomenon was consistent with the definition of specimen breakage by the critical state theory: the critical state was reached when the soils deformed under stress loading.

In order to further understand the induced pore-water pressure at rest, this study also discussed the relationship between the pore-water pressure ratio ($(u/\sigma'_{nc})_{\max}$) and the strain (ϵ), where σ'_{nc} is defined as the mean consolidation stress:

$$\sigma'_{nc} = \frac{1}{3}(\sigma'_1 + \sigma'_2 + \sigma'_3) \quad (1)$$

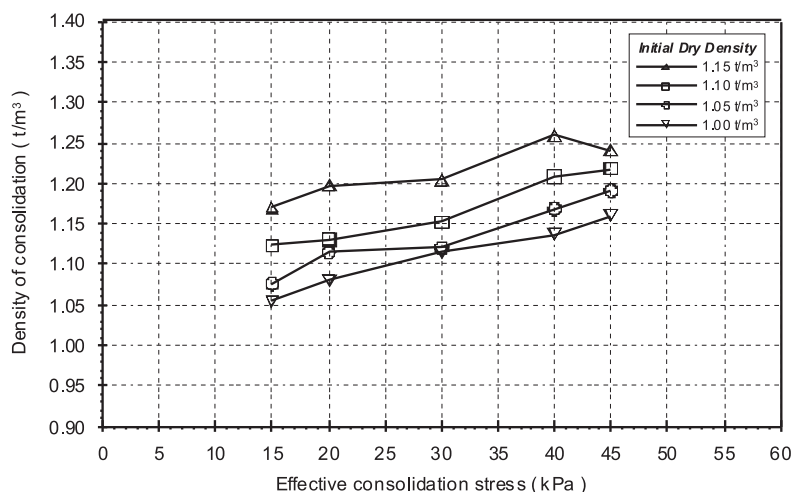


Figure 7. Dry density changes after isotropic consolidation.

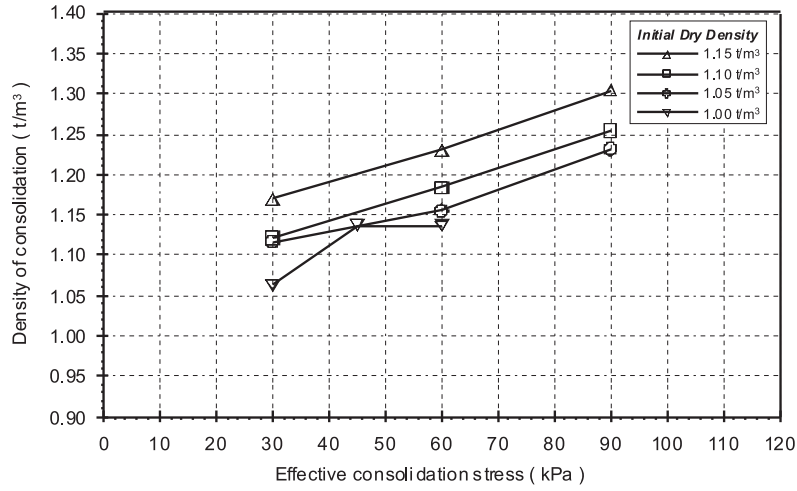


Figure 8. Dry density change after K_0 consolidation.

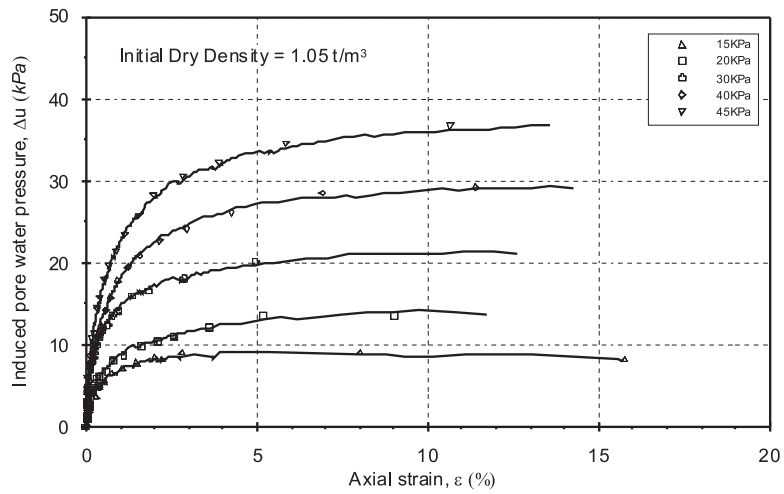


Figure 9. Relationship between Δu and ϵ curve for isotropic consolidation under undrained conditions.

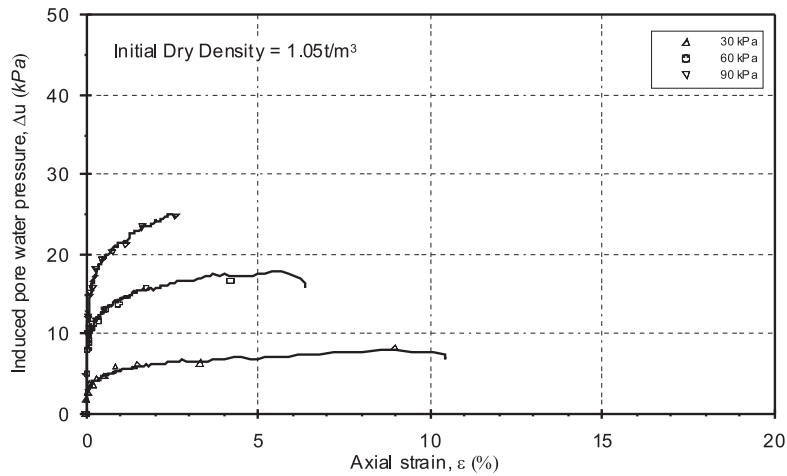


Figure 10. Relationship between Δu and ϵ curve for K_0 consolidation under undrained conditions.

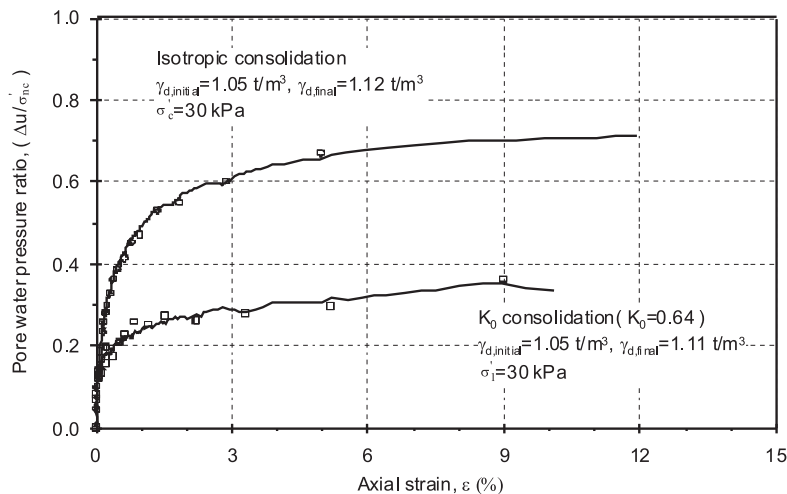


Figure 11. Comparison of the pore-water pressure model for isotropic and K_0 under undrained conditions.

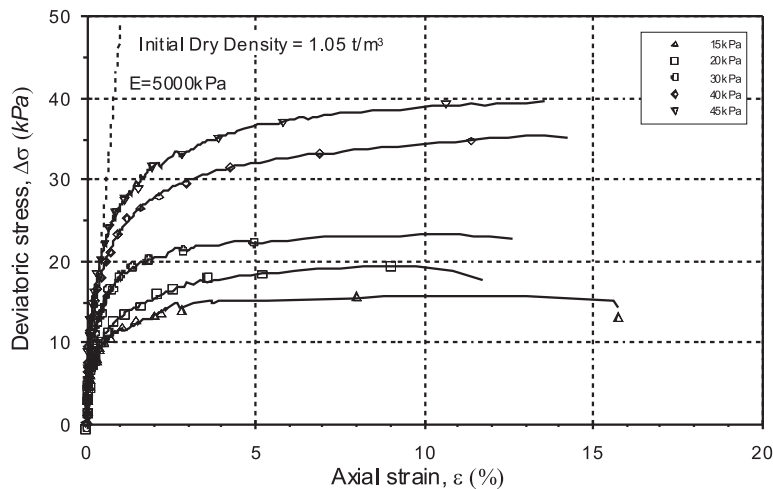


Figure 12. Relationship of $\Delta\sigma - \varepsilon$ for isotropic consolidation under undrained conditions.

The comparison of the pore-water pressure between the isotropic and K_0 consolidation processes is made in Fig. 11. The effective stress decreased gradually with the axial strain increased under static loading. However, the pore-water pressure increased more slowly during the K_0 consolidation process than during the isotropic consolidation process.

3.3 ISOTROPIC CONSOLIDATION TEST RESULTS

Fig. 12 presents the relationship between the deviatoric stress and the axial strain under isotropic with undrained conditions. For the results of the tri-axial compression testing for marine silts, the deviatoric stress increases as the confining pressure increases. Furthermore, the axial strain was plastic destruction, which,

analyzed from the relationship, has no peak strength between the stress and strain.

The results of the soft marine silts experiment illustrated the total stress and effective stress path. Under the different isotropic consolidation stresses, the final stress path and the failure lines approached consistency. Furthermore, all the failure lines passed through the original point. The relationship between the different initial dry densities and the shear strength parameters is shown in Table 2.

As for the total stress strength (short term), the parameters of the effective stress strength (long term) were smaller, as shown in Fig. 13 and Fig. 14. The parameter ϕ is approximately half of the parameter ϕ' . This is consistent with the results on the consolidated clay soils reported by Holtz and Kovacs (1981).

Table 2. Shear strength parameters for soils that underwent isotropic consolidation.

Dry density (t/m ³)	c (kPa)	φ (°)	c' (kPa)	φ' (°)
1.15	0	20.37	0	43.26
1.10	0	17.21	0	35.87
1.05	0	14.73	0	25.38
1.00	0	15.36	0	30.01

3.4 K₀ CONSOLIDATION EXPERIMENT RESULTS

Due to the intrinsic anisotropy produced by the particle arrangement considered in the traditional CIU test the

anisotropy produced by the K_0 consolidation ($K_0 \neq 1$) cannot be responded. Furthermore, anisotropic consolidation may affect the evaluation of the shear parameters related to the soft marine silts (Mayne, 1985). The basic mechanical behavior under K_0 consolidation is discussed below.

The experimental results (total stress and effective stress path plots) are shown for the soft marine soil in Figures 15 and 16. Under the different K_0 consolidation stresses, the initial value of the stress path lay below the state of the K_0 consolidation. Furthermore, all the failure lines passed through the coordinate origin. The relationship between the different initial dry densities and the shear strength parameters are shown in Table 3.

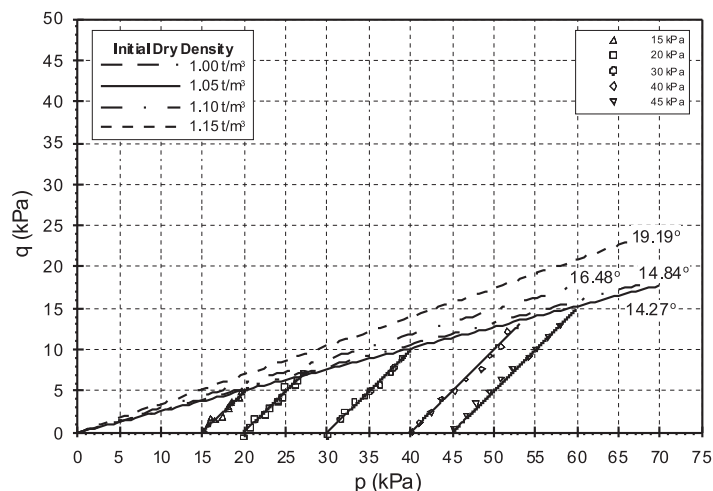


Figure 13. $p - q$ diagram for soils that underwent isotropic consolidation.

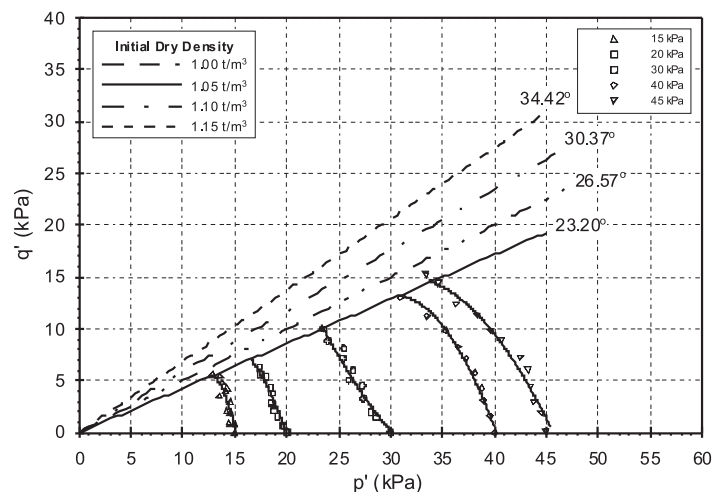


Figure 14. $p' - q'$ diagram for soils that underwent isotropic consolidation.

Table 3. Shear strength parameters for soils that underwent K_0 consolidation.

Initial dry density (t/m^3)	c (kPa)	ϕ ($^\circ$)	c' (kPa)	ϕ' ($^\circ$)
1.15	0	23.58	0	34.06
1.10	0	21.71	0	30.01
1.05	0	16.26	0	23.58
1.00	0	20.49	0	26.75

According to Skempton and Sowa (1963), the shear strength of the clay can be correlated to the water content. Figure 17 presents the shear strength vs. the water content relationships for various tests performed in the present study. The following formulas describe the relationships mathematically:

$$\text{Torvane: } Su = 0.065\omega + 6.2 \quad (2)$$

$$\text{SUU: } Su = 0.325\omega + 25.8 \quad (3)$$

$$\text{CIU: } Su = 1.02\omega + 64.55 \quad (4)$$

$$\text{CK}_0\text{U: } Su = 1.28\omega + 79.68 \quad (5)$$

Where

Su : shear strength under undrained conditions (kPa)

ω : water content (%)

The marine silts were classified as extremely soft soils, based on the shear-strength results and ASTM D1586. It was also found that the shear strengths obtained from various tests were ranked as $CIU > SUU > \text{Torvane}$. The same ranking of shear strengths was observed in a separate study (Lin, 1988). This outcome indicates that the undrained shear strength was high for the CIU soils, since the specimens consolidated completely during the CIU test procedure. However, it was apparent that the undrained shear strengths were lower for the SUU soils, since the effective stress was zero.

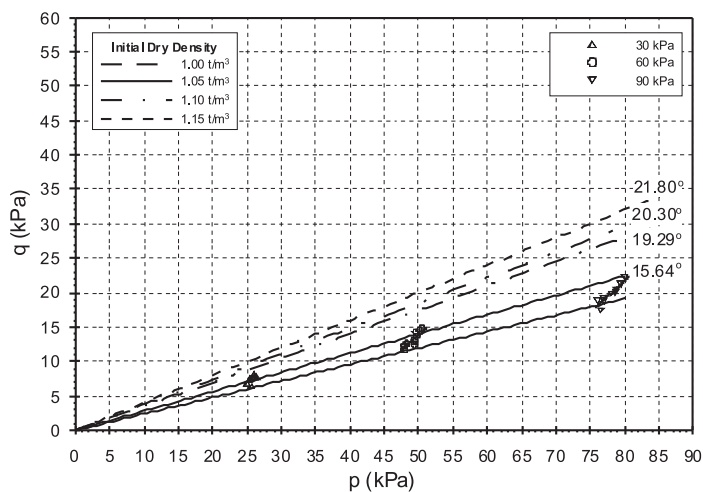


Figure 15. $p - q$ diagram for soils that underwent K_0 consolidation.

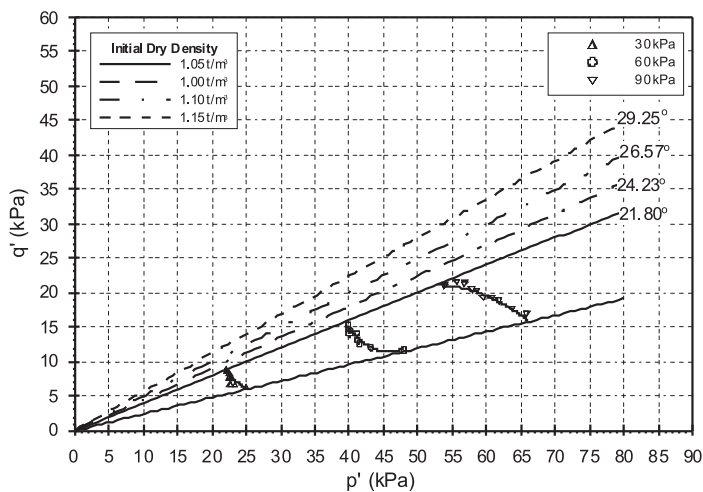


Figure 16. $p' - q'$ diagram for soils that underwent K_0 consolidation.

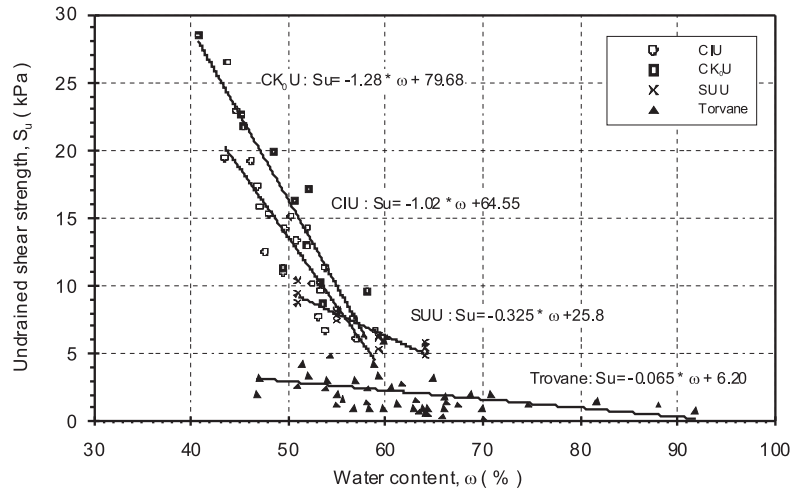


Figure 17. Undrained shear strengths resulting from different test methods.

4 NUMERICAL SIMULATION ANALYSIS

4.1 PARAMETERS FOR NUMERICAL MODE

The slope gradient was 2H:1V on the sea side and 1.5H:1V on the land side, and the crest width ranged from 18 m near shore to 21 m offshore, according to the breakwaters' design standard. For the convenience of the numerical simulation analysis, these seven sections were taken vertically across the cross-section of the structure (AA~GG). The section of

the rubble-mound breakwater is shown in Fig.18 (B is the width of the breakwater crest, h is the depth of water and d is the thickness of the soft marine soils).

The marine soils were assumed to be anisotropic, elastic material during the simulation, and simplified as a single layer. Therefore, the relevant experimental parameters, such as the effective friction angle and the slope of normal consolidation line, were obtained from experimental results. According to the numerical mode requirement, the stratum condition and the soils' property parameters are shown in Table 4.

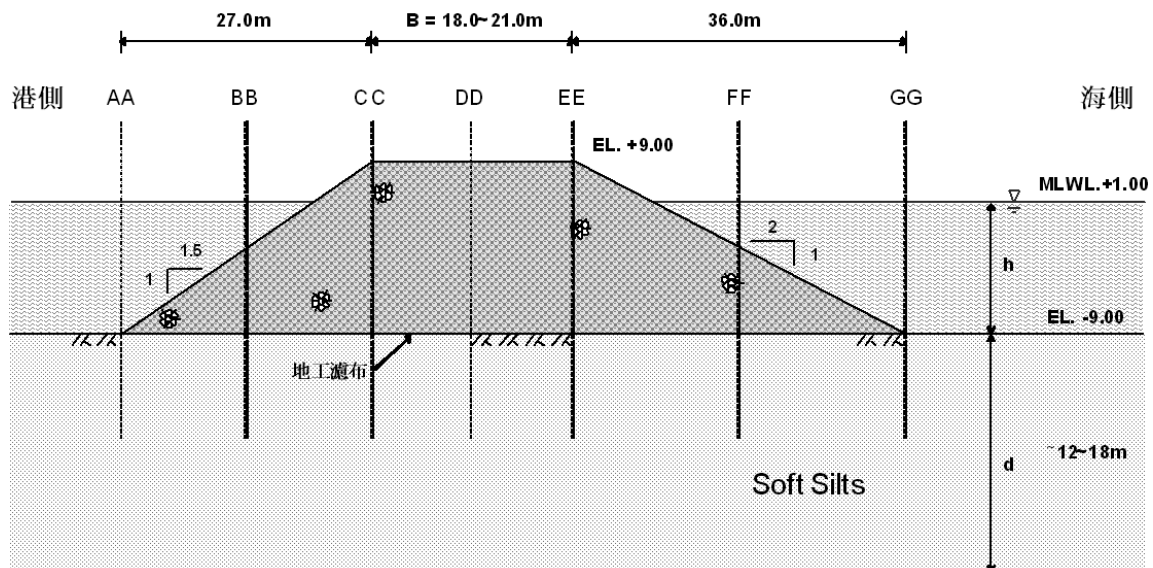


Figure 18. Sketch profile of the simplified rubble-mound breakwater.

Table 4. Parameters used in numerical simulation.

Linear Elastic	
A (pore pressure parameter)	0.78#
B (pore pressure parameter)	1.00#
E (elastic modulus)	5 MPa, 8 MPa* (Soft silt) 399 MPa (Rubble mound)
ν (Poisson's ratio)	0.4 (Soft silt) 0.3 (Rubble mound)
K_0 (coefficient of earth pressure at rest)	0.60, 0.60*
γ_t (bulk unit weight)	16.4, 16.7 kN/m ³ (Soft silt) 19.6 kN/m ³ (Rubble mound)
Modified Clay	
C_c (compression index)	0.313, 0.297*
C_s (swelling index)	0.0507, 0.0496*
λ (slope of normal consolidation line)	0.136, 0.129*
κ (slope of swelling line)	0.0220, 0.0215*
ϕ' (effective friction angle)	25.38°, 35.87°*
M (slope of critical state line)	1.00, 1.46*
Γ (specific volume)	2.648, 2.527*
OCR (over consolidation ratio)	1.00
Consolidation	
k (hydraulic conductivity)	2.07×10^{-4} m/day 1.42×10^{-4} m/day*
m_v (coefficient of volume compressibility)	3.70×10^{-3} 1/kPa 3.65×10^{-3} 1/kPa*

Note:

1. The condition of filling rubbles for breakwater meets the port structures' design standard issued by the Ministry of Communications and the parameters

2. "#": These parameter values reflect the initial properties that existed at the beginning of the construction.
3. "*": These parameter values reflect the properties that existed at the end of the construction when the unit weight of the marine soils increased to 16.7 kN/m³.

4.2 MODE PREDICTION AND RESULTS DISCUSSION. SIMULATION OF RESULTS AT DIFFERENT PHASES OF THE STRATIFIED GEO-STRUCTURE

Seven sections of the rubble-mound breakwater were analyzed to determine the maximum settlement induced during the construction steps. The settlement quantity of the soft marine silts increased with the increasing of the construction height (as shown in Fig 19). The seabed slightly up-heaved at the toe (at section GG) on the sea side. From the analysis, the largest settlement was detected near the sea-side toe (section BB), not at the core (section DD) of the breakwater, as shown in Fig. 20. The whole soft silts are stable before the construction height reached 6m, but when the height exceeded 9m, the vertical displacements were found over a large area of the soil layer and the phenomenon of upheaval was induced on the seabed. The settlement quantity increased with the increase of the thickness (h) of the soil layer and the width (B) of the breakwater. It can be concluded that the thicker soil layer may have a larger settlement.

The soft silt layers experienced lateral displacements due to the extrusion caused by the rubble-mound construction. The displacements were more obvious on the land side than on the sea side, as shown in Fig. 21.

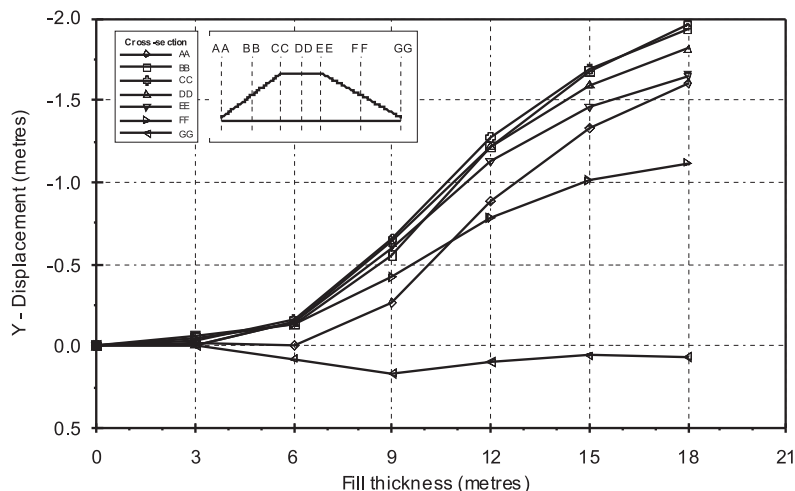


Figure 19. Settlement quantities of different sections of rubble-mound breakwaters under different construction steps.

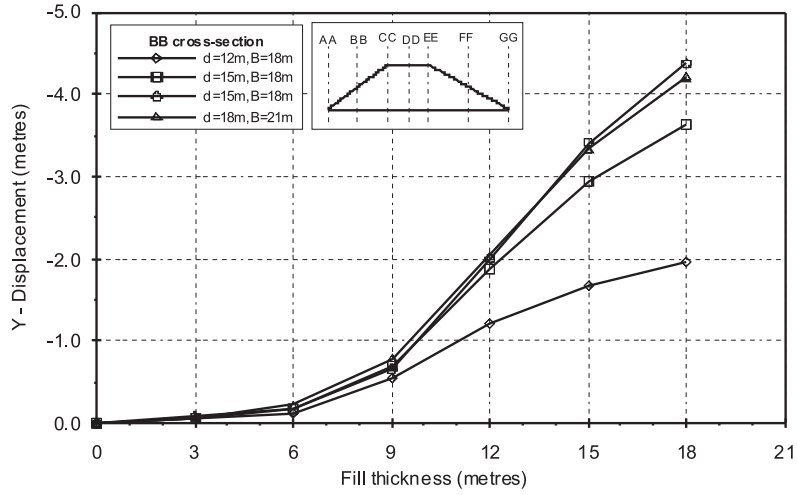


Figure 20. Thicknesses of different soil layers and the settlement quantity of rubble-mound breakwater under different construction steps.

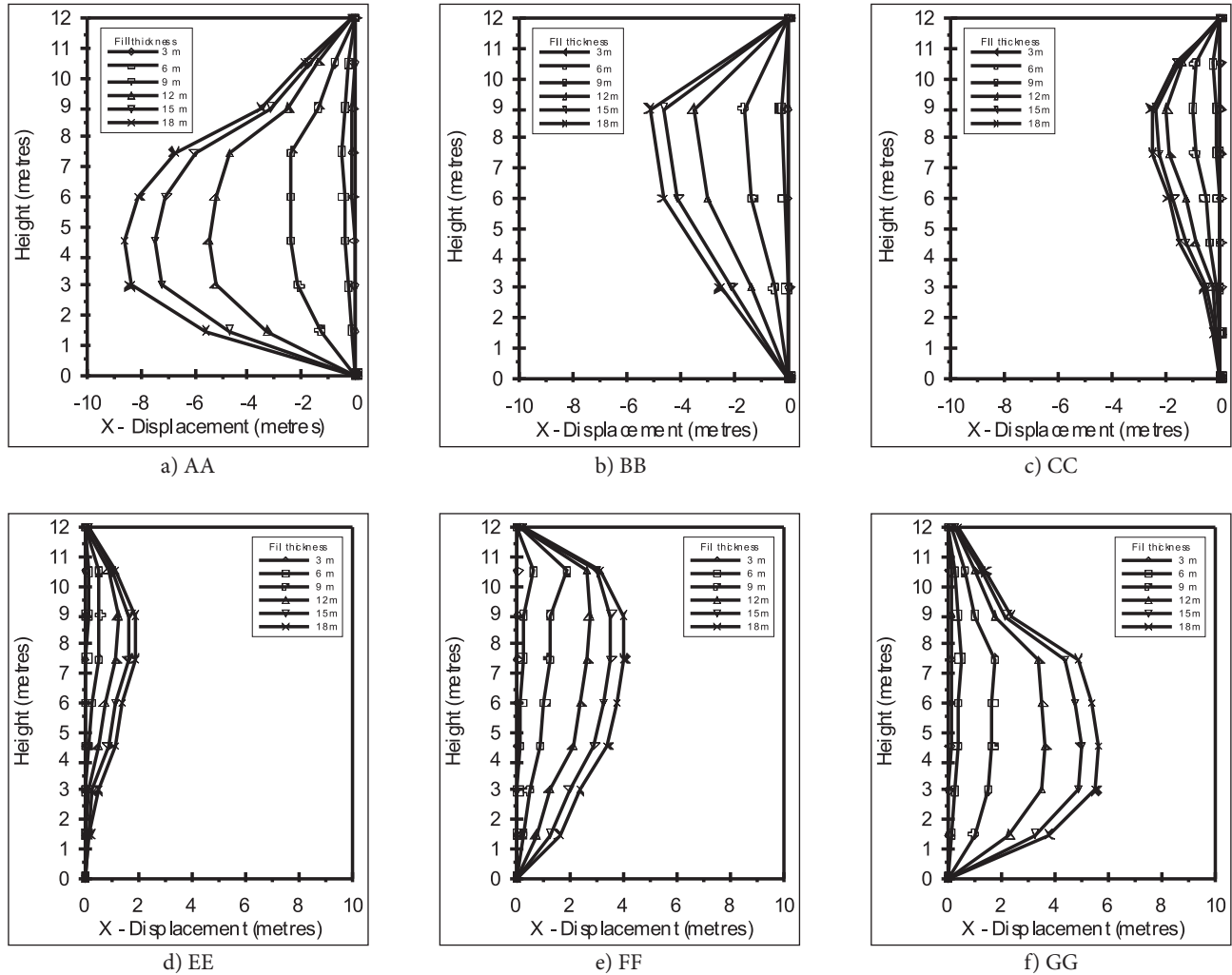


Figure 21. Side displacement of the different sections of breakwater under construction.

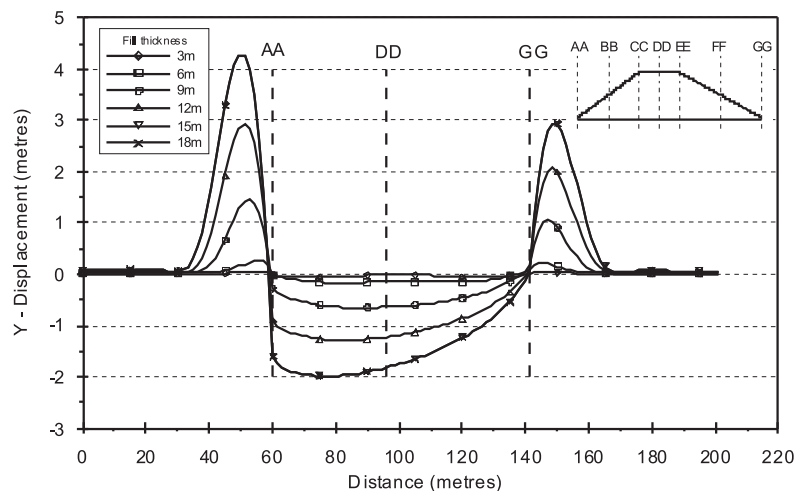


Figure 22. Settlement and upheaval of seabed under construction.

The behaviors of the seabed for filling the rubble mound under different loading were analyzed (as Fig. 22). The soft marine silts experienced larger lateral displacements under the increasing loading coming from the rubble mound, the front toe of the breakwater up-heaved due to extrusion. The area affected extended to about 40m (equivalent to four times the soil layer thickness) beyond the toe. It could be predicted that the slope of the soft marine silts suffered asymmetric loading. The bearing capacity of the soft silts cannot resist and the possible partial breakage mechanism and slip may occur.

4.3 RESULTS OF SEABED UPHEAVAL IN RUBBLE FILLING DISTANCE

When the length of the filling rubbles on in-situ reached 0k+250 m, an unreasonable settlement of the rubble-mound breakwater occurred. In order to evaluate the upheaval height caused by side displacement before the breakwater, the different seabed sites were analyzed at an interval of 120 m when filling the rubbles. The relevant stratum, mode configuration and landform before the breakwater are shown in Fig. 23 and Fig. 24.

The results of Fig.25 show that the extrusion of the seabed is most serious when the rubble filling reached 0k + 120 m. The upheaval was about 7.3 m at the other mileages of the filling rubbles and a side displacement occurred due to the construction of the breakwater. Furthermore, the slope of the stratum speeded up the slip of the slope of soil layer and the thickness of the nearshore seabed was small but a large-area upheaval occurred on it. This phenomenon coincided with the upheaval during the construction of the Baisha Port in 1995, particularly the side settlement at mileages of 0k+120 m during the construction on the site.

5 CONCLUSION

In order to further discuss the disaster factors caused by marine silts, the ongoing expansion of breakwaters at the Fuao Port of Ma-Zu was chosen as the research area. A series of experiments, including one-dimensional consolidation and a tri-axial mechanical test, were performed in this study. The in-situ data related to stratum drilling and steel-pipe piling as well as geological sampling on in-situ and laboratory analyses to evaluate the breakage and possible amount of settlement of the soil layer caused by loading. A suitable numerical model was also developed for a prediction of the settlement stability of the soft marine ground in this study.

According to the isotropic and K_0 consolidation without drainage, the initial value increased gradually, and the excessive pore-water pressure increased and approached the positive critical value as the strain increased. This phenomenon was consistent with a definition of specimen breakage by critical state theory: the critical state was reached when the soils deformed under stress loading.

The relationships between different tests were $CIU > SUU > Torvane$, which coincide with the study of the shear-strength evaluation of a silts specimen under different tests (Lin, 1988). These evaluations indicated that S_u values were an over estimation and may be the result of the specimen consolidated completely in the CIU test. However, it was apparent that the S_u were an under estimation and the effective stresses were zero, which reduced by the specimen saturated by back pressure in the SUU test.

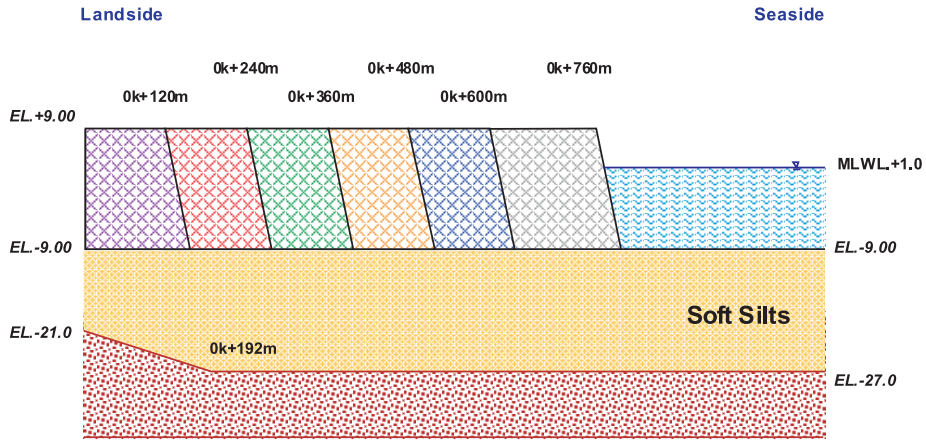


Figure 23. Landform and boundary conditions in the mode for analysis of the filling construction.

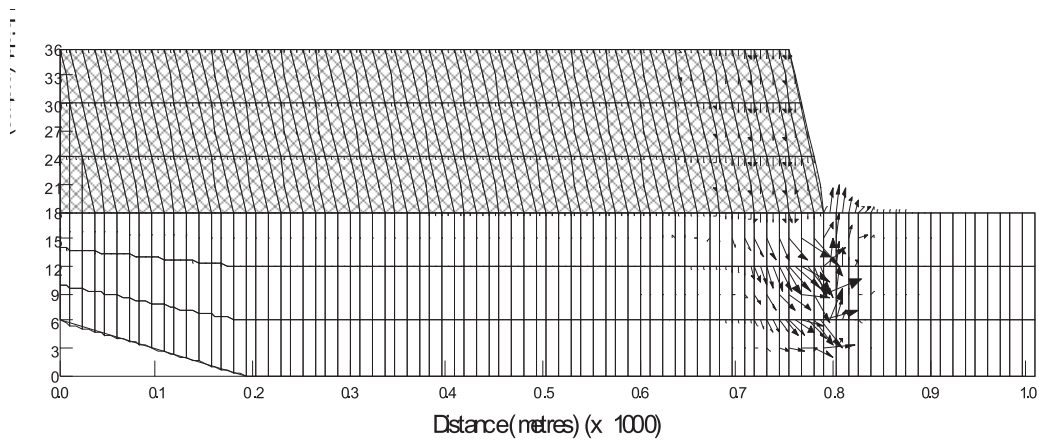


Figure 24. Landform change results of seabed before the simulation breakwater in the filling rubbles mileage.

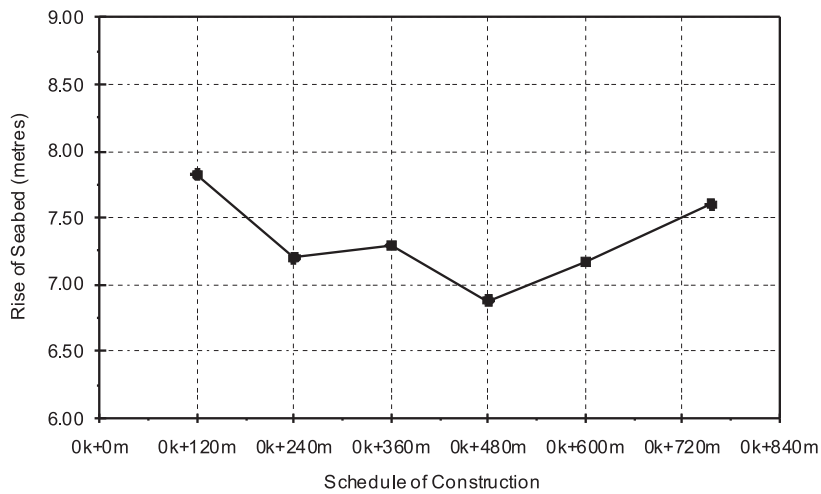


Figure 25. Rise of the front seabed in different construction mileages.

The soft marine silts at the breakwater induced displacement, greatly increasing with the filling rubble-mound loading, and then the front toe of the breakwater may experience upheaval due to extrusion. This could be predicted when the side slope of soft marine silts suffered asymmetric loading. The bearing capacity of the soft silts cannot resist and the partial breakage mechanism and slip may occur.

From the simulation results of seabed upheaval in rubble-filling mileage, the extrusion of the seabed is the most serious when the rubble filling reached 0k+120 m. The upheaval was about 7.3 m at the other construction of filling rubbles. The side displacement occurred on the near-shore due to the construction of the rubble-mound breakwater. Furthermore, the slope of stratum speeded up the slide of the slope on the soil layer. The thickness of the seabed at the near-shore was small but large-area upheaval occurred on the seabed. This phenomenon coincided with the disasters during the construction of Baisha Port in 1995, particularly the side settlement at mileages of 0k+120 m during construction on the site.

REFERENCES

- Atkinson, J. H., Evan J. S., Scott, C. R. (1985). Development in Microcomputer of Controlled Path Testing. *Ground Engineering*, 108, 1,15-22.
- Bishop, A. W., Henkel, D. J. (1957). *The Measurement of Soil Properties in the Triaxial Test*. Edward Aronld & Co., London.
- Bishop, A. W. (1958). Test Requirements for Measuring the Coefficient of Earth Pressure at Rest. *Proceedings, Conference on Earth Pressure Problems* (Brussels), Vol.1, pp.2.
- Bjerrum, L. (1963). Allowable Settlement of Structure. *Proceedings of European Conf. on Soil Mech. and Found. Eng.*, Weisbaden, Germany, Vol.2, pp. 35-137.
- Burcharth, H. F., Frgaard, P. (1987). On the Stability of Berm Breakwater Roundheads and Trunk Erosion in Oblique Waves. Seminar on Unconventional Rubble-Mound Breakwater, Ottawa.
- Chen, C. C. (2004). The Mechanical Properties of the Marine Soft Clay beneath the Near Shore Structure. Master Thesis, Dep. of Harbor and River Engineering, National Taiwan Ocean University.
- Chien, Lien-Kwei, Chi-Wei Chen, Chih-Hsin Chang and Tsung-Sheng Feng (2005). Engineering behavior and settlement evaluation of cement stabilized marine clay. *Proceedings of the 27th Ocean Engineering Conference in Taiwan*, pp. 973-980.
- Haykin, S. (1999). *Neural Networks*. Second ed. Prentice-Hall, Eaglewood Cliffs, NJ.
- Holtz, R. D., Kovacs, W. D. (1981). *An Introduction to Geotechnical Engineering*. Prentice-Hall, Inc., Englewood Cliffs, New Jersey.
- Jeng, D. S., Cha, D. H., Lin, Y. S., Hu, P. S. (2001). Wave-Induced Pore Pressure around a Composite Breakwater. *Ocean Engineering*, 28, 1413-1435.
- Kim, D.H., Park, W.S. (2005). Neural network for design and reliability analysis of rubble-mound breakwaters. *Ocean Engineering*, 32 (11-12), 1332-1349.
- Locat, J. (1996). On the Development of Microstructure in Collapsible soils. Lessons from the Study of Recent Sediments and Artificial Cementation and In Genesis and Properties of Collapsible Soils by E. Derbyshire, T. Dijstra, and I. J. Smalley, Kluwer Academic Publisher, Dordrecht, The Netherlands, pp.93-128.
- Leonards, G. A. (1962). *Engineering Properties of Soils*. McGraw-Hill, New York, U.S.A.
- Lien-kwei Chien, Tsung-shen Feng, Huo-Ping Weng and Wen-Chian Tzeng (2007). The Shear Strength and Mound Settlement of Nearshore Soft Marine Silts. *Proceedings of the 17th International Offshore and Polar Engineering Conference*, Vol. II, pp.1334-1339.
- Lippmann, R.P. (1987). An introduction to computing with neural nets. *IEEE ASSP Magazine*.
- Mayne, P. W. (1985). Stress Anisotropic Effects on Clay Strength. *Journal of Geotechnical Engineering*, 111, 3, 356-366
- Medina, J.R., Garrido, J., Gomez-Martin, M.E., Vidal, C. (2003). Armour damage analysis using neural networks. *Proceedings of Coastal Structures, Portland, OR, USA*.
- Skempton, A. W., Sowa, V. A (1963) The Behavior of Saturated Clays During Sampling and Testing. *Geotechnique*, 13, 4, 269-290.
- Skempton, A. W. (1954). The Pore-Pressure Coefficients A and B^o. *Geotechnique*, 4, 143-147.
- Sowers, G. F. (1962). *Shallow Foundations in Foundation Engineering*. G. A. Leonards (ed.), McGraw-Hill, New York.
- Sridharan, A., Murthy, N. S., Prakash, K. (1987). Rectangular Hyperbola Method of Consolidation Analysis. *Geotechnique*, 37, 3, 355-368.
- Terzaghi, K. (1925). Principles of Soil Mechanics, Determination of Permeability of Clay. *Engineering News Record*, 95, 21, 932.
- Vesic, A. S. (1973). Analysis of Ultimate Loads of Soil Mechanics and Foundations. *Journal of the Soil Mechanics and Foundations Engineering*, 99, SM1, 45-73.

- Whitman, R.V., Bailey, W. A. (1967). Use of Computers for Slope Stability Analysis. *Journal of the Soil Mechanics and Foundation Engineering Division*, 93, 4, 475-498.
- Yagci, O., Mercan, D.E., Cigizoglu, H.K., Kabdasli, M.S. (2005). Artificial intelligence methods in breakwater damage ratio estimation. *Ocean Engineering* 32 (17/18), 2088-2106.
- Yong, R. N., Sheeran, D. E. (1973). Fabric Unit Interaction and Soil Behaviour. *Proceedings of the International Symposium on Soil Structure*, Gothenburg, Sweden, 176-183.
- Yong, R. N., Warkentin, B. P. (1975). *Soil Properties and Behaviour*. Elsevier Scientific Publishing Co., New York.

NAVODILA AVTORJEM

Članki so objavljeni v angleškem jeziku s prevodom izvlečka v slovenski jezik.

VSEBINA ČLANKA

Članek naj bo napisan v naslednji obliki:

- Naslov, ki primerno opisuje vsebino članka in ne presega 80 znakov.
- Izvleček, ki naj bo skrajšana oblika članka in naj ne presega 250 besed. Izvleček mora vsebovati osnove, jedro in cilje raziskave, uporabljeno metodologijo dela, povzetek izidov in osnovne sklepe.
- Uvod, v katerem naj bo pregled novejšega stanja in zadostne informacije za razumevanje ter pregled izidov dela, predstavljenih v članku.
- Teorija.
- Eksperimentalni del, ki naj vsebuje podatke o postavitvi preiskusa in metode, uporabljene pri pridobitvi izidov.
- Izidi, ki naj bodo jasno prikazani, po potrebi v obliki slik in preglednic.
- Razprava, v kateri naj bodo prikazane povezave in posplošitve, uporabljene za pridobitev izidov. Prikazana naj bo tudi pomembnost izidov in primerjava s poprej objavljenimi deli.
- Sklepi, v katerih naj bo prikazan en ali več sklepov, ki izhajajo iz izidov in razprave.
- Literatura, ki mora biti v besedilu oštevilčena zaporedno in označena z oglatimi oklepaji [1] ter na koncu članka zbrana v seznamu literature.

OBLIKA ČLANKA

Besedilo naj bo pisano na listih formata A4, z dvojnimi presledki med vrstami in s 3.0 cm širokim robom, da je dovolj prostora za popravke lektorjev. Najbolje je, da pripravite besedilo v urejevalniku Microsoft Word. Hkrati dostavite odtis članka na papirju, vključno z vsemi slikami in preglednicami ter identično kopijo v elektronski obliki.

Enačbe naj bodo v besedilu postavljene v ločene vrstice in na desnem robu označene s tekočo številko v okroglih oklepajih.

ENOTE IN OKRAJŠAVE

V besedilu, preglednicah in slikah uporabljajte le standardne označbe in okrajšave SI. Simbole fizikalnih

veličin v besedilu pišite poševno (npr. v , T itn.). Simbole enot, ki sestojijo iz črk, pa pokončno (npr. Pa, m itn.).

Vse okrajšave naj bodo, ko se prvič pojavijo, izpisane v celoti.

SLIKE

Slike morajo biti zaporedno oštevilčene in označene, v besedilu in podnaslovu, kot sl. 1, sl. 2 itn. Posnete naj bodo v kateremkoli od razširjenih formatov, npr. BMP, JPG, GIF. Za pripravo diagramov in risb priporočamo CDR format (CorelDraw), saj so slike v njem vektorske in jih lahko pri končni obdelavi preprosto povečujemo ali pomajšujemo.

Pri označevanju osi v diagramih, kadar je le mogoče, uporabite označbe veličin (npr. v , T). V diagramih z več krivuljami mora biti vsaka krivulja označena. Pomen oznake mora biti razložen v podnapisu slike.

Za vse slike po fotografskih posnetkih je treba priložiti izvirne fotografije ali kakovostno narejen posnetek.

PREGLEDNICE

Preglednice morajo biti zaporedno oštevilčene in označene, v besedilu in podnaslovu, kot preglednica 1, preglednica 2 itn. V preglednicah ne uporabljajte izpisanih imen veličin, ampak samo ustrezne simbole. K fizikalnim količinam, npr. t (pisano poševno), pripišite enote (pisano pokončno) v novo vrsto brez oklepajev.

Vse opombe naj bodo označene z uporabo dvignjene številke¹.

SEZNAM LITERATURE

Vsa literatura mora biti navedena v seznamu na koncu članka v prikazani obliki po vrsti za revije, zbornike in knjige:

- [1] Feng, T. W. (2000). Fall-cone penetration and water content relationship of clays. *Geotechnique* 50, No. 2, 181-187.
- [2] Ortolan, Ž. and Mihalinec, Z. (1998). Plasticity index-Indicator of shear strength and a major axis of geotechnical modelling. *Proceedings of the*

- Eleventh Danube-European conference on soil mechanics and geotechnical engineering, Poreč, 25–29 May 1998.
- [3] Toporišič, J. (1994). Slovenski pravopis. 2nd.ed., DZS, Ljubljana.

PODATKI O AVTORJIH

Članku priložite tudi podatke o avtorjih: imena, nazive, popolne poštno naslove, številke telefona in faksa, naslove elektronske pošte. Navedite kontaktno osebo.

SPREJEM ČLANKOV IN AVTORSKE PRAVICE

Uredništvo si pridržuje pravico do odločanja o sprejemu članka za objavo, strokovno oceno mednarodnih recenzentov in morebitnem predlogu za krajšanje ali izpopolnitev ter terminološke in jezikovne korekture.

Avtor mora predložiti pisno izjavo, da je besedilo njegovo izvirno delo in ni bilo v dani obliki še nikjer objavljeno. Z objavo preidejo avtorske pravice na revijo ACTA GEOTECHNICA SLOVENICA. Pri morebitnih kasnejših objavah mora biti AGS navedena kot vir.

Rokopisi člankov ostanejo v arhivu AGS.

Vsa nadaljnja pojasnila daje:

Uredništvo
ACTA GEOTECHNICA SLOVENICA
Univerza v Mariboru
Fakulteta za gradbeništvo
Smetanova ulica 17
2000 Maribor
Slovenija
E-pošta: ags@uni-mb.si

INSTRUCTIONS FOR AUTHORS

The papers are published in English with a translation of the abstract into Slovene.

FORMAT OF THE PAPER

The paper should have the following structure:

- A Title that adequately describes the content of the paper and should not exceed 80 characters;
- An Abstract, which should be viewed as a mini version of the paper and should not exceed 250 words. The Abstract should state the principal objectives and the scope of the investigation and the methodology employed, it should also summarise the results and state the principal conclusions;
- An Introduction, which should provide a review of recent literature and sufficient background information to allow the results of the paper to be understood and evaluated;
- A Theoretical section;
- An Experimental section, which should provide details of the experimental set-up and the methods used for obtaining the results;
- A Results section, which should clearly and concisely present the data using figures and tables where appropriate;
- A Discussion section, which should describe the relationships shown and the generalisations made

possible by the results and discuss the significance of the results, making comparisons with previously published work;

- Conclusions, which should present one or more conclusions that have been drawn from the results and subsequent discussion;
- References, which must be numbered consecutively in the text using square brackets [1] and collected together in a reference list at the end of the paper.

LAYOUT OF THE TEXT

The text should be written in A4 format, with double spacing and margins of 3 cm, to provide editors with space to write in their corrections. Microsoft Word for Windows is the preferred format for submission. One hard copy, including all figures, tables and illustrations and an identical electronic version of the manuscript must be submitted simultaneously.

Equations should be on a separate line in the main body of the text and marked on the right-hand side of the page with numbers in round brackets.

UNITS AND ABBREVIATIONS

Only standard SI symbols and abbreviations should be used in the text, tables and figures. Symbols for physical

quantities in the text should be written in *Italics* (e.g. *v*, *T*, etc.). Symbols for units that consist of letters should be in plain text (e.g. Pa, m, etc.).

All abbreviations should be spelt out in full on first appearance.

FIGURES

Figures must be cited in consecutive numerical order in the text and referred to in both the text and the caption as Fig. 1, Fig. 2, etc. Figures may be saved in any common format, e.g. BMP, JPG, GIF. However, the use of CDR format (CorelDraw) is recommended for graphs and line drawings, since vector images can be easily reduced or enlarged during final processing of the paper.

When labelling axes, physical quantities (e.g. *v*, *T*) should be used whenever possible. Multi-curve graphs should have individual curves marked with a symbol; the meaning of the symbol should be explained in the figure caption.

Good quality black-and-white photographs or scanned images should be supplied for illustrations.

TABLES

Tables must be cited in consecutive numerical order in the text and referred to in both the text and the caption as Table 1, Table 2, etc. The use of names for quantities in tables should be avoided if possible: corresponding symbols are preferred. In addition to the physical quantity, e.g. *t* (in *Italics*), units (normal text), should be added on a new line without brackets.

Any footnotes should be indicated by the use of the superscript¹.

LIST OF REFERENCES

References should be collected at the end of the paper in the following styles for journals, proceedings and books, respectively:

- [1] Feng, T. W. (2000). Fall-cone penetration and water content relationship of clays. *Geotechnique* 50, No. 2, 181-187.
- [2] Ortolan, Ž. and Mihalinec, Z. (1998). Plasticity index-Indicator of shear strength and a major axis of geotechnical modelling. Proceedings of the Eleventh Danube-European conference on soil mechanics and geotechnical engineering, Poreč, 25–29 May 1998.

- [3] Toporišič, J. (1994). *Slovenski pravopis*. 2nd.ed., DZS, Ljubljana.

AUTHOR INFORMATION

The following information about the authors should be enclosed with the paper: names, complete postal addresses, telephone and fax numbers and E-mail addresses. Indicate the corresponding person.

ACCEPTANCE OF PAPERS AND COPYRIGHT

The Editorial Committee of the Slovenian Geotechnical Review reserves the right to decide whether a paper is acceptable for publication, to obtain peer reviews for submitted papers, and if necessary, to require changes in the content, length or language.

Authors must also enclose a written statement that the paper is original unpublished work, and not under consideration for publication elsewhere. On publication, copyright for the paper shall pass to the ACTA GEOTECHNICA SLOVENICA. The AGS must be stated as a source in all later publication.

Papers will be kept in the archives of the AGS.

For further information contact:

Editorial Board
 ACTA GEOTECHNICA SLOVENICA
 University of Maribor
 Faculty of Civil Engineering
 Smetanova ulica 17
 2000 Maribor
 Slovenia
 E-mail: ags@uni-mb.si

NAMEN REVIJE

Namen revije ACTA GEOTECHNICA SLOVENICA je objavljane kakovostnih teoretičnih člankov z novih pomembnih področij geomehanike in geotehnike, ki bodo dolgoročno vplivali na temeljne in praktične vidike teh področij.

ACTA GEOTECHNICA SLOVENICA objavlja članke s področij: mehanika zemljin in kamnin, inženirska geologija, okoljska geotehnika, geosintetika, geotehnične konstrukcije, numerične in analitične metode, računalniško modeliranje, optimizacija geotehničnih konstrukcij, terenske in laboratorijske preiskave.

Revija redno izhaja dvakrat letno.

AVTORSKE PRAVICE

Ko uredništvo prejme članek v objavo, prosi avtorja(je), da prenese(jo) avtorske pravice za članek na izdajatelja, da bi zagotovili kar se da obsežno razširjanje informacij. Naša revija in posamezni prispevki so zaščiteni z avtorskimi pravicami izdajatelja in zanje veljajo naslednji pogoji:

fotokopiranje

V skladu z našimi zakoni o zaščiti avtorskih pravic je dovoljeno narediti eno kopijo posameznega članka za osebno uporabo. Za naslednje fotokopije, vključno z večkratnim fotokopiranjem, sistematičnim fotokopiranjem, kopiranjem za reklamne ali predstavitvene namene, nadaljnjo prodajo in vsemi oblikami nedobičkonosne uporabe je treba pridobiti dovoljenje izdajatelja in plačati določen znesek.

Naročniki revije smejo kopirati kazalo z vsebino revije ali pripraviti seznam člankov z izvlečki za rabo v svojih ustanovah.

elektronsko shranjevanje

Za elektronsko shranjevanje vsakršnega gradiva iz revije, vključno z vsemi članki ali deli članka, je potrebno dovoljenje izdajatelja.

ODGOVORNOST

Revija ne prevzame nobene odgovornosti za poškodbe in/ali škodo na osebah in na lastnini na podlagi odgovornosti za izdelke, zaradi malomarnosti ali drugače, ali zaradi uporabe kakršnekoli metode, izdelka, navodil ali zamisli, ki so opisani v njej.

AIMS AND SCOPE

ACTA GEOTECHNICA SLOVENICA aims to play an important role in publishing high-quality, theoretical papers from important and emerging areas that will have a lasting impact on fundamental and practical aspects of geomechanics and geotechnical engineering.

ACTA GEOTECHNICA SLOVENICA publishes papers from the following areas: soil and rock mechanics, engineering geology, environmental geotechnics, geosynthetic, geotechnical structures, numerical and analytical methods, computer modelling, optimization of geotechnical structures, field and laboratory testing.

The journal is published twice a year.

COPYRIGHT

Upon acceptance of an article by the Editorial Board, the author(s) will be asked to transfer copyright for the article to the publisher. This transfer will ensure the widest possible dissemination of information. This review and the individual contributions contained in it are protected by publisher's copyright, and the following terms and conditions apply to their use:

photocopying

Single photocopies of single articles may be made for personal use, as allowed by national copyright laws. Permission of the publisher and payment of a fee are required for all other photocopying, including multiple or systematic copying, copying for advertising or promotional purposes, resale, and all forms of document delivery.

Subscribers may reproduce tables of contents or prepare lists of papers, including abstracts for internal circulation, within their institutions.

electronic storage

Permission of the publisher is required to store electronically any material contained in this review, including any paper or part of the paper.

RESPONSIBILITY

No responsibility is assumed by the publisher for any injury and/or damage to persons or property as a matter of product liability, negligence or otherwise, or from any use or operation of any methods, products, instructions or ideas contained in the material herein.